

Editorial corner – a personal view

Carbohydrate-based epoxies – good news for the environment?

Gy. Marosi*

Organic Chemistry and Technology Department of Budapest University of Technology and Economics, H-1111 Budapest, Műegyetem rkp. 3, Hungary

The relationship between polymers and the environment is contradictory. The use of polymers prevents deforestation but contributes to the accumulation of solid wastes. Focused research on thermoplastic biopolymers promises a solution, however their programmed stabilization and recycling requires more efforts. General way for the management of thermosetting polymer wastes (such as recycling) is not available thus various approaches are considered. Their replacement with thermoplastics, depolymerization or use as filler are technically and/or economically limited thus their waste is mostly disposed by combustion. Nature shows the biodegradation of lignocellulosic ‘natural thermosets’ as an alternative solution. The research of biodegradable epoxy resins based on epoxidized soybean oil has a long history, however, the achievable thermal resistance is not comparable with the commercial ones. Although the carbohydrates are the building blocks of the most abundant natural polymers sugar-based alternatives of thermosetting polymers are not widely used. Major reason can be their water uptake being much higher than that of monomers derived from petrochemical feedstock. However, hydrophilicity can be suppressed by blocking the free OH functions. One of the most promising sugar-derivatives as starting material for polymerization is the group of dianhydrohexitols, such as diglycidyl ether of isosorbide (1,4:3,6-dianhydro-D-sorbitol), which can maintain the mechanical properties at elevated temperature, when incor-

porated into thermosets. However, its drawbacks are the relatively high cost and the limited number of epoxy groups. The higher functionality level of sorbitol glycidyl ether provides larger chemical variability but limited thermomechanical performance. Syntheses of further carbohydrate derivatives are needed to provide affordable and thermal resistant crosslinked polymers of controlled biodegradability. These monomers can originate from various industrial plants or even from agricultural byproducts. More expensive carbohydrate monomers such as modified chitosans can be considered as comonomers to be grafted onto the backbones and adjusting this way the final properties to the requirements. Fully biodegradable composites can be formed by combination of these resins with natural fiber reinforcements.



Prof. Dr. György Marosi
Member of International Advisory Board

*Corresponding author, e-mail: gmarosi@mail.bme.hu
© BME-PT

Novel thermoplastic vulcanizates (TPVs) based on silicone rubber and polyamide exploring peroxide cross-linking

T. Chatterjee^{1,2}, S. Wiessner^{1,3}, K. Naskar^{2*}, G. Heinrich^{1,3}

¹Leibniz-Institut für Polymerforschung Dresden e.V., Hohe Strasse 6, D-01069 Dresden, Germany

²Rubber Technology Centre, Indian Institute of Technology, Kharagpur, 721302 Kharagpur, West Bengal, India

³Technische Universität Dresden, Institut für Werkstoffwissenschaft, D-01062 Dresden, Germany

Received 10 September 2013; accepted in revised form 19 November 2013

Abstract. Novel thermoplastic vulcanizates (TPVs) based on silicone rubber (PDMS) and polyamide (PA12) have been prepared by dynamic vulcanization process. The effect of dynamic vulcanization and influence of various types of peroxides as cross-linking agents were studied in detail. All the TPVs were prepared at a ratio of 50/50 wt% of silicone rubber and polyamide. Three structurally different peroxides, namely dicumyl peroxide (DCP), 3,3,5,7,7-pentamethyl 1,2,4-trioxepane (PMTO) and cumyl hydroperoxide (CHP) were taken for investigation. Though DCP was the best option for curing the silicone rubber, at high temperature it suffers from scorch safety. An inhibitor 2,2,6,6-tetramethylpiperidinyloxy (TEMPO) was added with DCP to stabilize the radicals in order to increase the scorch time. Though CHP (hydroperoxide) had higher half life time than DCP at higher temperature, it has no significant effect on cross-linking of silicone rubber. PMTO showed prolonged scorch safety and better cross-linking efficiency rather than the other two. TPVs of DCP and PMTO were made up to 11 minutes of mixing. Increased values of tensile strength and elongation at break of PMTO cross-linked TPV indicate the superiority of PMTO. Scanning electron micrographs correlate with mechanical properties of the TPVs. High storage modulus (E') and lower loss tangent value of the PMTO cross-linked TPV indicate the higher degree of cross-linking which is also well supported by the overall cross-link density value. Thus PMTO was found to be the superior peroxide for cross-linking of silicone rubber at high temperature.

Keywords: polymer blends and alloys, thermoplastic vulcanizate, silicone rubber (PDMS), polyamide (PA12) and peroxides

1. Introduction

Blending of polymers is a smart and economical strategy for obtaining new and improved polymeric materials from the existing polymers, which are difficult to obtain by direct polymerization process [1, 2]. Even though more than 400 miscible polymer pairs have been reported [3, 4], most of them are not miscible on a molecular scale and tend to undergo phase separation during mixing. Numerous rubber-plastic blends are available, only few of them are commercially attractive because of compatibility between the components. Thermoplastic elastomers (TPEs) are a class of polymers or polymer blends that have

rubber-like behaviour, but can be melt-processed like thermoplastic polymers [5, 6]. The combination of these properties is obtained by the two-phase structure of the materials: the soft phase, an elastomer, gives the rubber-like properties in the solid state, whereas the hard phase, a thermoplastic polymer with high glass transition temperature, gives strength to the blend. At the temperature of utilization, the latter is the stiffer phase that acts as physical cross-linker for the elastomer phase. At elevated temperatures (above the glass transition temperature or above the melting point), the hard phase softens and the TPE becomes processable.

*Corresponding author, e-mail: knaskar@rtc.iitkgp.ernet.in

© BME-PT

Thermoplastic vulcanizates (TPVs) are a highly engineered class of thermoplastic elastomers, comprising a cross-linked elastomeric phase and a melt processable thermoplastic phase. These materials are produced by dynamic vulcanization process, in which both mixing and cross-linking are carried out at the same time in a melt mixing device. Resulting compound exhibits more elastomer-like properties: such as lower compression set, lower stiffness, greater resistance to fatigue, heat and chemicals than the corresponding rubber or plastic [7, 8]. The dynamic vulcanization process was first reported by Gessler and Haslett [9] in 1962 and then further developed by Fischer [10] by his early work on polypropylene (PP)/ethylene propylene diene rubber (EPDM) TPVs with peroxides as cross-linking agent, resulted in the commercialization of ‘Uniroyal TPR’ thermoplastic rubber. Greater industrial attention was generated only after extensive study of TPVs based on various blend components by Coran and Patel in the 1980s [11, 12]. They performed extensive studies on PP and EPDM blends that were dynamically vulcanized with high crosslink density in the rubber phase. These works led to the commercialization of ‘Santoprene’ TPE, which was introduced by Monsanto in 1981. Most commercial TPVs are based on heterogeneous blends of PP and ethylene-propylene-diene rubber (EPDM) because of their structural compatibility. Naskar and Noordermeer [13, 14] extensively studied the influence of different peroxides and multifunctional peroxide in the conventional PP/EPDM blends. Later Naskar *et al.* [15] also developed a novel PP/EPDM TPV by electron induced reactive processing. Further TPVs based on silicone rubber [16] and maleated ethylene propylene rubber (EPM) [17] was also developed for some special purpose. Babu and coworkers [18, 19] explored a new TPV based on polypropylene (PP) and ethylene octene copolymer (EOC) blend system. EOC has gained special attention because of its unique molecular structure and also it provides better toughening characteristics than EPDM rubber [20, 21]. Recently Giri *et al.* [22] developed a new system in this family which is based on LLDPE/PDMS blend system. But all the TPVs have limited use in automotive applications due to their low heat resistance and poor oil resistance properties associated with the olefinic thermoplastic matrices [23]. To fulfill these two requirements a new family of high performance TPV called ‘super TPV’, based on

cross-linked silicone rubber particles dispersed in a variety of engineering thermoplastic matrix, was developed by Dow Corning [24]. In this present investigation polyamide (PA12) and silicone rubber (PDMS) are of special interest and a new super TPV system with a blend ratio of 50/50 wt% has been developed.

Silicone rubber (PDMS) is notable for its unique characteristics: such as very low T_g (-125°C) due to highly flexible [O–Si–O] backbone, very wide service temperature range, good aging properties, resistance to UV radiation, low toxicity, hydrophobic and physiologically inert [25–27]. Tensile strength of silicone rubber is very low and its oil and solvent resistance properties are also very poor [28]. To overcome these drawbacks of silicone rubber, a new blend system of silicone rubber (PDMS) and polyamide (PA12) has been chosen for the development of a novel TPV with controlled properties. PA12 has excellent solvent and oil resistance, in particular acid and alkali resistance and excellent environmental stress cracking resistance at elevated temperature [29]. Cross-linking of the PDMS rubber phase by organic peroxides suffers from scorching problems at high mixing temperature due to the faster decomposition of the peroxides (normally used for curing) [30, 31]. To overcome this difficulty three structurally different peroxides, namely dicumyl peroxide (DCP), 3,3,5,7,7-pentamethyl 1,2,4-trioxepane (PMTO) and cumyl hydroperoxide (CHP) were chosen for investigation. It is reported earlier that, though DCP was the best option for curing the silicone rubber, at high temperature it suffers from scorch safety since it has a typical cross-linking temperature at 160°C . At higher temperatures above 180°C it has very low half life time ($t_{1/2}$). An inhibitor 2,2,6,6-tetramethylpiperidinyloxy (TEMPO) was added with DCP to increase the scorch safety by scavenging the peroxide radicals [31, 32]. The main objective of this present work is to develop of a novel high performance TPV based on a PDMS/PA12 blend system at 50:50 blends ratio using different peroxides with suitable decomposition kinetics as the cross-linking agent to induce dynamic vulcanization of the PDMS phase. After that the morphological characteristics, mechanical properties, dynamic mechanical analysis, rheological and thermal properties of all the TPV systems were pursued to get a better insight.

2. Experimental

2.1. Materials

Polydimethyl siloxane (PDMS) (which trade name is XIAMETER RBB-2140-50) was procured from Dow Corning, USA. It has a Mooney viscosity, $ML_{(1+4)}$ at 100°C of 30 and density at 25°C of 1.15 gm/cm³. Polyamide 12 (PA12) (Rilsan[®] AESNO TL) was procured from Arkema, France. It has the density at 25°C of 1.02 gm/cm³. The melt flow rate of PA12, measured at 190°C and 2.16 kg load is 0.646 gm/10 min. Main characteristics of these polymeric materials are reported in the Table 1.

Cross-linker: Three structurally different organic peroxides were used for the cross-linking of the PDMS as follows: i) Perkadox BC-FF, Dicumyl peroxide (DCP); ii) Trigonox 311-50D (PMTO);

iii) Trigonox K-90, Cumyl hydroperoxide (CHP). All of them were procured from Akzo Nobel, Netherlands. Their commercial names, chemical names, chemical structures and molecular characteristics are given in Table 2.

Nitroxide 2,2,6,6-tetramethylpiperidinyloxy (TEMPO) procured from Aldrich Chemicals, was used as an inhibitor, in conjunction with DCP to control the scorch during mixing. The concentration of TEMPO was calculated in order to provide a molar ratio of ([TEMPO]/[DCP] = 1.6) [31, 32].

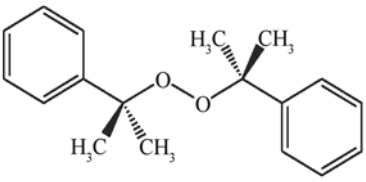
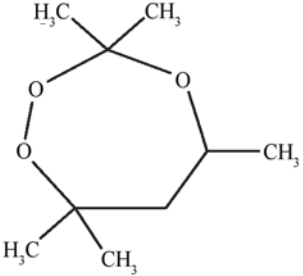
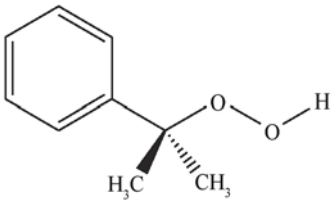
2.2. Mixing

To understand the curing characteristics of the three peroxides, the mixing of different peroxides with PDMS was performed in a laboratory kneader type

Table 1. Characteristics of the raw materials

Material	Trade name	T _g [°C]	T _m [°C]	Tensile strength [MPa]	Tensile elongation at break [%]
Silicone rubber	XIAMETER RBB-2140-50	-124	-	0.8	465
Polyamide (PA12)	Rilsan [®] AESNO TL	55	177	68.9	330

Table 2. Commercial name, chemical name and molecular characteristics of the three different peroxides

Commercial name	Chemical name and structure	Active oxygen content [%]	Half life time (t _{1/2}) at 180°C [min]	Decomposition products
Perkadox BC-FF	dicumyl peroxide (DCP) 	5.92	0.50	acetophenone, methane, 2-phenylisopropanol
Trigonox 311-50D	3,3,5,7,7-pentamethyl-1,2,4-trioxepane (PMTO) 	9.18	21.13	methane, acetone, isopropyl acetate, 3-hydroxy-1,3-dimethylbutyl acetate, 3-methoxy-1,3-dimethylbutyl acetate
Trigonox K-90	cumyl hydroperoxide (CHP) 	10.51	19.15	acetophenone, methane, 2-phenylisopropanol

W30 EHT Brabender, Germany, having a free volume of 30 cm³ fitted with two counter-rotating rotors. Peroxides were mixed with PDMS at 40°C and at a rotor speed of 60 rpm. All the blends of silicone rubber (PDMS) and polyamide (PA12) at a blend ratio of 50:50 (wt%) were also prepared in a batch process using the same instrument at a rotor speed of 120 rpm. According to literature though polyamide has the melting point in the range of 180°C, but it has been seen that polyamide did not melt at 180°C even after 12 minutes mixing. For that reason mixing was performed at 190°C. The mixer was connected to a drive unit Plastograph, which allows using of integrated pendulum dynamometer to detect the torque during compounding. The temperature development in the mixed material is measured by an integrated gusset at the bottom region of the mixing chamber thermocouple. Temperature control of the mixing chamber, front and rear plate was done via integrated thermocouples. Using a mass temperature sensor and a self-aligning dynamometer, which detects the torque, a torque-temperature diagram in function of time is created.

For the reactive blending at first, peroxides (1 wt%) were premixed with PDMS at the room temperature before its addition to the molten PA12. For dicumyl peroxide (DCP), TEMPO was added with DCP to increase the scorch safety. At first PA12 was poured into the mixing chamber at 190°C and at 120 rpm and was allowed for melting. After melting of the PA12 matrix, PDMS (premixed with peroxide) was added to the molten thermoplastic phase. Finally TPVs were developed with (50/50) wt% of PDMS and PA12 at a rotor speed of 120 rpm at 190°C using 11 minutes of mixing. Then the samples were injection moulded from a micro-injection moulding machine at 250°C and 7 bar pressure. Testing was performed after 24 hour of maturation.

2.3. Testing procedure

2.3.1. Curing characteristics

Curing characteristics of the different peroxide mixed PDMS were determined from Göttfert Elastograph Vario 67.03, Germany. From this the optimum curing time as well as scorch time of PDMS for various peroxides was determined. Testing conditions were maintained at 180°C for 60 minutes and at a frequency of 1.67 Hz. The rotational angle of the disk was 5°.

2.3.2. Morphology study

The morphological study of final TPV samples and dispersion of PDMS and PA12 phase was carried out using a Scanning Electron Microscope (LEO 435 VP, Carl Zeiss SMT, Jena, Germany). At first, the sample was taken over a sticky surface made by conductive carbon cement on a SEM sample holder. After that the samples were cut with the ultramicrotome UC 7, Leica, Wetzlar, Germany and then it is platinum coated (layer thickness 15 nm) using a sputter coater (BAL-TEC SCD 500 Sputter Coater). The morphology has been characterized by energy dispersive X-ray spectroscopy (EDX) via mapping of carbon, silicon, nitrogen, oxygen distribution in the sample. EDX delivers information about morphology without etching. Morphology study of the TPVs was also carried out by atomic force microscope (Bruker, Icon, Germany). Testing has been performed in the tapping mode. Tip stiffness was 40 N/m and tip radius was 10 nm.

2.3.3. Mechanical properties

Tensile tests were carried out according to DIN 53504/S2/50 on dumb-bell shaped specimens using an universal tensile testing machine Zwick Z010 at a constant cross-head speed of 50 mm/min. *E*-modulus was determined in between 0.20 to 0.40% of strain.

2.3.4. Dynamic mechanical thermal analysis (DMTA)

Dynamic mechanical thermal analysis (DMTA) of the samples was carried out using an Eplexor 150N DMTA (Gabo Qualimeter, Ahlden, Germany). Tests were carried out at a frequency of 10 Hz under static strain of 0.50% and dynamic strain of 0.10%. The samples were first cooled to –150°C and then subsequently heated at a rate of 3 K/min over a range of temperature from –150 to 200°C.

2.3.5. Thermogravimetric analysis (TGA)

Thermogravimetric analysis (TGA) and derivative thermogravimetry (DTG) of the neat components and the blends of PDMS/PA12 was measured by using a thermogravimetric analyzer (TGA Q5000, TA Instruments, USA) at a heating rate of 10 K/min under nitrogen atmosphere.

2.3.6. Melt rheological study

The rheological measurements of silicone rubber and polyamide were carried out by an Advanced Rheometric Expansion System (ARES) rheometer (Rheometric Scientific Inc, USA). The torque transducer had a torque range from 0.02 to 2000 g·cm. Parallel plate geometry was applied to the formerly pressed plates with 2 mm thickness and 25 mm diameter. Frequency range was selected between 0.1 to 100 rad/s and strain controlled dynamic frequency sweep test was applied. The measurements were done in N₂ atmosphere at a temperature of 190°C. During each experiment, the temperature maintained at the desired value by constant heating of the sample under nitrogen atmosphere.

2.3.7. Overall cross-link density

The overall crosslink density of silicone rubber was determined on the basis of equilibrium solvent-swelling measurements in toluene by the application of the well-known Flory-Rehner equation at room temperature (Equation (1)):

$$(\nu + PA) = -\frac{1}{V_s} \cdot \frac{\ln(1 - V_r) + V_r + \chi V_r^2}{(V_r)^{1/3} - 0.5V_r} \quad (1)$$

where ν – number of moles of effectively elastic chains per unit volume of PDMS [mol/ml] (crosslink density), PA – PA12, V_s – molar volume of solvent (toluene) [cc/mol], which is 105.74 cc/mol, χ – polymer-swelling agent interaction parameter, taken as 0.45 for both PDMS and toluene at 20°C [33], V_r – volume fraction of rubber in the swollen network and V_r can be expressed as Equation (2):

$$V_r = \frac{1}{A_r + 1} \quad (2)$$

where A_r – ratio of the volume of absorbed toluene to that silicone after swelling.

3. Results and discussion

3.1. Curing characteristics

Cure curves of PDMS cross-linked by different peroxides (1 wt%) at 180°C are shown in Figure 1.

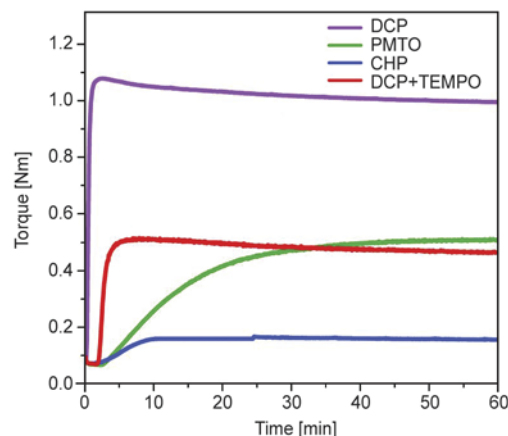


Figure 1. Cure curves of PDMS by different peroxides (1%) at 180°C

From the cure curve it is clear that at 180°C, DCP itself is faster curing peroxide for PDMS than PMTO and CHP. Scorch safety time (t_2), optimum curing time (t_{90}), maximum torque and delta torque values for the three different peroxides are given in the Table 3. From Table 3 it can be observed that at 180°C, scorch safety time and optimum curing time of PDMS for DCP is 0.33 and 0.90 minutes respectively. On the other hand, after using TEMPO, though scorch safety time and optimum curing time of PDMS for DCP were found to increase the cross-linking efficiency becomes lower which is clear from the Figure 1. From Table 3 it can be seen that maximum torque value for (DCP+TEMPO) comes down to 0.541 Nm which is near to half of the torque value (1.079 Nm) of DCP only, whereas the optimum curing time of (DCP+TEMPO) becomes 4.18 minute which is five times (0.90 minute) more than that of DCP only. It indicates that by using TEMPO the scorch safety time can be increased while the cross-linking efficiency of the peroxide would be reduced at the same time.

From Figure 1 it can be noticed that at 180°C PMTO is very slow curing peroxide for the PDMS and its state of cure is also poor. Optimum curing time of PDMS for PMTO is 28.20 minutes which is much higher than that of DCP. For CHP, though the optimum curing time is 18.20 minutes, higher than DCP,

Table 3. Curing characteristics of PDMS by three different peroxides at 180°C

Peroxides	t_2 [min]	t_{90} [min]	Minimum torque [Nm]	Maximum torque [Nm]	Delta torque [Nm]
DCP	0.33	0.90	0.088	1.079	0.991
DCP+TEMPO	1.80	4.18	0.076	0.541	0.465
PMTO	4.50	28.20	0.066	0.512	0.446
CHP	3.80	18.20	0.073	0.168	0.095

Table 4. Curing characteristics of PDMS by three different peroxides at 200°C

Peroxides	t_2 [min]	t_{90} [min]	Minimum torque [Nm]	Maximum torque [Nm]	Delta torque [Nm]
DCP+TEMPO	0.40 = 24 s	1.11 = 66 s	0.068	0.502	0.434
PMTO	1 = 60 s	7.80 = 468 s	0.063	0.515	0.452

but the maximum torque is 0.168 Nm only. On the other hand, from Table 3, it can be observed that the delta torque values for (DCP+TEMPO) and PMTO are 0.465 Nm and 0.446 Nm respectively whereas for CHP the delta torque value is 0.095 Nm only. This clearly implies, though CHP gives better scorch safety than DCP but its cross-linking efficiency is very poor. It means CHP is not the suitable peroxide for the cross-linking of PDMS. Curing characteristics of peroxide mixed PDMS at 200°C has been given in Table 4. From Table 4 it can be observed that curing characteristics of peroxide mixed PDMS follow the same trend. Only time has become 1/4th at 200°C. On the other side the curing characteristics of (DCP+TEMPO) and PMTO are comparable. Therefore, for the next part of the study (DCP+TEMPO) and PMTO have been pursued to develop and characterize the corresponding TPVs.

3.2. Mixing curve

Table 5 demonstrates the formulation of the TPVs which have been studied in this investigation. Mixing curves of the TPVs of PDMS and PA12 have been shown in Figure 2. From this, it can be observed that cross-linking efficiency of (DCP+TEMPO) is higher initially than that of PMTO as it shows very low scorch safety and low optimum curing time. On the other hand, cross-linking efficiency of PMTO is little bit less than (DCP+TEMPO), but it gives much better scorch safety during the preparation of TPV. Therefore, in (DCP+TEMPO) cross-linked TPV torque raises maximum but due to faster decomposition of DCP the rate of fall of torque is also very rapid and within one minute torque has fallen down from 31.56 Nm down to 19.31 Nm. As a result poor

Table 5. Detailed description of the TPVs made from PDMS/PA12 by different peroxides

Sample code	PDMS [wt%]	PA12 [wt%]	Peroxides
Si_PA_D_T	50	50	DCP+TEMPO
Si_PA_P	50	50	PMTO

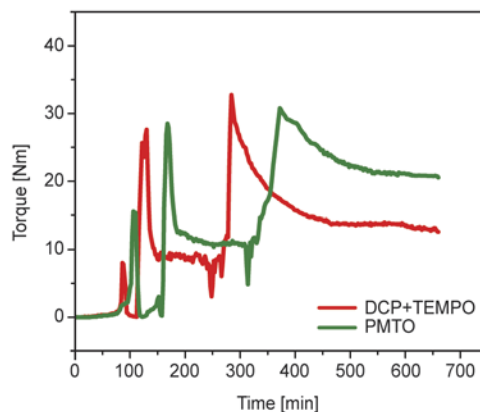
Where Si: silicone rubber (PDMS)

PA: Polyamide (PA12)

D: DCP

T: TEMPO

P: PMTO

**Figure 2.** Mixing curves of TPVs cross-linked by different peroxides

dispersion of the rubber phase has taken place in (DCP+TEMPO) cross-linked TPV which has been discussed later in the morphology study. But for PMTO cross-linked TPV, the rate of fall of torque is not so fast like (DCP+TEMPO) cross-linked TPV. Even after few minutes torque has fallen down from 30.76 to 25.56 Nm. This implies proper dispersion and distribution of the rubber particles. Therefore from the two curves it can be observed that, at high temperature due to faster decomposition of DCP in presence of TEMPO also, cross-linking efficiency of (DCP+TEMPO) becomes lower and state of cross-linking is also becomes poor. Due to that reason torque falls down steeply. On the other side, due to high thermal stability of PMTO, its state of curing is much better than (DCP+TEMPO) which correlates with the higher torque value during TPV preparation.

3.3. Morphology study

Morphology study of two thermoplastic vulcanizates was performed and shown in Figure 3. From the SEM photomicrograph of the two TPVs, it is clear that for the (DCP+TEMPO) cross-linked TPV, cross-linking of the rubber phase has not been taken place fully and wider distribution has not taken place also. (DCP+TEMPO) cross-linked TPV suffers from the faster decomposition of DCP even after the addition of TEMPO, due to the rise of temperature during mixing. Even after addition of TEMPO also scorch safety of DCP increases not so

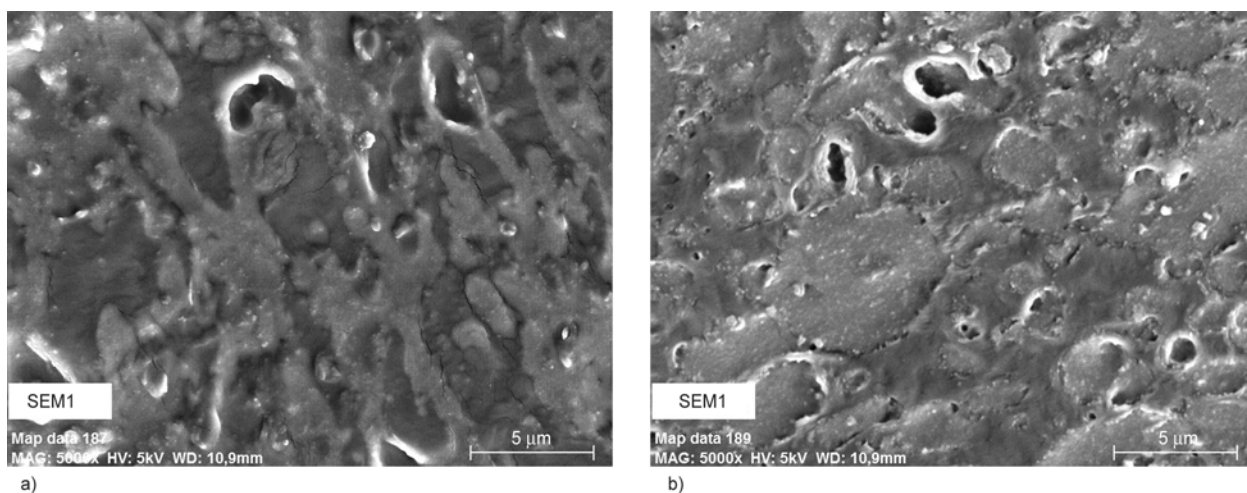


Figure 3. SEM photomicrographs of TPVs cross-linked by a) DCP+TEMPO, b) PMTO

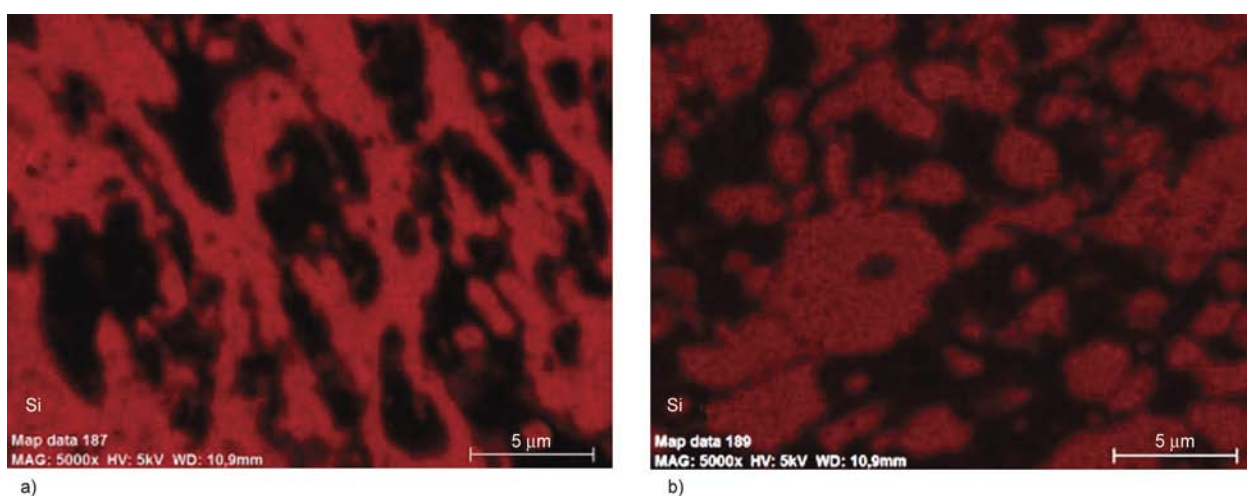


Figure 4. Silicon mapping of TPVs cross-linked by a) DCP+TEMPO, b) PMTO

much which is clear from Table 3. In (DCP+TEMPO) cross-linked TPV, initially the cross-linking rate of DCP was higher but due to the faster decomposition of DCP at high temperature dispersion and distribution of the rubber phase has not taken place properly which results in a co-continuous phase morphology rather than in the dispersed phase one, as shown in Figure 3a.

On the other hand, PMTO is new, high temperature peroxide which extends the temperature range of cross-linking. Scorch safety time and optimum curing time for PMTO is very high which is shown in Table 3. As a result, faster decomposition of PMTO has not taken place, even after the rise of temperature during mixing. Therefore, though the rate of cross-linking of PMTO is little bit lower than that of (DCP+TEMPO), dispersion and distribution of the rubber phase has taken place properly which results dispersed phase morphology in the final TPV. However, from Figure 3b it can also be observed there is

more or less wider distribution of the cross-linked rubber particles in the polyamide matrix and the particle size of the rubber phase varies in the 1–4 μm range. The same picture can also be observed from the silicon mapping of the consequent TPVs which is shown in Figure 4.

Similar morphology was observed from the atomic force microscopy (AFM) picture of a TPE and TPV system which is shown in Figure 5. From the top view of the TPE and TPV it is clearly seen that in case of TPE the two phase forms the co-continuous structure and there is no peak and hills, which can be seen from the Figure 5a. But for the picture of TPV it can be easily observed that the rubber phase is properly cross-linked and that is why rubber phase has appeared as peaks and hills in the Figure 5b.

3.4. Mechanical properties

Mechanical properties of the various TPVs are given in Table 6. From the mechanical properties of

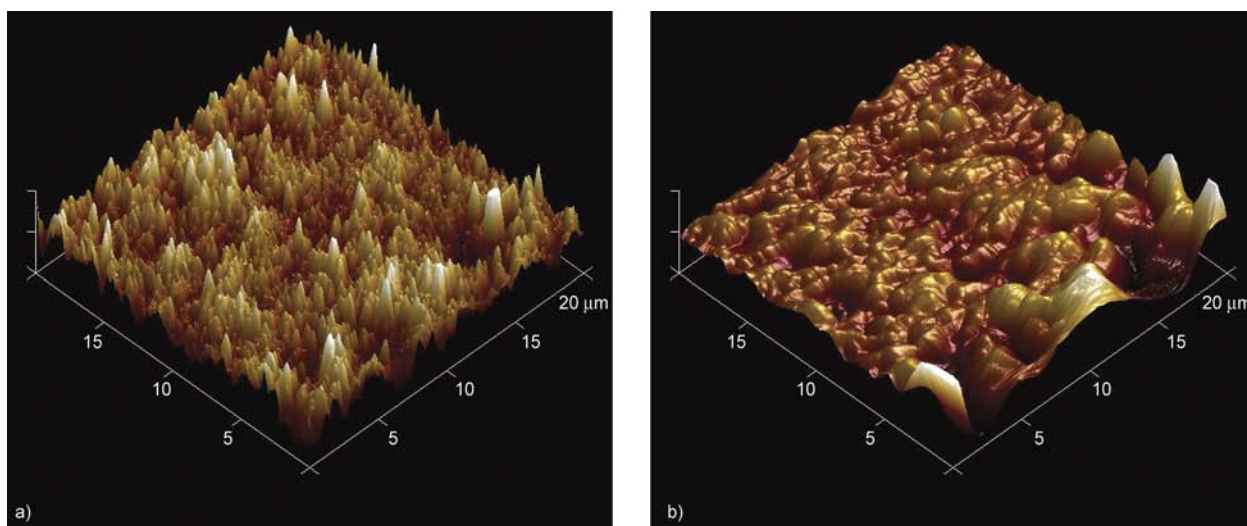


Figure 5. Top view image of a) TPE and b) TPV (PMTO cross-linked)

Table 6. Mechanical properties of the TPVs of PDMS/PA12

Sample code	Young's modulus, E_t [MPa]	Tensile strength [MPa]	Elongation at break [%]	Hardness [Shore D]
Si_PA_D_T	649±47	19.6±1.9	51±8	39±3
Si_PA_P	785±30	26.5±0.6	127±6	59±4

the TPVs it can be clearly observed that TPV cross-linked by PMTO gives better result from tensile strength, elongation and hardness point of view. Tensile strength of PMTO cross-linked TPV is 26.5 MPa whereas for the (DCP+TEMPO) cross-linked TPV it is 19.6 MPa. Elongation at break of the PMTO cross-linked TPV is 127% whereas for the (DCP+TEMPO) cross-linked TPV 51% only. On the other hand, hardness of PMTO cross-linked TPV is 59 Shore D whereas for (DCP+TEMPO) cross-linked TPV it is 39 Shore D. Tension set of PMTO cross-linked TPV samples is 21%. Due to co-continuous phase morphology in (DCP+TEMPO) cross-linked TPV, mechanical properties of (DCP+TEMPO) cross-linked TPV are poor whereas mechanical properties of PMTO cross-linked TPV are superior because of dispersed phase morphology and wider distribution of the rubber particles. This implies that in presence of PMTO, rubber phase gets fully cross-linked in PMTO cross-linked TPV which correlates with the higher value of overall cross-link density which has been shown later.

3.5. Dynamic mechanical thermal analysis (DMTA)

Storage modulus of the two thermoplastic vulcanizates are shown in Figure 6. It can be observed that at relatively low temperature the storage modulus

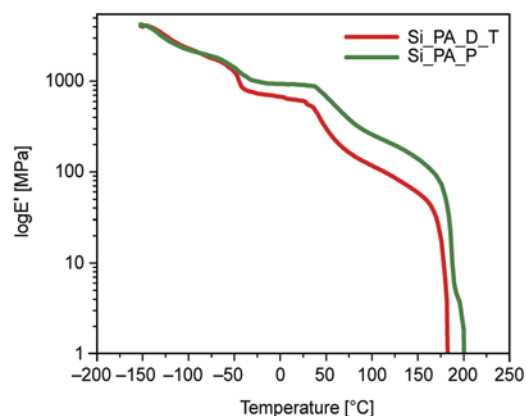
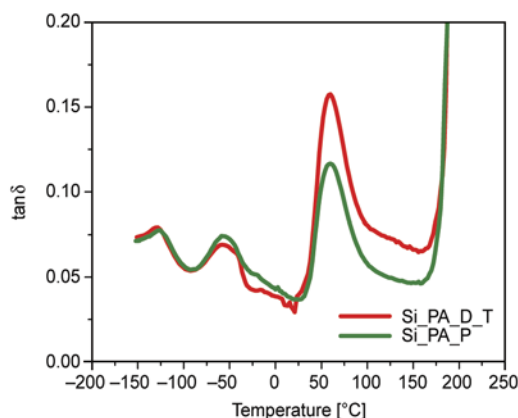


Figure 6. Storage modulus (E') of TPVs as a function of temperature

(E') of both the TPVs are almost same. The rubbery plateau region is found between -45 to $+55^\circ\text{C}$. From Figure 6, it can be noticed that in the rubbery plateau region storage modulus of PMTO cross-linked TPV are higher than that of the (DCP+TEMPO) cross-linked TPV. This clearly indicates the higher degree of cross-linking in PDMS rubber phase in PMTO cross-linked TPV over (DCP+TEMPO) cross-linked one. Even at higher temperature the storage modulus value of PMTO cross-linked TPV is found higher than the (DCP+TEMPO) cross-linked TPV. Therefore, mechanical properties and overall cross-link density of the PMTO cross-linked TPV were found superior to the (DCP+TEMPO) cross-linked one. Storage modulus and $\tan\delta$ values of all the TPVs were shown in the Table 7. Figure 7 illustrates the $\tan\delta$ plot as function of temperature and demonstrates that there are two major transitions: the T_g of PDMS at around -120°C and that of PA at around $+55^\circ\text{C}$. Another transition is at

Table 7. Storage modulus (E') and $\tan \delta$ values of TPVs

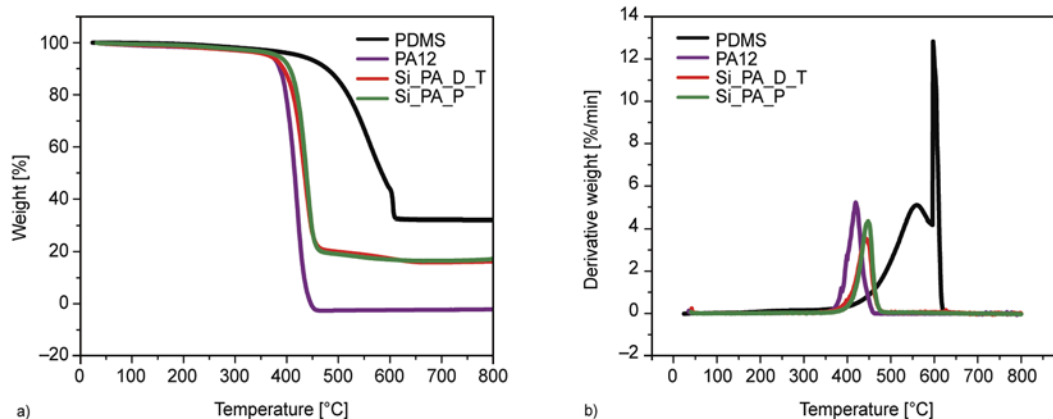
Sample code	$E' \cdot 10^2$ at 25°C [MPa]	$\tan \delta$ at -120°C	$\tan \delta$ at 55°C
Si_PA_D_T	6.19	0.075	0.154
Si_PA_P	9.02	0.073	0.115

**Figure 7.** $\tan \delta$ of TPVs as a function of temperature

around -50°C , which is the ductile brittle transition temperature of the PDMS. It can also be clearly observed that the T_g of PA12 has been shifted from 55°C to the higher value for the TPVs due to interaction between the two phases. The lower $\tan \delta$ value of the PMTO cross-linked TPV at T_g of silicone rubber, indicates the higher cross-linking of the PDMS rubber phase and lesser damping characteristics of the TPVs.

3.6. Thermogravimetric analysis (TGA)

Thermogravigrams and derivatograms of neat PDMS, PA12 and TPVs are shown in the Figure 8a and 8b respectively and the data are presented in Table 8. From the table, it is clearly observed that the initial decomposition temperature (T_i) of PDMS is at 476°C , whereas for the PA12 it is rather low at 380°C . Similarly the 50% weight loss temperature for PDMS is 584°C whereas for PA12 it is 415°C

**Figure 8.** a) Thermogravigrams and b) derivatograms of PDMS, PA12 and TPVs**Table 8.** TGA data of PDMS, PA12 and TPVs

Sample code	Initial decomposition temperature, T_i [°C]	50% weight loss temperature [°C]	Residue at 600°C [%]
PDMS	476	584	43.900
PA12	380	415	0.045
Si_PA_D_T	410	436	15.250
Si_PA_P	432	465	17.980

only. But considering the percentage residue at 600°C , it can be clearly stated that at 600°C PA12 decomposes fully and that is why percent residue is very less, whereas at 600°C the percent residue for PDMS is 43.9%. It indicates that at higher temperature say 600°C also decomposition of PDMS does not take place fully and for PDMS there is always higher percentage of residue because of presence of silica filler into the PDMS. Amongst the TPVs, T_i is the highest for the PMTO cross-linked TPV. Similarly 50% weight loss temperature and % residue at 600°C for the PMTO cross-linked TPV are 465°C and 17.98% respectively, which are 436°C and 15.25% for the (DCP+TEMPO) cross-linked TPV. Thus it can be concluded that the thermal stability of PMTO cross-linked TPV is higher and this has been taken place due to the higher cross-linking efficiency of the PMTO at higher temperature.

3.7. Melt rheological study

Complex modulus (G^*) as a function of frequency at 190°C for TPVs are shown in the Figure 9. From the figure it can be clearly observed that with increasing frequency the complex modulus (G^*) of the TPVs is increasing. But the increase in complex modulus is maximum in the case of TPV which is cross-linked by PMTO. The complex modulus (G^*) values at a frequency of 100 rad/s and the complex viscos-

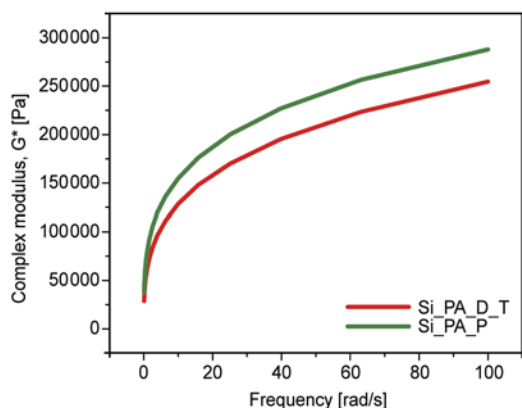


Figure 9. Complex modulus (G^*) of TPVs as a function of frequency at 190°C

Table 9. Complex modulus (G^*) and complex viscosity (η^*) of TPVs

Sample code	$G^* \cdot 10^5$ at 100 rad/s [Pa]	$\eta^* \cdot 10^3$ at 1 rad/s [Pa·s]
Si_PA_D_T	2.55	62.50
Si_PA_P	2.94	69.09

ity (η^*) values at a frequency of 1 rad/s are given in the Table 9. From the table also it is clear that the TPV, cross-linked by PMTO has given the maximum value of complex modulus (G^*) which is $2.94 \cdot 10^5$ Pa, higher than the (DCP+TEMPO) cross-linked TPV.

From the Figure 10 it is seen that complex viscosity (η^*) of TPVs decreases as a function of frequency, indicating typical pseudoplastic behaviour. It can also be demonstrated that higher cross-linking has taken place in the TPV cross-linked by PMTO. From the figure it is clear that complex viscosity (η^*) of the PMTO cross-linked TPV is higher than the (DCP+TEMPO) cross-linked TPV throughout the frequency range. So from the Table 9 also it is clear that the TPV, cross-linked by PMTO has given

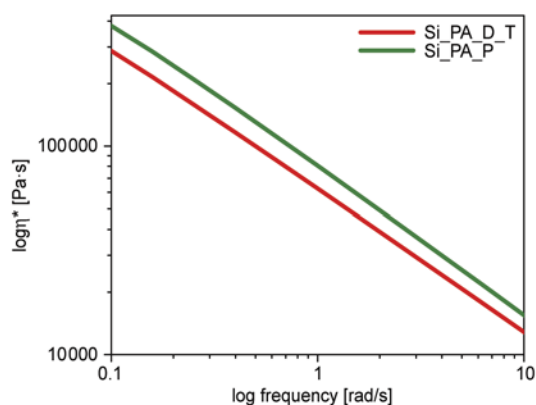


Figure 10. Complex viscosity (η^*) of TPVs as a function of frequency at 190°C

the maximum value of complex viscosity (η^*) which is $69.09 \cdot 10^3$ Pa·s, higher than the (DCP+TEMPO) cross-linked TPV. So it can be concluded that maximum cross-linking also has been taken place by the TPV which is cross-linked by PMTO and that has been supported also through the determination of overall cross-link density of the TPVs discussed next.

3.8. Overall cross-link density

From the Figure 11 it is clearly observed that the overall cross-link density ($v+PA$) of the PMTO cross-linked TPV is higher than that of the (DCP+TEMPO) cross-linked TPV. For the TPV which are cross-linked by (DCP+TEMPO), ($v+PA$) value is $17.1 \cdot 10^{-4}$ mol/mL. On the other hand, it can be clearly seen that the ($v+PA$) value of the PMTO cross-linked TPV is $56.8 \cdot 10^{-4}$ mol/mL higher than that of the (DCP+TEMPO) cross-linked TPV. This also implies that in presence of PMTO, cross-linking of the rubber phase has been taken place in the PMTO cross-linked TPV whereas for the (DCP+TEMPO) cross-linked TPV cross-linking of the rubber phase has not taken place properly.

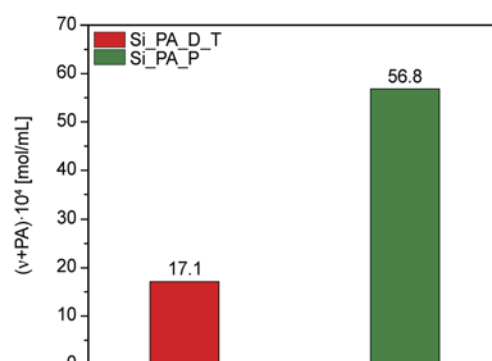


Figure 11. Overall cross-link density of the TPVs

4. Conclusions

A detailed study has been made in this investigation to develop a novel TPV based on PDMS and PA12. For the development of TPV three structurally different peroxides (DCP, PMTO and CHP) have been explored and out of these three peroxides PMTO cross-linked TPV gave superior properties from all respective points of view. During dynamic vulcanization PMTO gives a better scorch safety than the other two peroxides. That is why during dynamic vulcanization the dispersion of the rubber particles also takes place properly and the domain size also

becomes smaller. This is supported by SEM, EDX studies and AFM as well which clearly show that the finer dispersion is only achievable in case of PMTO cross-linked TPV. Moreover, there is evidence that the co-continuous non-reactive blend morphology has been changed into a dispersed one with cross-linked PDMS-domains embedded in the PA12 matrix. Accordingly mechanical properties of the PMTO cross-linked TPV are superior than the (DCP+TEMPO) cross-linked TPV. This can again be attributed to the presence of fine dispersed cross-linked PDMS domains in case of the dynamic vulcanization with PMTO. This is reflected also in the dynamic mechanical properties, both in the solid as well in the molten state, where the PMTO based TPV always showed a higher storage modulus in junction with lower $\tan \delta$ values. These findings indicate also higher overall cross-link density of the PMTO cross-linked TPV in comparison to the (DCP+TEMPO) based one. Accordingly the thermal stability of the PMTO based TPV is also higher, as substantiated by TGA-investigations. Considering all the results, it can be concluded that for further development of PDMS/PA12 based TPV, PMTO is a suitable peroxide.

Acknowledgements

We thank Mrs. M. Auf der Landwehr (IPF Dresden) for the morphology characterization by means of SEM-EDX. Thanks to D. Willink of Akzo Nobel Polymer Chemicals B.V. (Amersfoort, NL) for providing free samples of Trigonox[®] 311. Also thanks to Dr. A. Das, Dr. A. Leuteritz, Prof. U. Wagenknecht, R. Jurk and H. Kunath for valuable discussions and support.

References

- [1] Karger-Kocsis J.: Thermoplastic rubbers via dynamic vulcanization. in 'Polymer blends and alloys' (eds.: Shonaike G. O., Simon G. P.) Marcel Dekker, New York 125–153 (1999).
- [2] Babu R. R., Naskar K.: Recent developments on thermoplastic elastomers by dynamic vulcanization. *Advances in Polymer Science*, **239**, 219–247 (2011). DOI: [10.1007/12_2010_97](https://doi.org/10.1007/12_2010_97)
- [3] Paul D. R., Bucknall C. B.: *Polymer blends*. Wiley, New York (2000).
- [4] Utracki L. A., Favis B. D.: *Polymer alloys and blends-Thermodynamics and rheology*. Hanser, Munich (1990).
- [5] De S. K., Bhowmick A. K.: *Thermoplastic elastomers from rubber plastic blends*. Horwood, London (1990).
- [6] Holden G., Legge N. R., Schroeders H. E.: *Thermoplastic elastomer: A comprehensive review*. Hanser, Munich (1987).
- [7] Bousmina M., Muller R.: Rheology/morphology/flow conditions relationships for polymethylmethacrylate/rubber blend. *Rheologica Acta*, **35**, 369–381 (1996). DOI: [10.1007/BF00403538](https://doi.org/10.1007/BF00403538)
- [8] Abdou-Sabet S., Puydak R. C., Rader C. P.: Dynamically vulcanized thermoplastic elastomers. *Rubber Chemistry and Technology*, **69**, 476–494 (1996). DOI: [10.5254/1.3538382](https://doi.org/10.5254/1.3538382)
- [9] Gessler A. M., Haslett W. H.: Process for preparing a vulcanised blend of crystalline polypropylene and chlorinated butyl rubber. U.S. Patent 3037954, USA (1962).
- [10] Fisher W. K.: Thermoplastic blend of partially cured monoolefin copolymer rubber and polyolefin plastic. U.S. Patent 3862106, USA (1973).
- [11] Coran A. Y., Das B., Patel R. P.: Thermoplastic vulcanizates of olefin rubber and polyolefin resin. U.S. Patent 4130535, USA (1978).
- [12] Coran A. Y., Patel R.: Rubber-thermoplastic compositions. Part I. EPDM-polypropylene thermoplastic vulcanizates. *Rubber Chemistry and Technology*, **53**, 141–150 (1980). DOI: [10.5254/1.3535023](https://doi.org/10.5254/1.3535023)
- [13] Naskar K., Noordermeer J. W. M.: Influence of various peroxides in PP/EPDM thermoplastic vulcanizates at varied blend ratios. *Journal of Elastomers and Plastics*, **38**, 163–180 (2006). DOI: [10.1177/0095244306060215](https://doi.org/10.1177/0095244306060215)
- [14] Naskar K., Noordermeer J. W. M.: Dynamically vulcanized PP/EPDM blends: Multifunctional peroxides as crosslinking agents – Part I. *Rubber Chemistry and Technology*, **77**, 955–971 (2004). DOI: [10.5254/1.3547862](https://doi.org/10.5254/1.3547862)
- [15] Naskar K., Gohs U., Wagenknecht U., Heinrich G.: PP-EPDM thermoplastic vulcanisates (TPVs) by electron induced reactive processing. *Express Polymer Letters*, **3**, 677–683 (2009). DOI: [10.3144/expresspolymlett.2009.85](https://doi.org/10.3144/expresspolymlett.2009.85)
- [16] Basuli U., Chaki T. K., Naskar K.: Influence of Engage[®] copolymer type on the properties of Engage[®]/silicone rubber-based thermoplastic dynamic vulcanizates. *Express Polymer Letters*, **2**, 846–854 (2008). DOI: [10.3144/expresspolymlett.2008.99](https://doi.org/10.3144/expresspolymlett.2008.99)
- [17] Chatterjee K., Naskar K.: Development of thermoplastic elastomers based on maleated ethylene propylene rubber (m-EPM) and polypropylene (PP) by dynamic vulcanization. *Express Polymer Letters*, **1**, 527–534 (2007). DOI: [10.3144/expresspolymlett.2007.75](https://doi.org/10.3144/expresspolymlett.2007.75)
- [18] Babu R. R., Singha N. K., Naskar K.: Interrelationships of morphology, thermal and mechanical properties in uncrosslinked and dynamically crosslinked PP/EOC and PP/EPDM blends. *Express Polymer Letters*, **4**, 197–209 (2010). DOI: [10.3144/expresspolymlett.2010.26](https://doi.org/10.3144/expresspolymlett.2010.26)

- [19] Rajeshbabu R., Gohs U., Naskar K., Mondal M., Wagenknecht U., Heinrich G.: Electron-induced reactive processing of poly(propylene)/ethylene–octene copolymer blends: A novel route to prepare thermoplastic vulcanizates. *Macromolecular Materials and Engineering*, **297**, 659–669 (2012).
DOI: [10.1002/mame.201100209](https://doi.org/10.1002/mame.201100209)
- [20] McNally T., McShane P., Nally G. M., Murphy W. R., Cook M., Miller A.: Rheology, phase morphology, mechanical, impact and thermal properties of polypropylene/metallocene catalysed ethylene 1-octene copolymer blends. *Polymer*, **43**, 3785–3793 (2002).
DOI: [10.1016/S0032-3861\(02\)00170-2](https://doi.org/10.1016/S0032-3861(02)00170-2)
- [21] Da Silva A. L. N., Rocha M. C. G., Coutinho F. M. B., Bretas R., Scuracchio C. J.: Rheological, mechanical, thermal, and morphological properties of polypropylene/ethylene-octene copolymer blends. *Journal of Applied Polymer Science*, **75**, 692–704 (2000).
DOI: [10.1002/\(SICI\)1097-4628\(20000131\)75:5<692::AID-APP12>3.0.CO;2-Y](https://doi.org/10.1002/(SICI)1097-4628(20000131)75:5<692::AID-APP12>3.0.CO;2-Y)
- [22] Giri R., Naskar K., Nando G. B.: Effect of electron beam irradiation on the structure property relationship of LLDPE and PDMS rubber blends. *Rubber Fibres Plastics International*, **6**, 97–107 (2011).
- [23] Rajeshbabu R., Gohs U., Naskar K., Thakur V., Wagenknecht U., Heinrich G.: Preparation of polypropylene (PP)/ethylene octene copolymer (EOC) thermoplastic vulcanizates (TPVs) by high energy electron reactive processing. *Radiation Physics and Chemistry*, **80**, 1398–1405 (2011).
DOI: [10.1016/j.radphyschem.2011.07.001](https://doi.org/10.1016/j.radphyschem.2011.07.001)
- [24] Mani S.: Fundamentals aspects of crosslinking control of PDMS rubber at high temperatures using Tempo Nitroxide. PhD thesis, Claude Bernard University Lyon 1, France (2011).
- [25] Chang C-L., Don T-M., Lee H. S-J., Sha Y-O.: Studies on the aminolysis of RTV silicone rubber and modifications of degradation products. *Polymer Degradation and Stability*, **85**, 769–777 (2004).
DOI: [10.1016/j.polymdegradstab.2003.12.001](https://doi.org/10.1016/j.polymdegradstab.2003.12.001)
- [26] Mani S., Cassagnau P., Bousmina M., Chaumont P.: Morphology development in novel composition of thermoplastic vulcanizates based on PA12/PDMS reactive blends. *Macromolecular Materials and Engineering*, **296**, 909–920 (2011).
DOI: [10.1002/mame.201000406](https://doi.org/10.1002/mame.201000406)
- [27] Mark J. E., Allcock H. R., West R.: *Inorganic polymers*. Oxford University Press, New York (2005).
- [28] Santra R. N., Mukunda P. G., Nando G. B., Chaki T. K.: Thermogravimetric studies on miscible blends of ethylene-methyl acrylate copolymer (EMA) and polydimethylsiloxane rubber (PDMS). *Thermochimica Acta*, **219**, 283–292 (1993).
DOI: [10.1016/0040-6031\(93\)80505-5](https://doi.org/10.1016/0040-6031(93)80505-5)
- [29] Arkema: Market research showed that Rilsan PA11 and Rilsan PA12 are highly valued by major car OEMs. p2 (2007).
- [30] Dorn M.: Modification of molecular weight and flow properties of thermoplastics. *Advances in Polymer Technology*, **5**, 87–97 (1985).
DOI: [10.1002/adv.1985.060050203](https://doi.org/10.1002/adv.1985.060050203)
- [31] Mani S., Cassagnau P., Bousmina M., Chaumont P.: Rheological modelling of the free-radical crosslinking of PDMS rubber in the presence of TEMPO nitroxide. *Polymer*, **51**, 3918–3925 (2010).
DOI: [10.1016/j.polymer.2010.06.029](https://doi.org/10.1016/j.polymer.2010.06.029)
- [32] Mani S., Cassagnau P., Bousmina M., Chaumont P.: Cross-linking control of PDMS rubber at high temperatures using TEMPO nitroxide. *Macromolecules*, **42**, 8460–8467 (2009).
DOI: [10.1021/ma901521v](https://doi.org/10.1021/ma901521v)
- [33] Alvarez Grima M. M.: Novel co-agents for improved properties in peroxide cure of saturated elastomers. PhD Thesis, University of Twente, Enschede (1992).

Non-uniform dispersion of toughening agents and its influence on the mechanical properties of polypropylene

Z. Li, C. M. Liu, H. L. Liu, K. Wang, Q. Fu*

College of Polymer Science and Engineering, State Key Laboratory of Polymer materials Engineering, Sichuan University, 610065 Chengdu, China

Received 30 September 2013; accepted in revised form 25 November 2013

Abstract. To achieve excellent properties of polymer blends and composites, good dispersion and uniform distribution of second component or filler in the matrix are often required. However, more and more evidences reveal that uniform distribution is not always the best. To further prove this idea, in this work, we purposely designed and prepared different samples of isotactic polypropylene (iPP)/elastomer or iPP/ β -nucleating agent with uniform and non-uniform distribution of the modifiers via stacking the blending sheets in different sequence. It was found that for a given amount of toughening agent, the impact strength of polymer blends with non-uniform distribution of elastomer or β -nucleating agent could be much higher than its uniformly dispersed counterpart, while the tensile strength and tensile modulus remain relatively constant. The instrumented impact test confirmed that among the samples with different layered structures, the absorbed energy during crack initiation differs little from each other. Whereas absorbed energy during crack propagation process shows the same trend as final impact strength, making it the controlling parameter during the impact process. When cracks are initiated at higher toughening agents content side, the relatively smooth fracture surfaces near the crack edge area proved that they absorb small energy and the adjacent inner part showed obviously plastic deformation, corresponding to higher energy absorption. Our work demonstrates again that design and control of the hierarchical structure of polymer articles is vital for high performance properties and non-uniform distribution of filler could be much better than the uniform distribution.

Keywords: mechanical properties, poly(ethylene-1-octene), nucleating agents, heterogeneous distribution

1. Introduction

In the last decades, the development of polymeric matrix composites mainly focused on uniformly dispersed polymeric composites (UDPCs). The conventional view believes that the uniform distribution of the second component like nano-particles, elastomers, fibers and so forth contributes to the better properties of the composites. Undeniably, scientific researchers have achieved high performance of polymeric composites by this guiding ideology. However, as the rapid development of science and technology, the material application places higher demands on polymeric composites and the homogeneously distributed components not always yield

the most satisfactory effect [1–3]. Besides, their engineering and structural applications are restricted due to high production cost of nanoscale reinforcing materials. Heterogeneous spatial distribution of two or more components along the thickness of the product may have better performance characteristics such as thermal stress relaxation, adhesive property and mechanical properties as compared to the same material in homogeneous compositional state and this gives scientists a wide range of possibilities to manipulate the properties of these materials depending on requirements and future applications [4]. For example, Bafekrpour *et al.* [5] realized a heterogeneous distribution of graphite in phenolic matrix

*Corresponding author, e-mail: qiangfu@scu.edu.cn
© BME-PT

using powder stacking and compression molding techniques. The authors reported that the nanocomposites with the highest graphite content layer on the top and bottom surfaces and the lowest in the center, showed the highest improvement of thermo-mechanical properties and creep recovery among all filler distribution conditions. Lee and Jang [6] found that, if the face of a sample with high glass fiber content was loaded, the flexural strength and the impact energy of the composite showed improved values by comparison with those of the isotropic composite. Wang *et al.* [7] prepared a gradient polymer with a progressive change in sulfur content along the thickness direction and the composites showed a broad damping temperature range spanning over 100°C, which is far better than the isotropic ones with the same sulfur density.

Based on the above, we are wondering if the concept of non-uniform dispersion can be used in the isotactic polypropylene (iPP) toughening area to further enhance its impact strength. It has been long known that PP is a semi-crystalline polymer and has been widely used. But its toughness, and in particular its notched toughness, is insufficient for PP to be used as an engineering plastic. To solve the problem, elastomers like poly (ethylene-1-octene) (POE) and β -nucleating agents (NA) are the two broad types of modifiers to achieve the high impact resistance of PP [8–20]. PP is toughened by POE and NA through totally different mechanism: the former relies on the energy absorption of elastomer particles when impacting whereas NA can promote the growth of β -crystals instead of the α -form and β -nucleated PP shows better impact resistance [21–25]. Generally the incorporation of the modifiers always causes decrease in the tensile properties. So the POE and NA are always kept below a certain limit [26–27]. In this study, we demonstrate for the first time the design and fabrication of non-uniformly dispersed polymeric composites (N-UDPCs) of PP/POE and PP/NA system by sheet stacking and compression molding. Four N-UDPCs and UDPCs with the same thickness and total modifier contents were fabricated to evaluate the effect of spatial distribution of toughening agents on the mechanical properties.

The impacting process and fracture morphology were also investigated and characterized.

2. Experimental

2.1. Materials

iPP T30S (Dushanzi, China) with density (ρ) = 0.91 g/cm³, was the commercial product of Dushanzi Co. Ltd, China. The weight-average molecular weight (M_w) of the iPP was 3.9·10⁵ g/mol and the molecular weight distribution (MWD) was 4.6. POE 8150 with ρ = 0.868 g/cm³ was supplied by Du Pont Dow Elastomers Co. Ltd., USA. The octene content was 25 wt%. The rare earth β -nucleating agent was kindly supplied by Winner Functional Materials Co. (Foshan, Guangdong, China). Its composition is hetero-nuclear dimetal complexes of lanthanum and calcium containing some specific ligands [28].

2.2. Sample fabrication

PP samples with varied POE contents were melt compounded in a co-rotating twin screw extruder (TSSJ-25 co-rotating twin-screw extruder, China) with the setting temperatures of 160–200°C from hopper to die and the screw speed of 120 rpm. After making droplets, the pellets were dried at 80°C for 12 h. The composite sheets were moulded by hot pressing at 200°C. The POE content in the various composites was 0, 10, and 20% by weight. The thickness of each composite sheet was about 1.8 mm.

To obtain the non-uniformly dispersed polymeric composites (N-UDPCs) of PP/POE, composites with varying POE content through the thickness of the specimen were manufactured. Four sheets were stacked and heated to 200°C and compression moulded. The moulding pressure was 0.6 MPa and this pressure was maintained during cooling (–5°C/min) to room temperature, guaranteeing the thickness of all the samples being ca 7 mm. A range of compositions with different stacking sequence were made as illustrated in Figure 1. All the samples are prepared with four layers with same POE content of 10 wt%. POE10 is uniformly dispersed polymeric composites (UDPCs) with the average mass fraction of POE in PP (i.e. 10 wt%). 2PP/

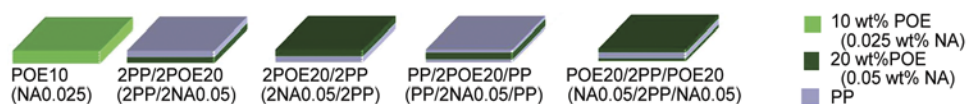


Figure 1. Illustrations of different layered structure of PP/POE and PP/NA composites

2POE20 has two layers of neat PP on the top and 20 wt% of POE in the bottom two layers. 2POE20/2PP has a reverse compositional change in comparison to 2PP/2POE20. PP/2POE20/PP has two layers of 20 wt% POE in the core and neat PP layer on the top and bottom. In contrast, POE20/2PP/POE20 has neat pp in the core and 20 wt% POE on the side. Similarly, N-UDPCs and UDPCs of PP/NA with 0.05 wt% NA were fabricated according to the same procedure. It shares the same illustration as PP/POE composites does in Figure 1.

To make sure that the individual layers could be well fused and avoid interlayer defects, two measures were taken. The first is that control the moulding pressure at 0.6 MPa during the cooling process. Another is that the inner air pressure was kept at -0.1 MPa to avoid the bubbles between different layers.

2.3. Characterizations and measurements

Mechanical tests

A SANS universal testing machine (Shenzhen, China) was used to measure the tensile properties, with a tensile rate of $50 \text{ mm}\cdot\text{min}^{-1}$. Tensile measurements were made on rectangular specimens ca 7 mm wide (the thickness of the laminated molded samples), 2 mm thick and with gauge length of 60 mm. A crosshead speed of 50 mm/min was applied to determine the tensile strength, elongation at break and tensile modulus.

Conventional Izod tests can provide information on the impact resistance of materials during high strain rate deformation; no other valuable data can be obtained except the final impact strength, especially in the inhomogeneous filler distribution system [29, 30]. Therefore, in this experiment, instrumented falling weight impact test (IFWIT) was used to detect the impact force changing trend versus displacement, establishing the correlation between filler distribution and impact strength

IFWIT was performed on a TCJ-25 (Jilin Taihe Tester Co. Ltd, China) machine. $80\times 7\times 4$ mm specimens were cut from the laminated molded samples as illustrated in Figure 2a, taken POE20/2PP/POE20 for instance. The specimens were notched on the top side according to Figure 1 with 0.3 mm notch depth. To be clarified, 2POE20/2PP iPP means the PP Side was notched whereas 2POE20/2PP iPOE means POE20 has the breach. Impact testing was carried out at 3.5/s velocity and 7.5 J maximal

energy. The samples were tested at room temperature (24°C).

Figure 2b also shows a typical force–deflection curve derived from an impact test on a PP/POE composite. In a typical force-displacement curve, the peak force (F_m) is the maximum force that the specimen can sustain on fracture, indicating the beginning of significant damage. The associated energy absorbed up to this point is symbolized by E_i . It is calculated by integrating the area under the load-displacement curve and represents the energy to initiate crack. After F_m , the dropping off in force indicates crack propagation. E_p represents the energy absorption in this phase. The total energy absorption E_t is $E_t = E_i + E_p$. This is the area under the entire force-deflection curve [31, 32].

Scanning electron microscope (SEM)

The scanning electron microscopy (SEM) experiments were performed using an FEI Inspect F SEM instrument with an acceleration voltage of 20 kV. For morphological observations the PP/POE samples were firstly cryo-fractured in liquid nitrogen and then etched chemically in xylene at 60°C for 40 min, followed by washing and drying. Impact fractured surface of both the PP/POE and PP/NA specimens were also investigated. All samples were sputter-coated with gold powder before test.

Differential scanning calorimetry (DSC)

The thermal analysis of the samples was conducted using a Perkin-Elmer pyris-1 DSC with nitrogen as the purge gas, calibrated by indium. The mass of tested sample was about 5 mg. In order to prove the anisotropic structure, the samples cut from the different layers of PP/NA specimens were directly heated from 30 to 200°C with a rate of $10^\circ\text{C}/\text{min}$ and held for 5 min to eliminate any thermal history, and then cooled to 50°C at the rate of $10^\circ\text{C}/\text{min}$. Thereafter, the specimens were heated a gain to the melting point at a rate of $10^\circ\text{C}/\text{min}$. The relative content of β -form estimated by DSC melting curve is defined as K_β^* and calculated from the Equation (1):

$$K_\beta^* = \frac{X_\beta}{X_\alpha + X_\beta} \quad (1)$$

where X_α and X_β are the relative crystallinity of the α - and β -form, respectively and could be calculated separately according to Equation (2):

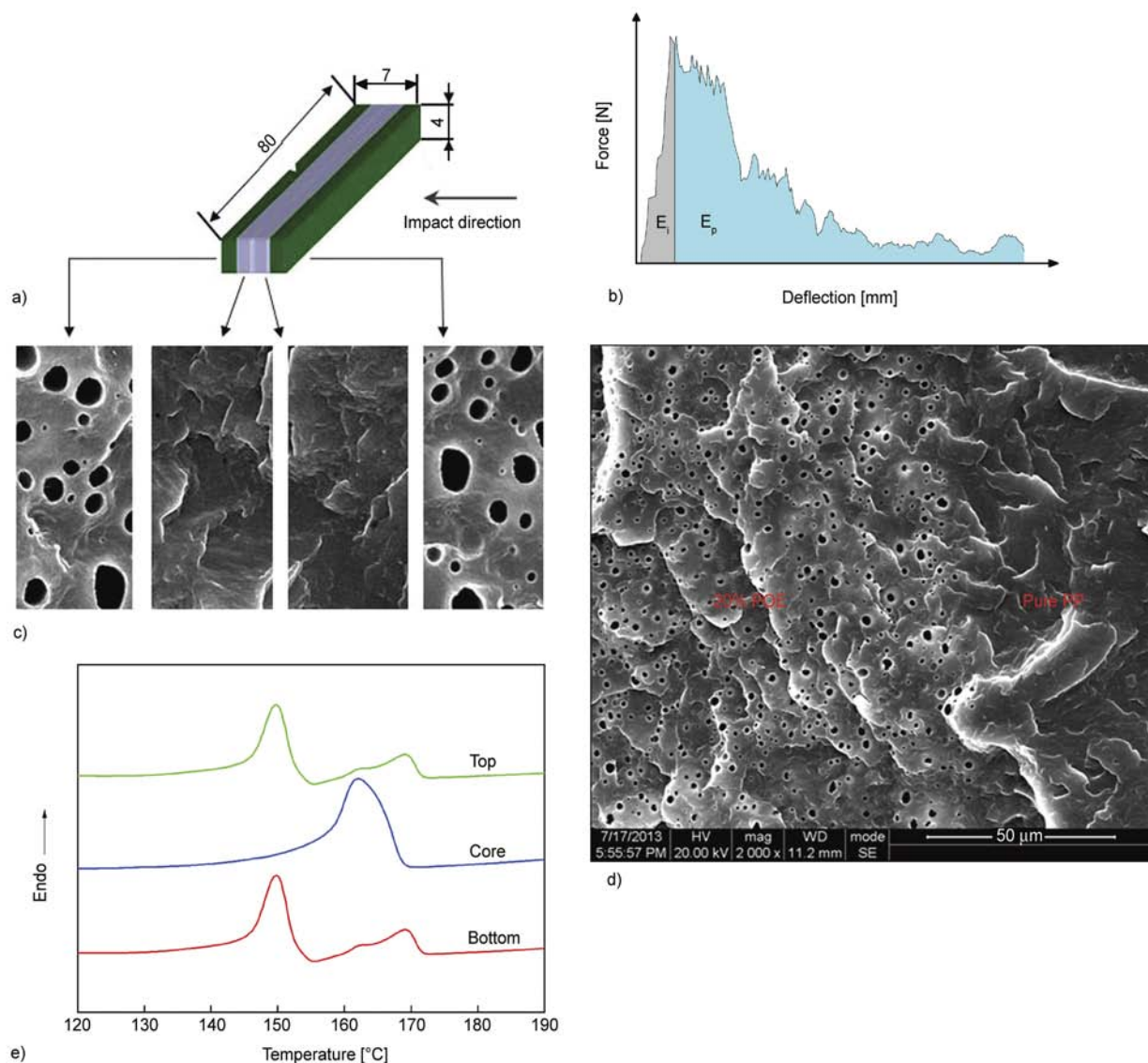


Figure 2. (a) The sketch of layered structure of POE20/2PP/POE20, (b) schematic diagram of Charpy impact measurement and schematic diagram of E_i and E_p of a force–deflection curve, (c) structure morphology across the thickness of the specimen of POE20/2PP/POE20, (d) the interfaces of POE20/2PP/POE20, (e) DSC heating curves of the samples cut from different part of NA0.05/2PP/NA0.05 specimen

$$X_i = \frac{\Delta H_i}{\Delta H_i^0} \quad (2)$$

where ΔH_i is the calibrated specific fusion heat of either α -form or β -form, and ΔH_i^0 is the standard fusion heat of either α - or β -form, which is 177 J/g for the α form and 168.5 J/g for the β -form [33].

3. Results and discussion

3.1. Specimen structure

The sandwich structure of PP/POE system was detected by SEM. Figure 2 c shows different structure morphology across the thickness of the specimen and Figure 2d illustrates the interface of POE20/2PP/POE20. The layers were homogeneous and

had clear interlayer boundaries. Despite high concentrations of POE, no interlayer defects, delamination or cracking was observed. It proved that the vacuum compression molding successfully drive the bubbles away during melting and cooling process. From the etched SEM figure, it is also clear that the POE domains were well dispersed in the PP matrix. Because NA0.05 merged well with PP, the layered structure is hardly seen from SEM. DSC was used to discriminate the different layers. As the samples taken from NA0.05/PP/NA0.05, The DSC melting thermograms of the three samples from different positions are shown in Figure 2e. For the top and bottom layers, the melting traces exhibit the same three endothermic melting peaks. The endothermic

peak at low temperature should be associated with the melting of the β -form. The middle endothermic peak approximately located at 165°C is characteristic for the melting of the original α -form. While the last endothermic peak approximately located at 169°C is characteristic for the melting of more perfect α -form deriving from β -to- α re-crystallization [22–24, 34, 35]. Quantitative estimations of relative fraction of β -form (K_{β}^*) been done according to the methods mentioned in the experimental section, and the values of the samples from top layers, core area and bottom layers are 68.2, 0 and 70.4% respectively. In addition, the amount of β -phase in sample NA0.025 is 12.3%.

Combined with the results of SEM and DSC, it can be concluded that the layered structures were well preserved during the compression molding process.

3.2. Tensile properties

Table 1 illustrates the tensile properties of PP/POE and PP/NA composites respectively. It shows the tensile properties of N-UDPCs differ little from UDPCs. Generally, the incorporation of POE and β -nucleating agent always leads to the decrease of tensile properties and the more content of fillers, the poorer tensile performance. Unexpectedly, in the PP/POE and PP/NA systems, the either tensile strength or tensile modulus just shows slight decline. The

tensile strength and modulus of PP is higher than any components filled with POE or NA. Therefore when the tension is imposed on the anisotropic specimens, the neat PP layer acts as the main load-bearing skeleton and it compensates the strength loss brought by layers with 20 wt% POE or 0.05 wt% NA. That may explain the tensile properties do not fluctuate too much whether or not the filler is uniformly dispersed in PP matrix.

3.3. Impact strength

The final instrumented impact strength of PP/POE composites is illustrated in Figure 3a. It can be easily seen that with different POE spatial distribution through the thickness, the composites respond totally different to the impact force. POE20/2PP/POE20 and 2POE20/2PP iPOE get the highest impact strength among the all. However, when POE was uniformly dispersed in PP matrix with the content of 10 wt%, the value of impact strength is only half of that compared to the former two composites. With the same average POE content, when the breaches was notched on the PP side, the impact strength value of PP/2POE20/PP and 2POE20/2PP iPP are lower than POE10. In this circumstance, POE domains in the matrix fail to resist impact forces. By comparison, we can see that although 2POE20/2PP iPOE and 2POE20/2PP iPP have the same layered structure

Table 1. the tensile properties of the two series of composites PP/POE series and PP/NA series

	Tensile strength [MPa]	Tensile modulus [MPa]		Tensile strength [MPa]	Tensile modulus [MPa]
POE20/2PP/POE20	31.7±0.6	1025.7±120.6	NA0.05/2PP/NA0.05	30.6±1.5	894.3±75.0
2POE20/2PP	30.3±0.6	1048.8±50.2	2NA0.05/2PP	30.8±1.8	861.1±81.5
POE10	31.0±0.5	1112.5±60.4	NA0.025	33.1±0.9	829.2±52.3
PP/2POE20/PP	32.7±0.5	1091.0±148.8	PP/2NA0.05/PP	31.4±1.6	884.8±167.9

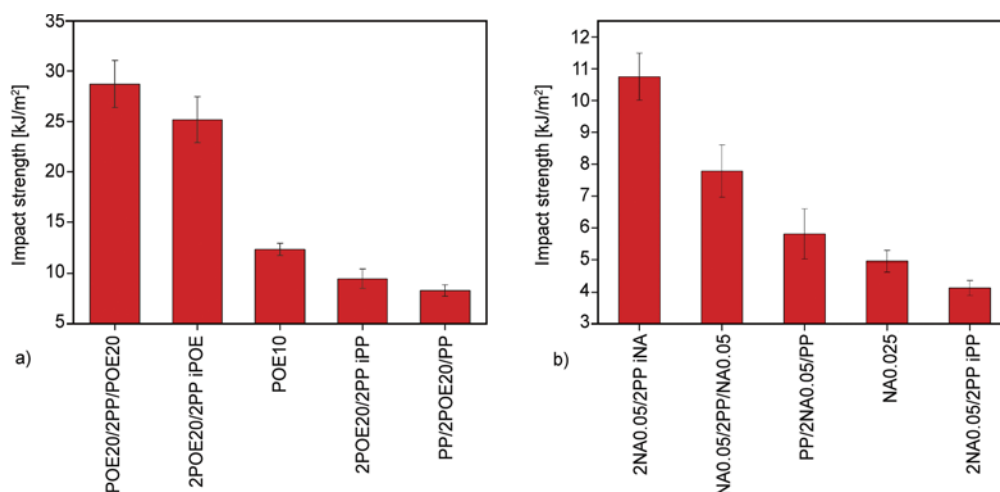


Figure 3. Impact strength of (a) PP/POE composites and (b) PP/NA composites

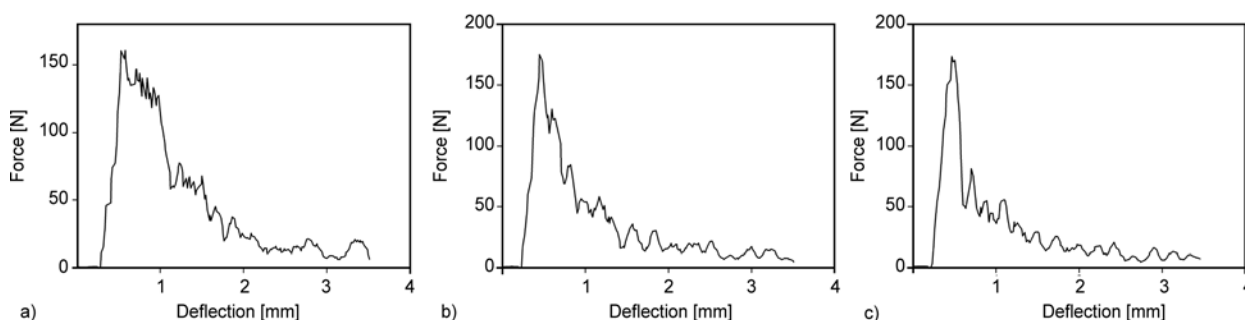


Figure 4. Force-displacement curves of (a) 2POE20/2PP, (b) POE10 and (c) PP/2POE20/PP

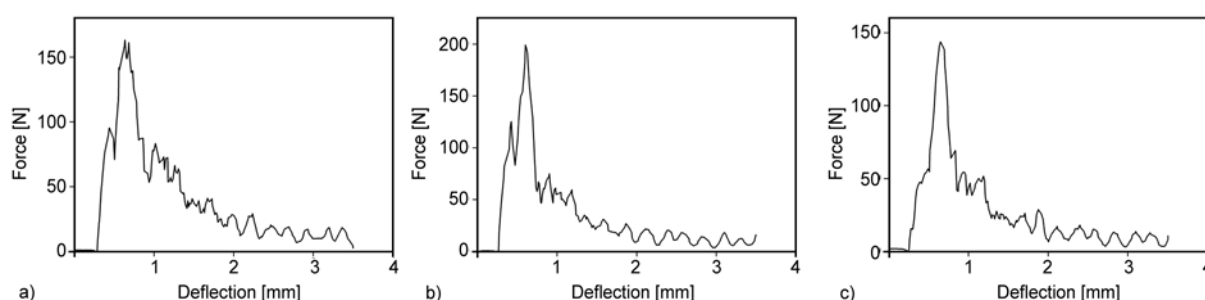


Figure 5. Force-displacement curves of (a) 2NA0.05/2PP iNA, (b) NA0.025 and (c) 2NA0.05/2PP iPP

and POE content, the impact strength is quite different due to the opposite bleach position.

Apart from the final impact strength as illustrated above, the force-displacement curve was also obtained as shown in Figure 4a, 4b and 4c, corresponding to 2POE20/2PP iPOE, POE10 and PP/2POE20/PP respectively. The traces of the three specimens show almost the same linear increase in force to the peak force (F_m) where the damage is initiated. Deformation and fracture of the matrix takes place in an area in front of the notched crack tip. It is obvious that even though the three composites have the same POE content, the force-displacement curves are totally different from each other after damage initiation. There is a sharp dropping off in force of POE10 and PP/2POE20/PP. That implies that less energy was absorbed in the damage propagation process compared with 2POE20/2PP iPOE, showing a dropping off in several stages after the specimen reaches F_m . Hence, the gradual dropping off leads to more energy absorption associated with higher impact strength.

Figure 6a compares E_t , E_i and E_p of all the five series of specimens, giving a quantitative explanation for the impacting process. As is predicated, the value of E_t has the same changing trend as that of the impact strength for different layer arrangement. However, the values of E_i don't show apparent differences among the specimens. This indicates again

that the different POE distribution doesn't significantly influence the energy absorption before the peak force is reached. It should be noted that the values of E_p are strongly influenced by the different layered structure and have the same changing trend as the impact strength does. Clearly, it is the E_p that finally affects the impact strength. For POE20/2PP/POE20 and 2POE20/2PP iPOE, the values of E_p are maintained at a higher level, whereas for POE10, 2POE20/2PP iPP and PP/2POE20/PP, the values of E_p shows dramatic dropping off. To explain the results, the different layered structure should be well considered. From the force-displacement curves, the damage initiates at a relatively short time and the forces have reached its maximum with the replacement being less than 0.1 mm. In other words, when the damage initiation ends, the crack depth is at most 0.4 mm plus the notched depth. For POE20/2PP/POE20 and 2POE20/2PP iPOE respectively have one layer with 1.8 mm thick and two layers with 3.6 mm thick of 20 wt% POE on the top. Therefore, when the damage propagation begins, the crack tip still remains in the POE20 layer which absorbs the most energy in the impact process. The specimens absorb most of the energy before 1.5 mm. It means that by purposely arranging POE layers on the notched top, they can effectively absorb the energy ($E_i + E_p$) during the impacting process. For POE10, 2POE20/2PP iPP and PP/2POE20/PP, the damage

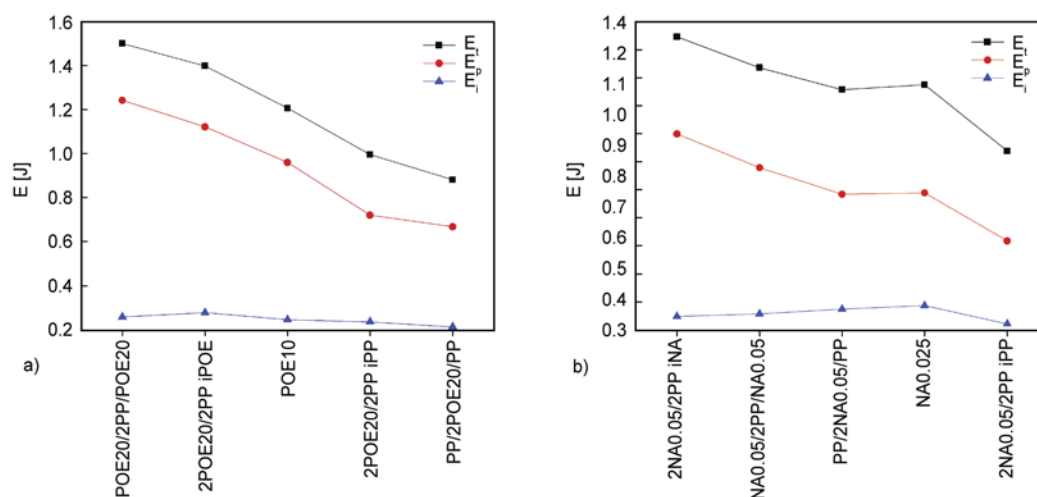


Figure 6. Illustration of E_t , E_p , E_i of (a) PP/POE composites and (b) PP/NA system

propagated in POE10 and PP layers and they show poor ability to hinder crack from propagating. According to the theory, 2POE20/PP iPOE seems to have higher impact strength than POE20/2PP/POE20, but the result is opposite. To make this clear, It is suggested that the reinforcing POE20 blend absorbs much energy by activation of multiple crazing events at a stress level below that of the crack initiation in the inner PP layer. Thereby, cracks in the PP layer can only occur when a very high degree of damage as already occurred in the outer POE20 layer. Even when cracks start to be initiated and propagate in the PP layer, the POE20 layer on the opposite side of the impact works to arrest crack propagation to rupture till too much cracks have propagated through the PP layer. It is perfectly consistent with the fact that the POE20/PP iPOE structure has lower impact resistance than the POE20/2PP/POE20 sandwich structure when impacted on the POE20 side, since no toughened layer can stop the cracks at the exit of the PP layer

The above results prove to us that the hierarchical structure of the specimens has displayed its superiority over POE uniformly dispersed ones. To verify the universality of the theory, the series of PP/NA specimens were also prepared since β -nucleating agents have the totally different toughening mechanism from elastomers. The impact process was investigated according to the same procedure.

Similarly, in the PP/NA system, different layer arrangement contributes to the variation on impact strength, seen from Figure 3b. 2NA0.05/2PP iNA shows the highest resistance to impact force, followed by NA0.05/2PP/NA0.05. Both of the two performed better than that NA was evenly dispersed in

the PP matrix at 0.025 wt%. It should be pointed out that the amount of β -phase PP in NA0.05 layer is far more than that in NA0.025 and the result seems reasonable since the amount of β -phase has the critical influence on impact strength. Like 2POE20/2PP iPP and PP/2POE20/PP, when the PP sides were notched, NA0.05/PP iPP and PP/NA0.05/PP show poor impact resistance. It seems like neither POE nor β -nucleated PP worked effectively in the four components of which cracks initiate from the PP sides.

Figure 5a, 5b and 5c illustrate the force-displacement curves of 2NA0.05/2PP iNA, NA0.025 and 2NA0.05/2PP iPP. Like the curves obtained from the PP/POE composites, the force changing trends versus displacement are nearly the same before. 2NA0.05/2PP iNA obviously decrease the slope of the force reduction after F_m so that a larger deflection and hence higher E_p can be achieved. Because PP do not show obvious toughness enhancement when the NA content is controlled at 0.025 wt%, the traces of NA0.025 and 2NA0.05/2PP iPP have the same patterns. The reason is understandable since the amount of β -nucleated PP in NA0.05 is far more than that in NA0.025 and the β -phase can absorb most of energy during the crack propagation process. The content of β -phase PP in NA0.025 is too low to be impact resistant.

E_t , E_i and E_p of all the five PP/NA specimens are also obtained from respective force-deflection curve as illustrated in Figure 6b. E_t has the same trend as the finally impact strength does. The essential factor controlling the impact performance is still the energy during crack propagation (E_i).

However in PP/NA composites, the impact strength sequence is not in accord with that of PP/POE com-

posites. For example, 2NA0.05/2PP iNA shows the best ability to resist impact force, whereas for POE reinforced PP matrix, POE20/2PP/POE20 has the highest impact strength. That may have something to do with the totally different toughening mechanism of NA and POE. PP is toughened by POE through the energy absorption of elastomer particles when impacting and the crystal form of PP change little, whereas NA can promote β -crystals instead of α -form and β -nucleated PP shows better impact resistance. The major difference is the significantly lower impact strength due to the lower energy-dissipating property of β -nucleated PP as compared to the POE/PP blends. Nevertheless, it has to be admitted that when the sides have high content of POE and β -nucleated PP where the cracks initiate, the corresponding specimens: POE20/2PP/POE20, 2POE20/2PP iPOE, NA0.05/2PP/NA0.05 and 2NA0.05/2PP iNA show higher impact strength than the specimens when the corresponding toughening agents are uniformly dispersed in PP matrix. That successfully proves that uniformly distribution of the modifiers is not always the best solution to toughen the matrix.

3.4. Fracture morphology

The impact process of composite materials is so complicated that it is unrealistic to completely figure out the toughening mechanism just through IFWIT. To help better understand the impact process, the fractured surfaces of the specimens were investigated by SEM. Figure 7a₁ shows part of the fractured surfaces of 2POE20/2PP iPOE where the cracks initiate from the 20 wt% POE layer. By careful observation, the fractured 20 wt% POE layer appears two different regions. Figure 7a₃ is near the notched tip and Figure 7a₂ is somewhat far from the notched side. Combined with the force-displacement curve, the two areas are corresponded with the damage initiation and propagation stage, respectively. At higher magnification, one can observe that in the crack initiation region Figure 7a₃, most of the POE particles are still embedded in PP matrix. As discussed above, the initiating process happens at so short a time that POE particles fail to respond to the impact force. That explains why E_1 didn't show obvious enhancement when the force reached the maximum. Contrast with the edge region, the inner area of POE20 layer shows a typical sea-island structure of elastomer enhancement system. The pulling out

of POE particles from PP matrix absorbs most of the energy during damage propagation process. The fractured surface pictures agree well with the result obtained from instrumented impact test.

The fracture surface of 2NA0.05/2PP iNA is illustrated in Figure 7b₁. The interfaces of different layers are blurred and the fracture surfaces of the damage initiation and propagation process do not differ too much. However, at higher magnification the difference can still be found even it is not so obvious. The edge area Figure 7b₃ exhibits the typical surface of brittle fracture mode. The plastic deformation zone is relative small and smooth, implying little impact energy is absorbed in that area. The inner region Figure 7b₂ corresponding to damage propagation process fracture surface shows a little more obvious plastic deformation and the extent of plastic deformation increases somewhat.

The evolution of fracture morphology from external crack tip to internal crack propagation area agrees well with the IFWIT result. It explains why the specific N-UDPCs (e.g. POE20/2PP/POE20) perform better than UDPCs (e.g. POE10) from another perspective.

4. Conclusions

In this study, PP based N-UDPCs were prepared by sheets stacking and compression moulding method. The layered structures of PP/POE and PP/NA composites were confirmed by SEM and DSC results respectively. The effect of spatially heterogeneous POE and NA content on the impact and tensile properties has been investigated. Regardless of the layer arrangement, tensile strength of anisotropic composites do not decline compared with the filler uniformly distributed ones. Although having the same filler content, composites with different modifiers distribution showed peculiar impact properties. When the crack initiate from the high filler content side, like 2POE20/2PP iPP, POE20/2PP/POE20, 2NA0.05/2PP iNA and NA0.05/2PP/NA0.05, the impact strength is obviously higher than that of the filler uniformly distributed ones. Regardless of the different toughening mechanisms of POE and β -nucleating agent, the instrumented impact test has the similar result. The essential factor controlling the final strength is the absorbed energy during damage propagation process. In addition the morphology result confirms the results from another point of view. In a word, the enhancement of impact strength was

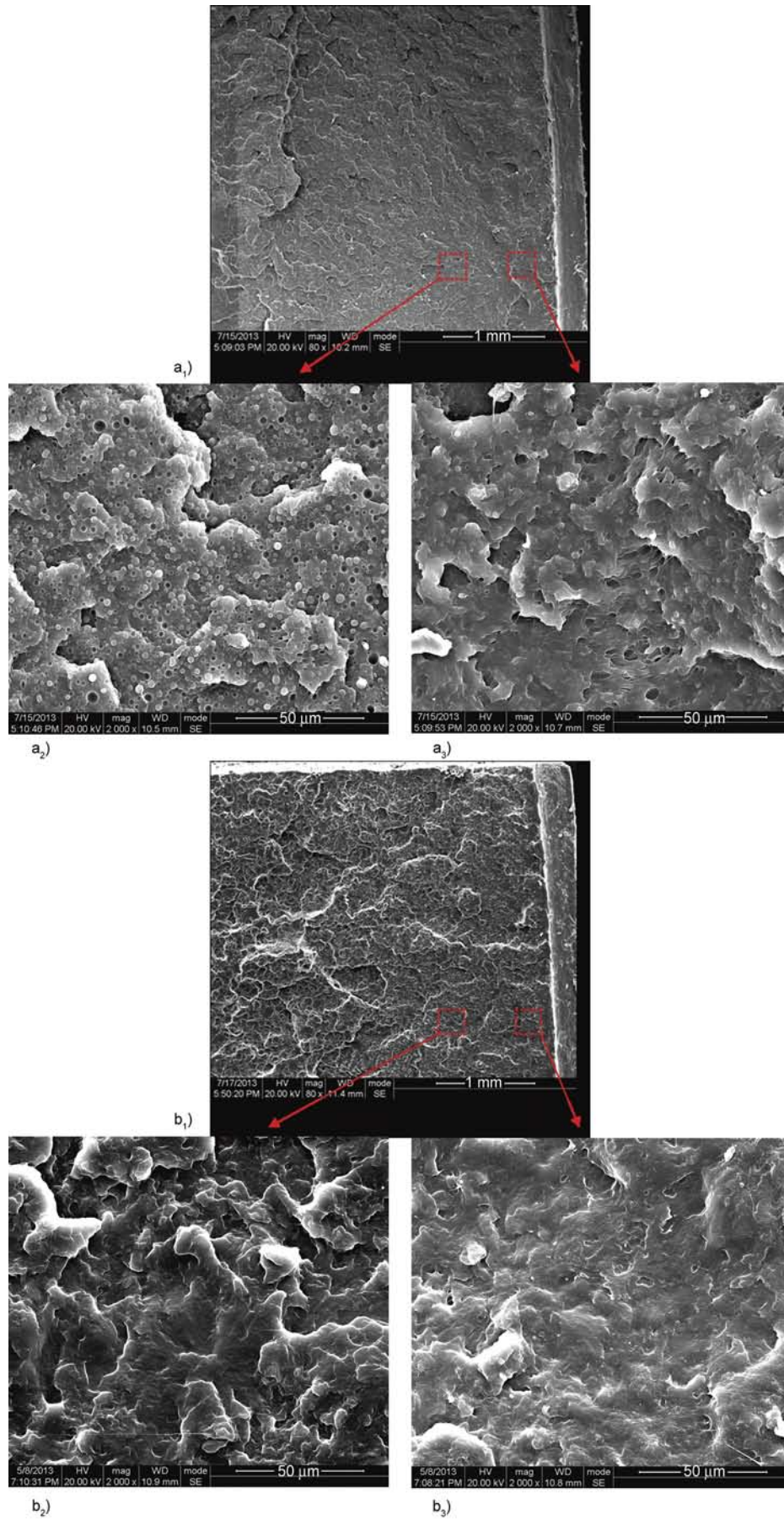


Figure 7. Typical impact-fractured surfaces morphologies of (a₁) 2POE20/2PP and (b₁) 2NA0.05/2PP iNA; (a₂), (a₃) enlarged view of sub-region marked in (a₁); (b₂), (b₃) enlarged view of sub-region marked in (b₁)

achieved by the heterogeneous distribution of toughening agents while the tensile strength kept constant. Although the method to prepare the composites looks like somewhat cumbersome, it really proves that uniformly distribution is not always the best way to achieve the high performance of polymeric composites. That may give researchers some hints to creatively manipulate the composite structures.

Acknowledgements

This work was supported by the National Natural Science Foundation of China (51121001 and 51210005) and the Special Funds for Major State Basic Research Projects of China (2011CB606006).

References

- [1] Zhang N., Li M., Nie J., Sun F.: Microstructure and surface property of macroscopic gradient polymer initiated by polysiloxane benzophenone photoinitiators with different silicone chain lengths. *Journal of Materials Chemistry*, **22**, 9166–9172 (2012).
DOI: [10.1039/C2JM30270E](https://doi.org/10.1039/C2JM30270E)
- [2] Koide S., Yazawa K., Asakawa N., Inoue Y.: Fabrication of functionally graded bulk materials of organic polymer blends by uniaxial thermal gradient. *Journal of Materials Chemistry*, **17**, 582–590 (2007).
DOI: [10.1039/B614001G](https://doi.org/10.1039/B614001G)
- [3] Ahankari S., Kar K. K.: Mechanical properties of functionally graded carbon black–styrene butadiene rubber composites: Effect of modifying gradation and average filler loading. *Journal of Applied Polymer Science*, **125**, 3469–3476 (2012).
DOI: [10.1002/app.36704](https://doi.org/10.1002/app.36704)
- [4] Misra N., Kapusetti G., Pattanayak D. K., Kumar A.: Fabrication and characterization of epoxy/silica functionally graded composite material. *Indian Journal of Physics*, **85**, 1393–1404 (2011).
DOI: [10.1007/s12648-011-0161-0](https://doi.org/10.1007/s12648-011-0161-0)
- [5] Bafekrpour E., Simon G. P., Habsuda J., Naebe M., Yang C., Fox B.: Fabrication and characterization of functionally graded synthetic graphite/phenolic nanocomposites. *Materials Science and Engineering: A*, **545**, 123–131 (2012).
DOI: [10.1016/j.msea.2012.02.097](https://doi.org/10.1016/j.msea.2012.02.097)
- [6] Lee N.-J., Jang J.: The effect of fibre-content gradient on the mechanical properties of glass-fibre-mat/polypropylene composites. *Composites Science and Technology*, **60**, 209–217 (2000).
DOI: [10.1016/S0266-3538\(99\)00122-0](https://doi.org/10.1016/S0266-3538(99)00122-0)
- [7] Wang Y.-Q., Wang Y., Zhang H.-F., Zhang L.-Q.: A novel approach to prepare a gradient polymer with a wide damping temperature range by *in-situ* chemical modification of rubber during vulcanization. *Macromolecular Rapid Communications*, **27**, 1162–1167 (2006).
DOI: [10.1002/marc.200600106](https://doi.org/10.1002/marc.200600106)
- [8] Geng C., Su J., Han S., Wang K., Fu Q.: Hierarchical structure and unique impact behavior of polypropylene/ethylene-octene copolymer blends as obtained via dynamic packing injection molding. *Polymer*, **54**, 3392–3401 (2013).
DOI: [10.1016/j.polymer.2013.04.048](https://doi.org/10.1016/j.polymer.2013.04.048)
- [9] Yang J., Zhang Y., Zhang Y.: Brittle–ductile transition of PP/POE blends in both impact and high speed tensile tests. *Polymer*, **44**, 5047–5052 (2003).
DOI: [10.1016/S0032-3861\(03\)00438-5](https://doi.org/10.1016/S0032-3861(03)00438-5)
- [10] Chen X., Yu J., Luo Z., Guo S., He M., Zhou Z.: Study on mechanical properties and phase morphology of polypropylene/polyolefin elastomer/magnesium hydroxide ternary composites. *Polymers for Advanced Technologies*, **22**, 657–663 (2011).
DOI: [10.1002/pat.1561](https://doi.org/10.1002/pat.1561)
- [11] Bai S.-L., Wang G.-T., Hiver J.-M., G'Sell C.: Microstructures and mechanical properties of polypropylene/polyamide 6/polyethylene-octene elastomer blends. *Polymer*, **45**, 3063–3071 (2004).
DOI: [10.1016/j.polymer.2004.02.070](https://doi.org/10.1016/j.polymer.2004.02.070)
- [12] Li K., Huang H.-X.: Detecting impact toughness of polypropylene/poly(ethylene-co-octene) blends with various morphologies induced via chaotic and shear mixing. *Polymer Engineering and Science*, **52**, 2157–2166 (2012).
DOI: [10.1002/pen.23177](https://doi.org/10.1002/pen.23177)
- [13] Xu L., Zhong G.-J., Ji X., Li Z.-M.: Crystallization behavior and morphology of one-step reaction compatibilized microfibrillar reinforced isotactic polypropylene/poly(ethylene terephthalate) (*i*PP/PET) blends. *Chinese Journal of Polymer Science*, **29**, 540–551 (2011).
DOI: [10.1007/s10118-011-1066-2](https://doi.org/10.1007/s10118-011-1066-2)
- [14] Benavente R., Caveda S., Pérez E., Blazquez E., Peña B., van Grieken R., Suárez I.: Influence of β -nucleation on polymorphism and properties in random copolymers and terpolymers of propylene. *Polymer Engineering and Science*, **52**, 2285–2295 (2013).
DOI: [10.1002/pen.23322](https://doi.org/10.1002/pen.23322)
- [15] Luo F., Wang J., Bai H., Wang K., Deng H., Zhang Q., Chen F., Fu Q., Na B.: Synergistic toughening of polypropylene random copolymer at low temperature: β -modification and annealing. *Materials Science and Engineering: A*, **528**, 7052–7059 (2011).
DOI: [10.1016/j.msea.2011.05.030](https://doi.org/10.1016/j.msea.2011.05.030)

- [16] Obadal M., Čermák R., Baran N., Stoklasa K., Šimoník J.: Impact strength of β -nucleated polypropylene. *International Polymer Processing*, **19**, 35–39 (2004). DOI: [10.3139/217.1802](https://doi.org/10.3139/217.1802)
- [17] Kotek J., Raab M., Baldrian J., Grellmann W.: The effect of specific β -nucleation on morphology and mechanical behavior of isotactic polypropylene. *Journal of Applied Polymer Science*, **85**, 1174–1184 (2002). DOI: [10.1002/app.10701](https://doi.org/10.1002/app.10701)
- [18] Han L., Wang Y., Liu L., Xiang F.-M., Huang T., Zhou Z.-W.: Crystallization, mechanical and thermal properties of sorbitol derivatives nucleated polypropylene/calcium carbonate composites. *Chinese Journal of Polymer Science*, **28**, 457–466 (2010). DOI: [10.1007/s10118-010-9051-8](https://doi.org/10.1007/s10118-010-9051-8)
- [19] Grein C., Gahleitner M., Bernreitner K.: Mechanical and optical effects of elastomer interaction in polypropylene modification: Ethylene-propylene rubber, poly-(ethylene-co-octene) and styrene-butadiene elastomers. *Express Polymer Letters*, **6**, 688–696 (2012). DOI: [10.3144/expresspolymlett.2012.74](https://doi.org/10.3144/expresspolymlett.2012.74)
- [20] Wahit M. U., Hassan A., Mohd Ishak Z. A., Czigány T.: Ethylene-octene copolymer (POE) toughened polyamide 6/polypropylene nanocomposites: Effect of POE maleation. *Express Polymer Letters*, **3**, 309–319 (2009). DOI: [10.3144/expresspolymlett.2009.39](https://doi.org/10.3144/expresspolymlett.2009.39)
- [21] Jiao Y.-H., Wang X.-L., Wang Y.-Z., Chen L., Mu S.-M., Li F.: Relationship between microstructure and mechanical properties of ethylene-octene copolymer reinforced and toughened PP. *Journal of Macromolecular Science Part B: Physics*, **48**, 351–364 (2009). DOI: [10.1080/00222340802680001](https://doi.org/10.1080/00222340802680001)
- [22] Výchopňová J., Habrová V., Obadal M., Čermák R., Čabla R.: Crystallization of polypropylenewith a minute amount of β -nucleator. *Journal of Thermal Analysis and Calorimetry*, **86**, 687–691 (2006). DOI: [10.1007/s10973-006-7894-6](https://doi.org/10.1007/s10973-006-7894-6)
- [23] Chvátalová L., Navrátilová J., Čermák R., Raab M., Obadal M.: Joint effects of molecular structure and processing history on specific nucleation of isotactic polypropylene. *Macromolecules*, **42**, 7413–7417 (2009). DOI: [10.1021/ma9005878](https://doi.org/10.1021/ma9005878)
- [24] Varga J., Menyhárd A.: Effect of solubility and nucleating duality of *N,N'*-dicyclohexyl-2,6-naphthalenedicarboxamide on the supermolecular structure of isotactic polypropylene. *Macromolecules*, **40**, 2422–2431 (2007). DOI: [10.1021/ma062815j](https://doi.org/10.1021/ma062815j)
- [25] Zhao S., Cai Z., Xin Z.: A highly active novel β -nucleating agent for isotactic polypropylene. *Polymer*, **49**, 2745–2754 (2008). DOI: [10.1016/j.polymer.2008.04.012](https://doi.org/10.1016/j.polymer.2008.04.012)
- [26] Hanim H., Fuad M. Y. A., Zarina R., Mohd Ishak Z. A., Hassan A.: Properties and structure of polypropylene/polyethylene-octene elastomer/nano CaCO₃ composites. *Journal of Thermoplastic Composite Materials*, **21**, 123–140 (2008). DOI: [10.1177/0892705707083634](https://doi.org/10.1177/0892705707083634)
- [27] Luo F., Wang K., Ning N., Geng C., Deng H., Chen F., Fu Q., Qian Y., Zheng D.: Dependence of mechanical properties on β -form content and crystalline morphology for β -nucleated isotactic polypropylene. *Polymers for Advanced Technologies*, **22**, 2044–2054 (2011). DOI: [10.1002/pat.1718](https://doi.org/10.1002/pat.1718)
- [28] Luo F., Xu C. L., Wang K., Deng H., Chen F., Fu Q.: Exploring temperature dependence of the toughening behavior of β -nucleated impact polypropylene copolymer. *Polymer*, **53**, 1783–1790 (2012). DOI: [10.1016/j.polymer.2012.02.024](https://doi.org/10.1016/j.polymer.2012.02.024)
- [29] Tai C. M., Li R. K. Y., Ng C. N.: Impact behaviour of polypropylene/polyethylene blends. *Polymer Testing*, **19**, 143–154 (2000). DOI: [10.1016/S0142-9418\(98\)00080-4](https://doi.org/10.1016/S0142-9418(98)00080-4)
- [30] Keledi G., Sudár A., Burgstaller C., Renner K., Móczó J., Pukánszky B.: Tensile and impact properties of three-component PP/wood/elastomer composites. *Express Polymer Letters*, **6**, 224–236 (2012). DOI: [10.3144/expresspolymlett.2012.25](https://doi.org/10.3144/expresspolymlett.2012.25)
- [31] Zhao N., Rödel H., Herzberg C., Gao S.-L., Krzywinski S.: Stitched glass/PP composite. Part I: Tensile and impact properties. *Composites Part A: Applied Science and Manufacturing*, **40**, 635–643 (2009). DOI: [10.1016/j.compositesa.2009.02.019](https://doi.org/10.1016/j.compositesa.2009.02.019)
- [32] Thomason J. L.: The influence of fibre length, diameter and concentration on the impact performance of long glass-fibre reinforced polyamide 6,6. *Composites Part A: Applied Science and Manufacturing*, **40**, 114–124 (2009). DOI: [10.1016/j.compositesa.2008.10.013](https://doi.org/10.1016/j.compositesa.2008.10.013)
- [33] Li J. X., Cheung W. L.: Effect of mould temperature on the formation of α/β polypropylene blends in injection moulding. *Journal of Materials Processing Technology*, **63**, 472–475 (1997). DOI: [10.1016/S0924-0136\(96\)02667-2](https://doi.org/10.1016/S0924-0136(96)02667-2)
- [34] Varga J.: Supermolecular structure of isotactic polypropylene. *Journal of Materials Science*, **27**, 2557–2579 (1992). DOI: [10.1007/BF00540671](https://doi.org/10.1007/BF00540671)
- [35] Yuan Q., Jiang W., An L.: Study of β - α recrystallization of the polypropylene. *Colloid and Polymer Science*, **282**, 1236–1241 (2004). DOI: [10.1007/s00396-004-1063-x](https://doi.org/10.1007/s00396-004-1063-x)

Advanced anticorrosive coatings prepared from electroactive polyimide/graphene nanocomposites with synergistic effects of redox catalytic capability and gas barrier properties

K. C. Chang¹, C. H. Hsu¹, H. I Lu², W. F. Ji¹, C. H. Chang¹, W. Y. Li¹, T. L. Chuang², J. M. Yeh^{1*}, W. R. Liu³, M. H. Tsai⁴

¹Department of Chemistry, Center for Nanotechnology and Biomedical Technology at Chung-Yuan Christian University (CYCU), Chung Li, 32023 Taiwan, Taiwan

²Master Program in Nanotechnology and Center for Nanotechnology at CYCU, Chung Li, 32023 Taiwan, Taiwan

³Department of Chemical Engineering, CYCU, Chung Li, 32023 Taiwan, Taiwan

⁴Department of Chemical and Materials Engineering, National Chin-Yi University of Technology, Taichung, 41170 Taiwan, Taiwan

Received 27 September 2013; accepted in revised form 30 November 2013

Abstract. In this study, electroactive polyimide (EPI)/graphene nanocomposite (EPGN) coatings were prepared by thermal imidization and then characterized by Fourier transformation infrared (FTIR) and transmission electron microscope (TEM). The redox behavior of the as-prepared EPGN materials was identified by in situ monitoring for cyclic voltammetry (CV) studies. Demonstrating that EPGN coatings provided advanced corrosion protection of cold-rolled steel (CRS) electrodes as compared to that of neat EPI coating. The superior corrosion protection of EPGN coatings over EPI coatings on CRS electrodes could be explained by the following two reasons. First, the redox catalytic capabilities of amino-capped aniline trimer (ACAT) units existing in the EPGN may induce the formation of passive metal oxide layers on the CRS electrode, as indicated by scanning electron microscope (SEM) and electron spectroscopy for chemical analysis (ESCA) studies. Moreover, the well-dispersed carboxyl-graphene nanosheets embedded in the EPGN matrix hinder gas migration exponentially. This would explain enhanced oxygen barrier properties of EPGN, as indicated by gas permeability analysis (GPA) studies.

Keywords: nanocomposites, electroactive, polyimide, graphene, anticorrosion

1. Introduction

Polymer-based composites were reported in the 1960s as a new paradigm in material science. In the past twenty years, three major inorganic materials acting as nanofillers have been used to prepare organic-inorganic nanocomposites: (1) layered materials such as clay [1, 2], (2) tubular materials such as carbon nanotubes (CNTs) [3, 4], and (3) spherical materials such as SiO₂ particles [5, 6] as well as other synthetic materials [7, 8].

Owing to the poor compatibility between the organic matrix and the inorganic nanofillers, it is typically desired to ameliorate the compatibility at the matrix/filler interface, ideally during the preparation of the nanocomposite materials. Thus, it is of great importance to innovative new nanofiller materials or new methods for the preparation of polymer/nanofiller composites is key in developing novel advanced polymer-based composites.

*Corresponding author, e-mail: juiming@cycu.edu.tw
© BME-PT

Polyimides (PIs) are well-known high-performance polymeric materials due to desirable tensile properties; high-temperature durability, excellent chemical and thermal stabilities, low thermal expansion coefficient, and low dielectric constant [9–12].

The electroactive oligoaniline were exploited to provide various polymers such as PIs and other derived polymers [13, 14] with electroactive properties. The incorporation of a well-defined oligoaniline into the backbone structure of a PI could render a novel electroactive PI possess electroactivity, much better mechanical properties, and thermal stability. Recently, we have reported the synthesis of an EPI with oligoaniline in the main chain via a thermal imidization reaction and further introduced nanomaterials (*e.g.*, clay nanosheets and TiO₂ nanoparticles) into the EPI to prepare EPI nanocomposites [15, 16]. All the examined materials exhibited significant enhancement of the corrosion protection of the metallic substrate as compared with that of neat electroactive polymer coatings [17, 18] since the well-dispersed nanoclay in the EPI with an aspect ratio of ~200 increasing the length of the diffusion pathways for reactive gases (*e.g.*, oxygen and water vapor) in the polymers [15].

Extensive efforts are devoted to utilizing graphene-based materials such as graphene nanoplatelets (GNPs), graphene nanosheets (GNSs), and graphene oxide (GO) as nanofillers to improve the mechanical, thermal and dielectric properties, and electricity of diverse organic polymers [19–26] since scientists discovered excellent intrinsic properties of graphene sheets. Nowadays, scientific studies associated with the lower density and higher aspect ratio (~500) [27] of conductive graphene, compared with that of non-conductive clay platelets initiated investigation into their potential application as advanced gas barrier and corrosion-prevention polymer nanocomposites. To the best of our knowledge, there is no report in investigating the anticorrosive abilities of the EPI nanocomposites with the addition of graphene nanosheets. In this study, we fabricated anticorrosive EPI/graphene nanocomposite (EPGN) coatings which could provide two-fold protection against metal corrosion. In the first step of the protection mechanism, the electroactive amino-capped aniline trimer (ACAT) components in EPI form a passivation oxide layer on the metal surface. Secondly, the well-dispersed carboxyl-graphene nanosheets in the EPI

matrix increase the tortuosity of the diffusion pathway of O₂ molecules. The detailed anticorrosion performance of the EPGN coated onto cold-rolled steel (CRS) was evaluated through a series of electrochemical corrosion measurements in a corrosive medium (3.5 wt% sodium chloride aqueous solution).

2. Experimental section

2.1. Chemicals and instruments

Aniline (Fluka, Germany) was distilled prior to use. 1,4-phenylenediamine (Aldrich, Germany), 4'-(4,4'-isopropylidene-diphenoxy)bis(phthalic anhydride) (BSAA, Aldrich, Germany), 4,4'-oxydianiline (ODA, Aldrich, Germany), and *N,N*-dimethylacetamide (DMAc, Riedel-deHaën, Germany) were used as received without further purification. Graphene nanosheets (SFG44-GNS) were prepared from SFG44 synthetic graphite powder (TIMCAL[®]). All reagents were reagent grade unless otherwise stated.

Fourier transform infrared (FTIR) spectra were recorded using a FTIR spectrometer (JASCO FT/IR-4100, Japan) operated at room temperature. The nanostructure of the composite materials was imaged with a JEOL-200FX transmission electron microscope (TEM, Japan). The samples for TEM observations were cut into 60–90-nm-thick sections with a diamond knife. The morphology of the surface of the passivation metal oxide layers was observed using a scanning electron microscope (SEM, JOEL JSM-7600F, Japan). The corrosion potential and corrosion current of sample-coated cold-rolled steel (CRS) electrodes were electrochemically measured using a VoltaLab 50 potentiostat/galvanostat. Electrochemical impedance spectroscopy (EIS) measurements were recorded on an AutoLab (PGSTAT302N) potentiostat/galvanostat electrochemical analyzer. Gas permeability (O₂ permeation) experiments were performed using a GTR-31 analyzer (Yangimoto Co., Kyoto, Japan). Electron spectroscopy for chemical analysis (ESCA) was performed using a VG Scientific ESCALAB 250 system.

2.2. Synthesis and characterization of ACAT

A typical procedure was recently established by Wei *et al.* [28] for synthesizing ACAT and accordingly, the ACAT could be easily synthesized by oxidizing 1,4-phenylenediamine and 2 equiv of aniline, with ammonium persulfate as an oxidant. The ACAT

was characterized using mass spectroscopy, FTIR spectroscopy, and ^1H NMR spectroscopy, as previously been reported in the literature [29].

2.3. Synthesis and characterization of carboxyl-graphene nanosheets

GO derived from SFG44 synthetic graphite powder (TIMCAL[®]) was synthesized by a modified Hummers' method [30]. The few-layer carboxyl-graphene nanosheets were synthesized by thermal exfoliation at 1000°C.

The surface composition of the carboxyl-graphene nanosheets was examined from the analysis of X-ray photoelectron spectroscopy (XPS) spectra, as shown in Figure 1. The characteristic peak was due to the graphitic structure (mainly C=C) at a binding energy of 284.5 eV. Moreover, the intense splitting of the C 1s peak at higher binding energy suggested the presence of oxidized carbon functional groups. The curve showed three oxidized C 1s peaks centered at 286.1 eV (C–O from phenol and ether), 287.5 eV (C=O from carbonyl and quinone), and 288.7 eV (–COO from carboxyl and ester). The relative intensity of the C–O peak was much larger than those of the C=O and –COOH peaks.

The content of functionalized groups containing carbon-oxygen bonds of carboxyl-graphene nanosheets was calculated from the XPS spectra using the Equation (1) [31]:

Content of functionalized groups containing carbon-oxygen bonds =

$$\frac{\text{Area}_{\text{C-OH}} + \text{Area}_{\text{C=O}} + \text{Area}_{\text{-COO}}}{\text{Area}_{\text{total}}} \quad (1)$$

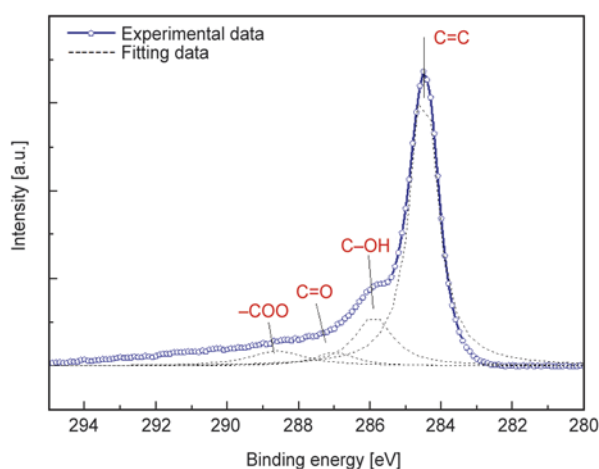


Figure 1. XPS C 1s spectra of carboxyl-graphene

According to the quantitative analysis by Gaussian fitting with three peaks, the C–O, C=O and –COO contents of the carboxyl-graphene nanosheets were 11, 5, and 4%, respectively. Graphene nanosheets were also characterized using X-ray diffraction (XRD), Raman spectra, and SEM and TEM observations, under similar conditions as those previously reported [32, 33].

2.4. Preparation of EPGN coatings

A typical procedure to prepare the EPGN coatings by thermal imidization is as follows. The electroactive poly(amic acid)/graphene (EPAAG) was prepared by reacting with BSAA and ACAT. BSAA (0.520 g, 1 mmol) and the ACAT (0.288 g, 1 mmol) were separately dissolved in 4.0 g of DMAc. Subsequently, graphene (*e.g.* 1 wt%) was mixed well with the BSAA solution, and then, the BSAA/graphene and ACAT solutions were mixed under magnetic stirring for 30 min at room temperature to form EPAAG. Then, EPAAG drops were spread on the CRS, and subsequent thermal imidization was performed at 80°C for 0.5 h, 100°C for 6 h, 160°C for 2 h, 200°C for 2 h, and 30°C for 6 h to obtain EPGN coatings. The thickness of coatings is about 30 μm

2.5. Electrochemical corrosion studies

The electrochemical corrosion measurements were performed using a VoltaLab 50 system. All the electrochemical corrosion measurements were performed using a double-wall jacketed cell covered with a glass plate, through which water was maintained at a constant temperature of $25 \pm 0.5^\circ\text{C}$. The open-circuit potential (OCP) at the equilibrium state of the system was recorded as the corrosion potential (E_{corr} in mV versus a saturated calomel electrode (SCE)). Tafel plots were obtained by scanning the potential from -500 to 500 mV above E_{corr} at a scan rate of 10 mV/min. The corrosion current (I_{corr}) was determined by superimposing a straight line along the linear portion of the cathodic or anodic curve and extrapolating it through E_{corr} . The corrosion rate (R_{corr} , in milli-inches per year, MPY) was calculated from the Equation (2):

$$R_{\text{corr}}[\text{MPY}] = \frac{0.13 I_{\text{corr}} \cdot E.W.}{A \cdot d} \quad (2)$$

where $E.W.$ is the equivalent weight [g/eq.], A is the area [cm^2], and d is the density [g/cm^3].

An AutoLab (PGSTAT302N) potentiostat/galvanostat was used to perform the alternating current (AC) impedance spectroscopy measurements. Impedance was measured in the range 100 kHz to 100 MHz with a 1 cm×1 cm pure iron working electrode embedded in epoxy, Pt as a counter electrode, and an SCE as a reference electrode. The working electrode was initially placed in the test environment for 30 min prior to the impedance run. All experiments were conducted at room temperature. All trials were repeated at least three times to ensure reproducibility and statistical significance of the raw data.

2.6. Preparation of membranes and molecular barrier property measurements

The typical procedure for the preparation of EPGN membranes with 0.5 and 1 wt% of carboxyl-graphene nanosheets (denoted as EPGN0.5 and EPGN1, respectively) is shown in Figure 2. Membranes of the as-prepared EPI and EPGN materials were prepared for measurement of the oxygen barrier property that had been reported in our earlier papers [34, 35].

3. Results and discussion

3.1. Characterization of EPI and EPGN materials

The successful synthesis of EPI and EPGN materials was confirmed by IR analysis. Figure 3 shows

the FTIR spectra of the obtained for ACAT-based EPAA, EPI, and EPGN materials. In all of the FTIR spectra, the characteristic peaks from 2500 to 3500 cm^{-1} indicate the presence of O–H and N–H. Moreover, the characteristic peaks at 1600 and 1504 cm^{-1} were assigned to the stretching modes of N=Q=N and N–B–N, respectively (Q represents the quinoid ring, and B represents the benzene ring structure). In the case of ACAT-based EPAA (Figure 3 curve a), the characteristic peaks for C=O in COOH were found at 1712 cm^{-1} . The EPI characteristic peaks in both EPI and EPGN1, that is, the peaks related to the functional groups of EPAA such as carboxylic acid and amine groups at 2500–3500 cm^{-1} , were absent. The two peaks at 1774 and 1712 cm^{-1} may be associated with the asymmetric and symmetric carbonyl stretching vibration, respectively, of the imide absorption band, respectively.

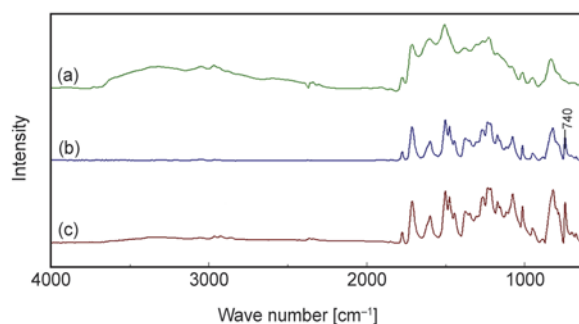


Figure 3. FTIR spectra of (a) EPAA, (b) EPI, and (c) EPGN

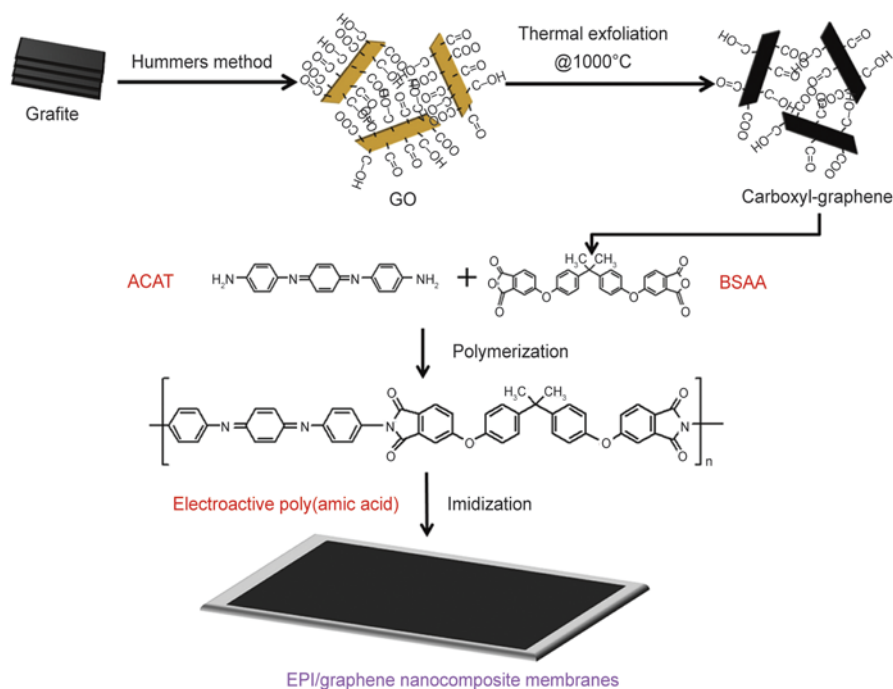


Figure 2. Preparation of EPI/graphene nanocomposite (EPGN) membranes

Finally, the new peaks at 1373 and 740 cm^{-1} can be explained by C–N stretching and imide ring, respectively. The characteristic absorption band found at 740 cm^{-1} was the result of the deformation of the imide groups, as shown in Figure 3 curves b and c. These changes in the characteristic peaks of ACAT-based EPAA, EPI, and EPGN indicate that EPAA was almost completely converted into the corresponding ACAT-based EPI and EPGN through the thermal imidization process at 200°C [18, 36, 37]. Moreover, comparison of the two curves of the EPI and EPGN materials, no obviously different absorption peak is observed, probably because of the low amounts of graphene present in the samples [38].

3.2. Morphology of EPGN membranes

The morphological studies of the dispersion of graphene nanosheets can be identified by TEM observations. Figure 4 shows the micrographs of EPGN1 taken at 200 k magnification using the 120 kV TEM instrument. The bright regions of the photograph at

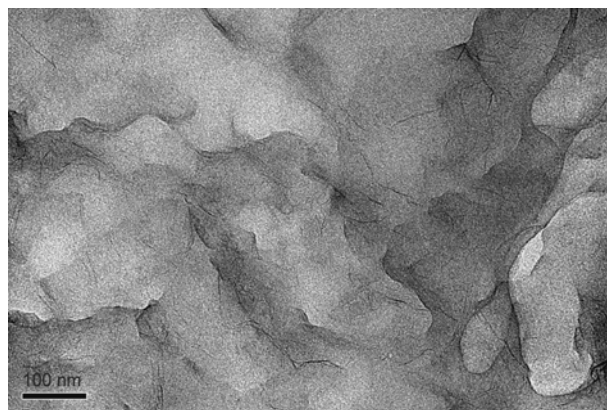


Figure 4. TEM micrographs of EPGN1 ($\times 200\text{ k}$)

high magnification represent the domain of the EPI matrix, and the dark lines correspond to the cross section of the layers of graphene nanosheets. As shown in the figure, EPGN1 exhibited relatively well-dispersed graphene nanosheets in the EPI matrix. This indicates that the attachment of carboxylic groups onto the graphene surface could effectively enhance the compatibility between the car-

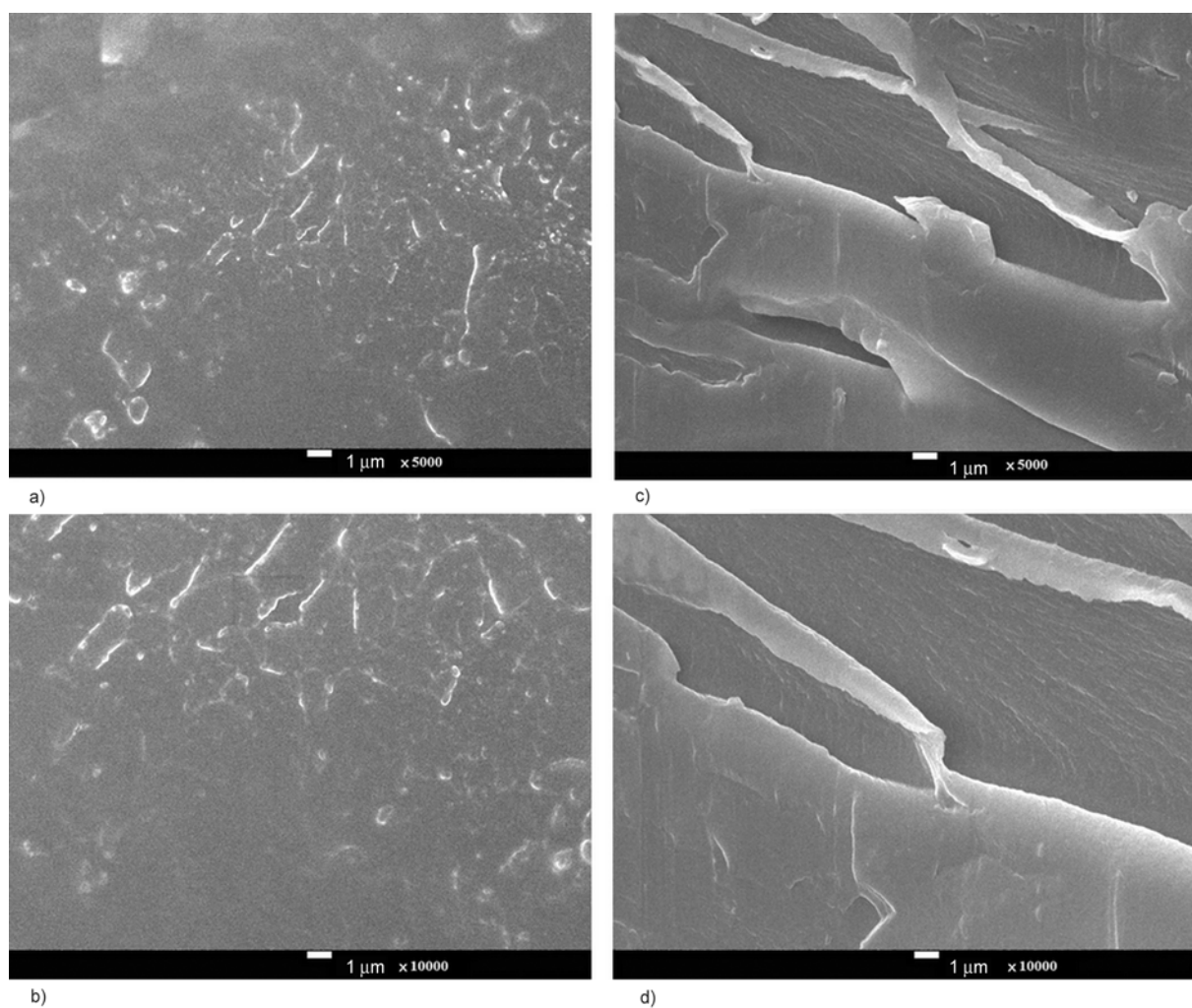


Figure 5. SEM images of fracture surfaces of (a) EPI ($\times 5\text{ k}$), (b) EPI ($\times 10\text{ k}$), (c) EPGN1 ($\times 5\text{ k}$), and (d) EPGN1 ($\times 10\text{ k}$)

boxyl-graphene nanosheets and the EPI matrix, leading to improved dispersion capability. The enhanced dispersion can also be attributed to the formation of hydrogen bonds between the remaining hydroxyl groups of the carboxyl-graphene nanosheets and the carboxyl groups of EPAA [39].

The dispersion of graphene nanosheets in the EPI matrix are also shown in the SEM images of the fracture surfaces of membranes in Figure 5. As can be seen in Figure 5a, 5b, EPI film shows a smooth fractured surface. In contrast, the EPGN1 membrane possesses rough fractured surfaces that could be attributed to the strong interfacial adhesion and good compatibility between the EPI matrix and carboxyl-graphene nanosheets (Figure 5c, 5d).

3.3. Adhesion test

Void space at the coating-metal interface is responsible for the accumulation of water and ions at the interface, and believed to be a primary failure mechanism for corrosion resistant coatings. Therefore, a corrosion-inhibiting coating should have good adhesion with the protecting surface for its practical application. The adhesion of the EPI and EPGN1 coating on the CRS substrate was evaluated according to the cross-cut method [40]. The results showed that there was no significant peeling of either EPI or EPGN1 after cross-cutting through the coating (Figure 6), indicating that the coatings developed in this study strongly stuck on the CRS surface (good adhesion).

3.4. Electroactivity of EPI and EPGN coatings

Cyclic voltammetry (CV) has been widely used to characterize the electrochemical properties of electroactive polymers. In this study, the polymers were

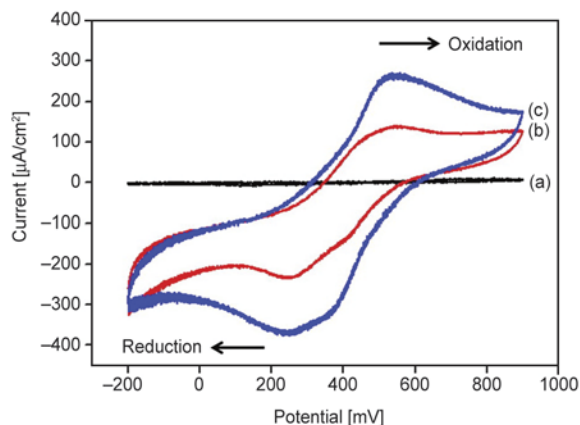


Figure 7. Redox behavior of (a) NEPI-coated, (b) EPI-coated, and (c) EPGN1-coated electrode measured in 1.0 M H_2SO_4 aqueous solution

characterized by CV using a three-electrode electrochemical cell. As shown in Figure 7, the electrochemical CV results indicate that the EPGN materials (*e.g.*, EPGN1) in the form of a coating showed a single oxidation peak, which was similar to the case of the EPI [17]. EPGN1 showed an oxidation current (I_{ox}) of $271.9 \mu\text{A}/\text{cm}^2$ and a reduction current (I_{red}) of $376.6 \mu\text{A}/\text{cm}^2$; the latter was smaller than that of the EPI ($I_{\text{ox}} = 141.3 \mu\text{A}/\text{cm}^2$, $I_{\text{red}} = 236.8 \mu\text{A}/\text{cm}^2$). However, NEPI showed null zero redox current. This implies that the incorporation of the ACAT into the polyimide introduces electroactivity in the as-prepared polyimide. The introduction of graphene into the EPI matrix results in EPGN materials with higher electroactivity than that of the EPI.

We therefore infer that coatings produced from EPGN materials may provide enhanced corrosion protection as a result of synergistic effects of creating a passive metal oxide layer and the barrier properties that the graphene nanosheets provide to hinder oxygen migration. A series of electrochemical

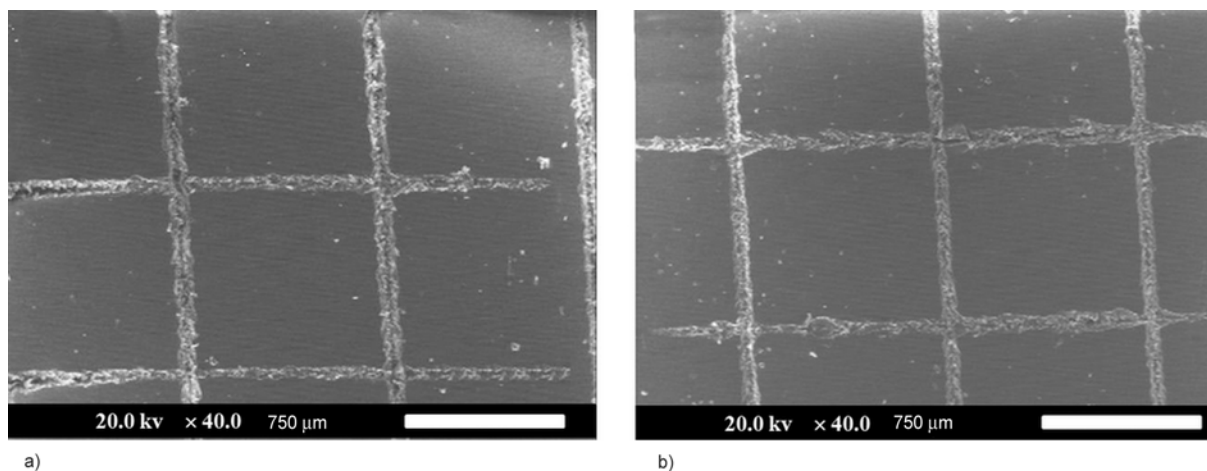


Figure 6. SEM images of (a) EPI-coated on CRS and (b) EPGN1-coated on CRS after testing for adhesion

standard corrosion measurements (e.g., potentiodynamic and electrochemical impedance measurements) and gas barrier measurements are discussed in the following sections as evidence.

3.5. Potentiodynamic measurements

The polarization curves for EPI and a series of EPGN coatings on CRS coupons recorded after 30 min of immersion in a 3.5 wt% aqueous NaCl electrolyte are illustrated. Figure 8 shows the Tafel lines (a), (b), (c), and (d) for the uncoated, EPI-coated, EPGN0.5-coated, and EPGN1-coated CRS electrode, respectively, at 500 mV/min. The corrosion parameters calculated from the Tafel plots for several composite materials are summarized in Table 1; generally, a higher E_{corr} and R_p , and a lower I_{corr} and R_{corr} indicate better corrosion protection. The values of polarization resistance, R_p , were evaluated from the Tafel plots, according to the Stern-Geary equation (Equation (3)) [41]:

$$R_p = \frac{b_a b_c}{2.303(b_a + b_c)} \cdot I_{\text{corr}} \quad (3)$$

where I_{corr} is the corrosion current determined from the intersection of the linear portions of the anodic and cathodic curves, and b_a and b_c are anodic and

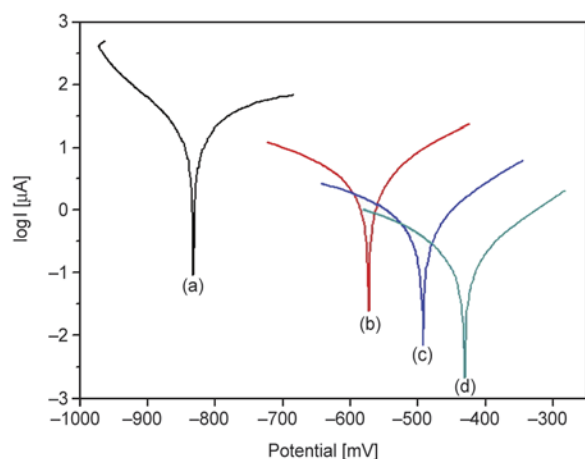


Figure 8. Tafel plots for (a) bare, (b) EPI-coated, (c) EPGN0.5-coated, and (d) EPGN1-coated CRS electrodes at 25±0.5°C

cathodic Tafel slopes ($\Delta E/\Delta \log I$), respectively. The protection efficiency (P_{EF} [%]) values were estimated using the Equation (4) [42]:

$$P_{\text{EF}} [\%] = 100 \frac{R_p^{-1}(\text{uncoated}) - R_p^{-1}(\text{coated})}{R_p^{-1}(\text{coated})} \quad (4)$$

The results in Figure 8 and Table 1 indicate that the EPI-coated CRS coupon shows a higher E_{corr} value than does the uncoated CRS, which is consistent with the results of earlier studies [15–18]. Moreover, the EPGN materials showed a higher E_{corr} , R_p , and P_{EF} and lower I_{corr} values than does the EPI. For example, the EPGN1-coated CRS has an E_{corr} of -432 mV, I_{corr} of 0.15 $\mu\text{A}/\text{cm}^2$, R_p of 165.29 $\text{k}\Omega\cdot\text{cm}^2$, R_{corr} of 0.14 MPY, and P_{EF} of 98.79%, which are over twice those of the EPI-coated electrode. On the other hand, corrosion current values of the EPGN coatings on CRS were found to decrease gradually with a further increase in graphene loading.

3.6. Electrochemical impedance measurements

Electrochemical impedance spectroscopy (EIS) is used to examine the activity difference between the CRS surface upon EPI and EPGN coating treatment. Impedance is a complex resistance when alternating current flows through a circuit made of capacitors, resistors, or insulators, or any of their combination [43]. EIS measurement results in currents over a wide range of frequencies. To obtain the Randles circuit parameters, fitting of the model to the experimental data should be performed using complex nonlinear least-squares procedures available in numerous EIS data fitting computer programs. For the simulation studies, corrosion of metals is modeled with an equivalent circuit (called a Randles circuit), as illustrated in Figure 9, which is made of a double-layer capacitor in parallel with a charge transfer resistor and connected in series with an electrolyte solution resistor. The impedance (Z) depends

Table 1. Electrochemical corrosion measurements of bare CRS, EPI, EPGN0.5 and EPGN1 coated electrodes

Sample code	Electrochemical corrosion measurements ^a				P_{EF} [%]	Thickness [μm]
	E_{corr} [mV vs SCE]	R_p [$\text{k}\Omega\cdot\text{cm}^2$]	I_{corr} [$\mu\text{A}/\text{cm}^2$]	R_{corr} [MPY]		
CRS	-832	2.00	14.50	13.50	–	–
EPI	-573	11.10	2.75	2.56	81.98	32±2
EPGN0.5	-493	52.17	0.55	0.51	96.17	31±2
EPGN1	-432	165.29	0.15	0.14	98.79	33±2

^aSaturated calomel electrode (SCE) was employed as a reference electrode

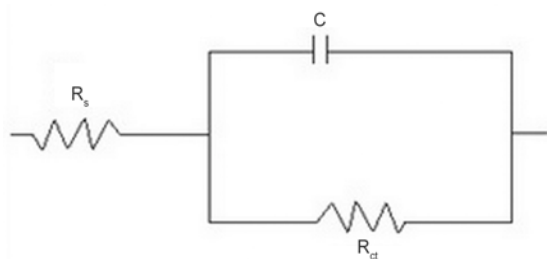


Figure 9. Randles equivalent circuit used for modeling impedance measurements (EIS)

on the charge transfer resistance (R_{ct}), solution resistance (R_s), capacitance of the electrical double layer, and frequency of the AC signal (ω) (Equation (5):

$$Z = Z' + jZ'' = R_s \frac{R_{ct}}{1 + (R_{ct}C_{dl}\omega)^2} + \frac{jR_{ct}^2C_{dl}\omega}{1 + (R_{ct}C_{dl}\omega)^2} \quad (5)$$

The fitting data fitted well to all the experimental electrochemical data. The high-frequency intercept is equal to the solution resistance, and the low-frequency intercept is equal to the sum of the solution and charge transfer resistances [44]. In general, a larger semicircle diameter (charge transfer resistance) represents a smaller corrosion rate.

Figure 10 shows the Nyquist plots of the four measured samples. The first sample (curve a) is uncoated CRS. A series of samples denoted as (curve b), (curve c), and (curve d) represent CRS-coated by EPI, EPGN0.5, and EPGN1, respectively. The corrosion test on these samples immersed in 3.5 wt% NaCl aqueous electrolyte for 30 min is followed by EIS analysis. The charge transfer resistances of all samples, as determined by subtracting the intersection of the high-frequency end from the low-frequency end of the semicircle arc with the real axis,

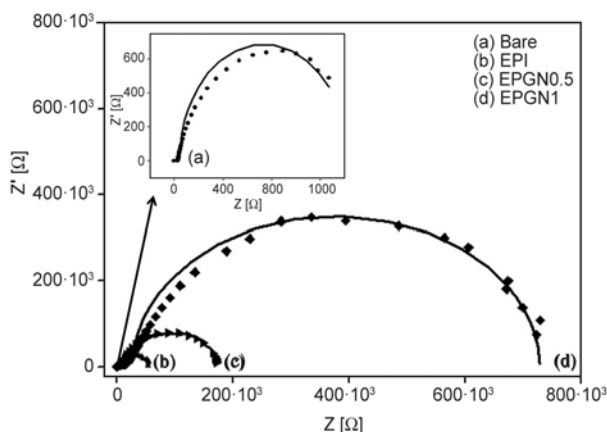


Figure 10. Nyquist plots for (a) bare, (b) EPI-coated, (c) EPGN0.5-coated, and (d) EPGN1-coated CRS electrodes

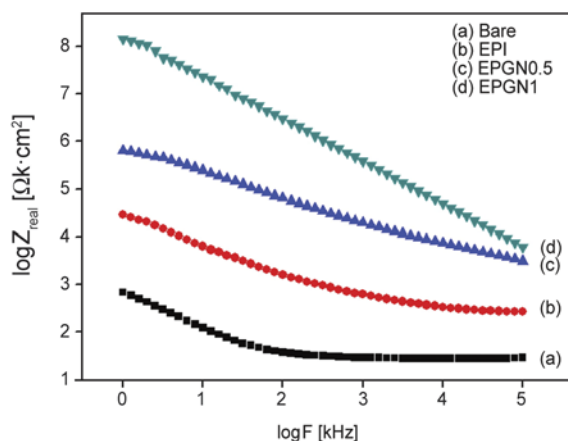


Figure 11. Bode plots for (a) bare, (b) EPI-coated, (c) EPGN0.5-coated, and (d) EPGN1-coated CRS electrodes

are 1.27, 54.69, 170, and 728 $k\Omega \cdot cm^2$, respectively. EIS Bode plots (impedance vs. frequency) of all samples are shown in Figure 11. Z_{real} is a measure of corrosion resistance [45]. Low Z_{real} value could be brought about by very high capacitance and/or very low resistance of the coating [46]. Large value of the capacitance has been related to the high extent at which water has penetrated the coating [47]. In the case of Bode plots, the value of Z_{real} at the lowest frequency also represents the corrosion resistance. The Bode magnitude plots for uncoated CRS and CRS-coated by EPI, EPGN0.5, and EPGN1 shows Z_{real} values of 2.8, 4.5, 5.8, and 8.1 $k\Omega \cdot cm^2$, respectively, at low frequency end. These results clearly demonstrate that the EPGN1 coating protects the CRS electrode against corrosion better than the EPI and EPGN0.5 coatings.

The increase in the impedance values at high graphene concentrations in various frequency regions could be interpreted as the barrier effect of the graphene nanosheets dispersed in the composites. Visual observation of the corrosion products clearly reveal that the EPGN samples exhibiting corrosion protection have a grayish oxide layer over the bare exposed CRS surface, similar to what was observed by Wessling [48, 49], in the case of PANI dispersion coatings on steel. The barrier effect of the EPGN materials as compared to that of the EPI may be due to the dispersed graphene in the EPI matrix, which increased the tortuosity of the diffusion pathway of O_2 molecules [39, 50], as shown in Figure 12. They are further evidenced by the observations on the CRS surface and gas permeability studies of coat-

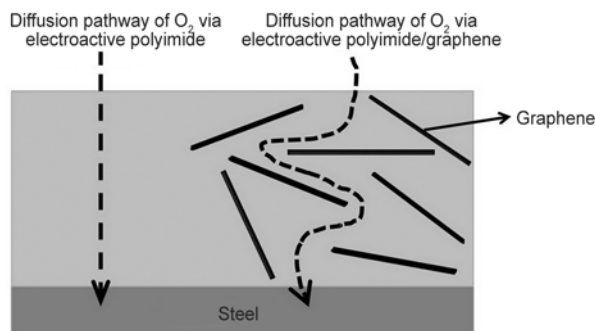


Figure 12. Schematic representation of O_2 molecules following a tortuous path through an EPI and EPGN materials

ings and membranes, as discussed in Sections 3.6 and 3.7.

3.7. Observations of the CRS surface

The EPI and EPGN coatings might induce the formation of a layer of passivation oxide, Fe_2O_3/Fe_3O_4 , through the redox reaction between the quinonediimine segment (Figure 6) of EPI/EPGN and the metal surface. It should be emphasized that the advantage of this newly developed EPGN materials is that it not only provides passive protection but also acts as an active functional polymer materials that can induce the formation of another inert protection layer, *i.e.*, Fe_2O_3 and Fe_3O_4 .

Next, the as-prepared sample coatings were stored for 24 h at room temperature and then removed using a razor knife. Visual observation of the passivation oxide layers revealed a grayish oxide layer over the CRS surface under the EPGN1 coating on CRS. It is similar to what was observed by Wessling [48, 51]. The SEM images revealed that the oxide layers were formed between the EPGN1 coating and

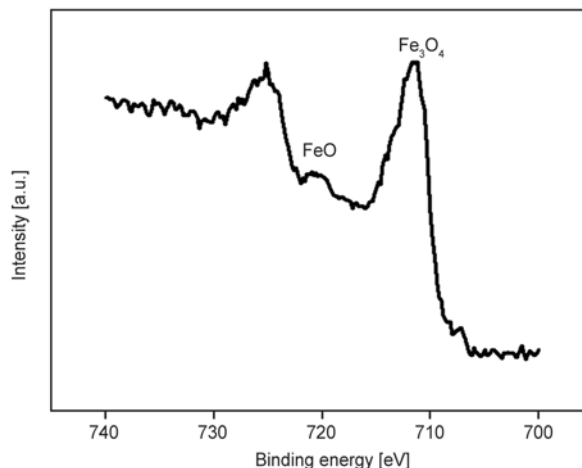


Figure 14. ESCA Fe 2p core-level spectra of EPI

the CRS surface (Figure 13b), but we could not observe the same image from the pure CRS surface (Figure 13a).

In addition to the SEM observations, the chemical nature of the passivation oxide layers was determined by ESCA. The plots of binding energy vs. intensity for the iron oxide layers are shown in Figure 14. The passivation oxide layers exhibited the Fe $2p^{3/2}$ peak binding energy of Fe_2O_3 at 710.9 eV; FeO at 709.6 eV; and Fe_3O_4 at 710.3 eV. The Fe 2p spectra of FeO and Fe_3O_4 were, and hence, it was difficult to distinguish between the two oxides. The $2p^{3/2}$ binding energy was about 725.2 and 711.6 eV. These findings indicated that the passive oxide layer is predominately composed by Fe_2O_3 above a very thin Fe_3O_4 layer, which was consistent with the results of previous studies [48, 51–53].

The enhanced corrosion protection of EPI and EPGN coatings was found to be associated with the formation of passivation protective metal oxide lay-

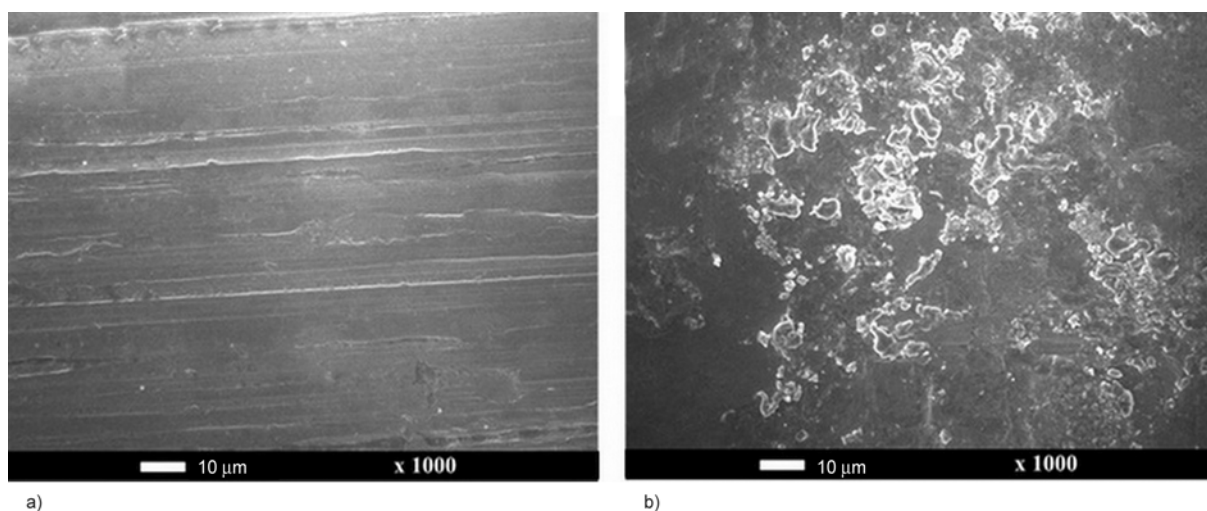


Figure 13. SEM images for (a) polished CRS metal and the surface of the (b) EPGN1 coating on the CRS metal

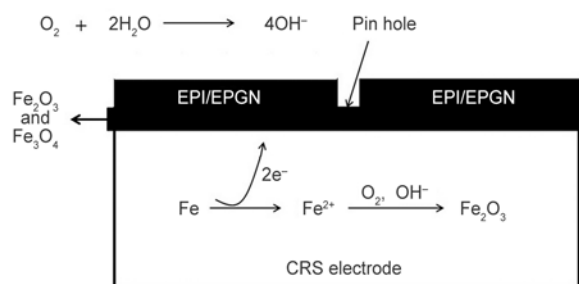


Figure 15. Schematic diagram of mechanism of CRS passivation by EPI/EPGN coatings

ers, induced by the redox catalytic properties of as-prepared EPI and EPGN coatings, as shown in Figure 15.

3.8. Gas barrier of EPI and EPGN membranes

The presence of filler, inorganic or organic, in the polymer matrix usually constitutes a solid barrier in the path of the gas molecules passing through the polymer. A more tortuous path is thus forced upon the gas molecules passing through the polymeric matrix, retarding the progress of the phenomenon. The more tortuous the path the longer it takes for the gas molecules to pass through the material, resulting in a macroscopically observed reduced permeability. The higher the filler–matrix interfacial area and aspect ratio of the filler, the more tortuous the path, hence the greater the decrease in permeability. Graphene-based polymer nanocomposites had been examined intensively for their gas barrier rate's enhancements, due to the high aspect ratio of well-dispersed graphene nanosheets [54]. In this study, molecular barrier measurements were performed on membranes of EPI and EPGN materials prepared to

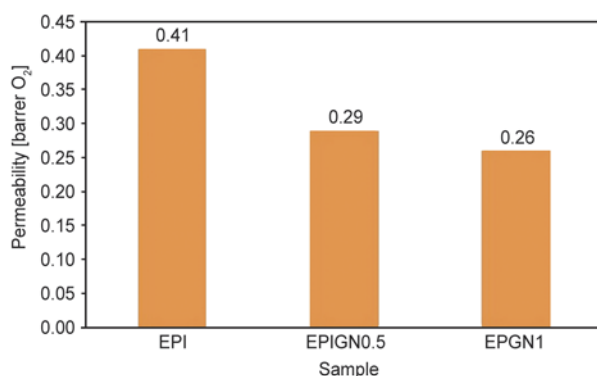


Figure 16. Permeability of oxygen as a function of graphene content in the EPGN materials

a film thickness of ~50 μm. Compared to EPI, EPGN membranes at low graphene loading (e.g., 0.5 wt%) shows about 29% reduction in O₂ permeability, as shown in Figure 16. The decrease in gas permeability is attributed to the barrier properties of the layers of graphene nanosheets dispersed in the composites. It should be noted that a further increase in graphene loading in the EPGN materials up to 1 wt% results in a further decrease in gas permeability.

4. Conclusions

Electroactive polyimide/graphene nanocomposite (EPGN) materials were successfully prepared by thermal imidization. The structure and electroactivity of the EPGN materials were investigated by FTIR and CV. The dispersion capability of the carboxyl-graphene nanosheets in the EPI matrix was observed by TEM studies. The nanocomposites consisting of the EPI matrix and well-dispersed graphene nanosheets were found to exhibit excellent anticorrosive properties resulted from enhanced gas barrier properties.

Acknowledgements

The authors acknowledge the financial support from the Ministry of Education, Taiwan, R.O.C. (NSC 101-2113-M-033-005-MY1, 101-3113-P-002-026 and 102-2622-E-007-016-CC1); The Center-of-Excellence (COE) Program on Membrane Technology from the Ministry of Education (MOE), R.O.C.; The Department of Chemistry at CYCU (CYCU-01RD-RA002-11235); and The Center for Nanotechnology and Biomedical Technology at CYCU.

References

- [1] Lee C-H., Kato M., Usuki A.: Preparation and properties of bio-based polycarbonate/clay nanocomposites. *Journal of Materials Chemistry*, **21**, 6844–6847 (2011). DOI: [10.1039/C1JM10087D](https://doi.org/10.1039/C1JM10087D)
- [2] Usuki A., Hasegawa N., Kato M., Kobayashi S.: Polymer-clay nanocomposites. *Advances in Polymer Science*, **179**, 135–195 (2005). DOI: [10.1007/b104481](https://doi.org/10.1007/b104481)
- [3] Pötschke P., Krause B., Buschhorn S. T., Köpke U., Müller M. T., Villmow T., Schulte K.: Improvement of carbon nanotube dispersion in thermoplastic composites using a three roll mill at elevated temperatures. *Composites Science and Technology*, **74**, 78–84 (2013). DOI: [10.1016/j.compscitech.2012.10.010](https://doi.org/10.1016/j.compscitech.2012.10.010)
- [4] Minus M. L., Chae H. G., Kumar S.: Polyethylene crystallization nucleated by carbon nanotubes under shear. *ACS Applied Materials Interfaces*, **4**, 326–330 (2012). DOI: [10.1021/am2013757](https://doi.org/10.1021/am2013757)

- [5] Hu X-L., Hou G-M., Zhang M-Q., Rong M-Z., Ruan W-H., Giannelis E-P.: A new nanocomposite polymer electrolyte based on poly(vinyl alcohol) incorporating hypergrafted nano-silica. *Journal of Materials Chemistry*, **22**, 18961–18967 (2012).
DOI: [10.1039/C2JM33156J](https://doi.org/10.1039/C2JM33156J)
- [6] Chen J. H., Rong M. Z., Ruan W. H., Zhang M. Q.: Interfacial enhancement of nano-SiO₂/polypropylene composites. *Composites Science and Technology*, **69**, 252–259 (2009).
DOI: [10.1016/j.compscitech.2008.10.013](https://doi.org/10.1016/j.compscitech.2008.10.013)
- [7] Hojjati B., Charpentier P. A.: Synthesis of TiO₂-polymer nanocomposite in supercritical CO₂ via RAFT polymerization. *Polymer*, **51**, 5345–5351 (2010).
DOI: [10.1016/j.polymer.2010.09.050](https://doi.org/10.1016/j.polymer.2010.09.050)
- [8] Tang C-W., Li B., Sun L., Lively B., Zhong W-H.: The effects of nanofillers, stretching and recrystallization on microstructure, phase transformation and dielectric properties in PVDF nanocomposites. *European Polymer Journal*, **48**, 1062–1072 (2012).
DOI: [10.1016/j.eurpolymj.2012.04.002](https://doi.org/10.1016/j.eurpolymj.2012.04.002)
- [9] Yang C-P., Su Y-Y., Guo W., Hsiao S-H.: Synthesis and properties of novel fluorinated polynaphthalimides derived from 1,4,5,8-naphthalenetetracarboxylic dianhydride and trifluoromethyl-substituted aromatic bis(ether amine)s. *European Polymer Journal*, **45**, 721–729 (2009).
DOI: [10.1016/j.eurpolymj.2008.12.013](https://doi.org/10.1016/j.eurpolymj.2008.12.013)
- [10] Lin S., Guo R., Lan J., Chen S., Shang J.: Synthesis and properties of novel thermoplastic poly(ester-etherimide) elastomers derived from 4,4'-bis(N-trimellitimid)-diphenylether unit with excellent thermal stability. *Journal of Macromolecular Science Part A: Pure and Applied Chemistry*, **49**, 1052–1060 (2012).
DOI: [10.1080/10601325.2012.728473](https://doi.org/10.1080/10601325.2012.728473)
- [11] Tsuchiya T., Maeda S., Tsukada Y.: Packaging substrate applications of ultra low CTE polyimide. *Journal of Photopolymer Science and Technology*, **25**, 359–364 (2012).
DOI: [10.2494/photopolymer.25.359](https://doi.org/10.2494/photopolymer.25.359)
- [12] Popovici D., Hulubei C., Cozan V., Lisa G., Bruma M.: Polyimides containing cycloaliphatic segments for low dielectric material. *High Performance Polymers*, **24**, 194–199 (2012).
DOI: [10.1177/0954008311435798](https://doi.org/10.1177/0954008311435798)
- [13] Wang Z. Y., Yang C., Gao J. P., Lin J., Meng X. S., Wei Y., Li S.: Electroactive polyimides derived from amino-terminated aniline trimer. *Macromolecules*, **31**, 2702–2704 (1998).
DOI: [10.1021/ma971782s](https://doi.org/10.1021/ma971782s)
- [14] Chao D., Cui L., Lu X., Mao H., Zhang W., Wei Y.: Electroactive polyimide with oligoaniline in the main chain via oxidative coupling polymerization. *European Polymer Journal*, **43**, 2641–2647 (2007).
DOI: [10.1016/j.eurpolymj.2007.03.048](https://doi.org/10.1016/j.eurpolymj.2007.03.048)
- [15] Huang H-Y., Huang T-C., Yeh T-C., Tsai C-Y., Lai C-L., Tsai M-H., Yeh J-M., Chou Y-C.: Advanced anti-corrosive materials prepared from amine-capped aniline trimer-based electroactive polyimide-clay nanocomposite materials with synergistic effects of redox catalytic capability and gas barrier properties. *Polymer*, **52**, 2391–2400 (2011).
DOI: [10.1016/j.polymer.2011.03.030](https://doi.org/10.1016/j.polymer.2011.03.030)
- [16] Weng C-J., Huang J-Y., Huang K-Y., Jhuo Y-S., Tsai M-H., Yeh J-M.: Advanced anticorrosive coatings prepared from electroactive polyimide-TiO₂ hybrid nanocomposite materials. *Electrochimica Acta*, **55**, 8430–8438 (2010).
DOI: [10.1016/j.electacta.2010.07.063](https://doi.org/10.1016/j.electacta.2010.07.063)
- [17] Huang K-Y., Jhuo Y-S., Wu P-S., Lin C-H., Yu Y-H., Yeh J-M.: Electrochemical studies for the electroactivity of amine-capped aniline trimer on the anticorrosion effect of as-prepared polyimide coatings. *European Polymer Journal*, **45**, 485–493 (2009).
DOI: [10.1016/j.eurpolymj.2008.10.033](https://doi.org/10.1016/j.eurpolymj.2008.10.033)
- [18] Huang T-C., Yeh T-C., Huang H-Y., Ji W-F., Chou Y-C., Hung W-I., Yeh J-M., Tsai M-H.: Electrochemical studies on aniline-pentamer-based electroactive polyimide coating: Corrosion protection and electrochromic properties. *Electrochimica Acta*, **56**, 10151–10158 (2011).
DOI: [10.1016/j.electacta.2011.08.114](https://doi.org/10.1016/j.electacta.2011.08.114)
- [19] Bao C., Song L., Wilkie C. A., Yuan B., Guo Y., Hu Y., Gong X.: Graphite oxide, graphene, and metal-loaded graphene for fire safety applications of polystyrene. *Journal of Materials Chemistry*, **22**, 16399–16406 (2012).
DOI: [10.1039/C2JM32500D](https://doi.org/10.1039/C2JM32500D)
- [20] Potts J. R., Shankar O., Du L., Ruoff R. S.: Processing-morphology-property relationships and composite theory analysis of reduced graphene oxide/natural rubber nanocomposites. *Macromolecules*, **45**, 6045–6055 (2012).
DOI: [10.1021/ma300706k](https://doi.org/10.1021/ma300706k)
- [21] Jiang X., Drzal L. T.: Exploring the potential of exfoliated graphene nanoplatelets as the conductive filler in polymeric nanocomposites for bipolar plates. *Journal of Power Sources*, **218**, 297–306 (2012).
DOI: [10.1016/j.jpowsour.2012.07.001](https://doi.org/10.1016/j.jpowsour.2012.07.001)
- [22] Li M., Huang X., Wu C., Xu H., Jiang P., Tanaka T.: Fabrication of two-dimensional hybrid sheets by decorating insulating PANI on reduced graphene oxide for polymer nanocomposites with low dielectric loss and high dielectric constant. *Journal of Materials Chemistry*, **22**, 23477–23484 (2012).
DOI: [10.1039/C2JM34683D](https://doi.org/10.1039/C2JM34683D)
- [23] Kim B. K., Jang M. W., Park H. C., Jeong H. M., Kim E. Y.: Effect of graphene doping of holographic polymer-dispersed liquid crystals. *Journal of Polymer Science Part A: Polymer Chemistry*, **50**, 1418–1423 (2012).
DOI: [10.1002/pola.25909](https://doi.org/10.1002/pola.25909)

- [24] Longun J., Iroh J. O.: Nano-graphene/polyimide composites with extremely high rubbery plateau modulus. *Carbon*, **50**, 1823–1832 (2012). DOI: [10.1016/j.carbon.2011.12.032](https://doi.org/10.1016/j.carbon.2011.12.032)
- [25] Yoonessi M., Shi Y., Scheiman D. A., Lebron-Colon M., Tigelaar D. M., Weiss R. A., Meador M. A.: Graphene polyimide nanocomposites; Thermal, mechanical, and high-temperature shape memory effects. *ACS Nano*, **6**, 7644–7655 (2012). DOI: [10.1021/nn302871y](https://doi.org/10.1021/nn302871y)
- [26] Chen D., Zhu H., Liu T.: *In situ* thermal preparation of polyimide nanocomposite films containing functionalized graphene sheets. *ACS Applied Materials and Interfaces*, **2**, 3702–3708 (2010). DOI: [10.1021/am1008437](https://doi.org/10.1021/am1008437)
- [27] Xu Z., Buehler M. J.: Geometry controls conformation of graphene sheets: Membranes, ribbons, and scrolls. *ACS Nano*, **4**, 3869–3876 (2010). DOI: [10.1021/nn100575k](https://doi.org/10.1021/nn100575k)
- [28] Wei Y., Yang C., Ding T.: A one-step method to synthesize N,N'-bis(4'-aminophenyl)-1,4-quinonediiimine and its derivatives. *Tetrahedron Letters*, **37**, 731–734 (1996). DOI: [10.1016/0040-4039\(95\)02300-3](https://doi.org/10.1016/0040-4039(95)02300-3)
- [29] Huang K-Y., Shiu C-L., Wu P-S., Wei Y., Yeh J-M., Li W-T.: Effect of amino-capped aniline trimer on corrosion protection and physical properties for electroactive epoxy thermosets. *Electrochimica Acta*, **54**, 5400–5407 (2009). DOI: [10.1016/j.electacta.2009.04.030](https://doi.org/10.1016/j.electacta.2009.04.030)
- [30] Hummer W., Offerman R.: Preparation of graphitic oxide. *Journal of the American Chemical Society*, **80**, 1339 (1958). DOI: [10.1021/ja01539a017](https://doi.org/10.1021/ja01539a017)
- [31] Yang D., Velamakanni A., Bozoklu G., Park S., Stoller M., Piner R. D., Stankovich S., Jung I., Field D. A., Ventrice Jr C. A., Ruoff R. S.: Chemical analysis of graphene oxide films after heat and chemical treatments by X-ray photoelectron and micro-Raman spectroscopy. *Carbon*, **47**, 145–152 (2009). DOI: [10.1016/j.carbon.2008.09.045](https://doi.org/10.1016/j.carbon.2008.09.045)
- [32] Liu W-R., Kuo S-L., Lin C-Y., Chiu Y-C., Su C-Y., Wu H-C., Hsieh C-T.: Characterization and electrochemical behavior of graphene-based anode for li-ion batteries. *The Open Materials Science Journal*, **5**, 236–241 (2011). DOI: [10.2174/1874088X01105010236](https://doi.org/10.2174/1874088X01105010236)
- [33] Kuo S-L., Liu W-R., Kuo C-P., Wu N-L., Wu H-C.: Lithium storage in reduced graphene oxides. *Journal of Power Sources*, **244**, 552–556 (2013). DOI: [10.1016/j.jpowsour.2013.01.186](https://doi.org/10.1016/j.jpowsour.2013.01.186)
- [34] Chang K-C., Lai M-C., Peng C-W., Chen Y-T., Yeh J-M., Lin C-L., Yang J-C.: Comparative studies on the corrosion protection effect of DBSA-doped polyaniline prepared from *in situ* emulsion polymerization in the presence of hydrophilic Na⁺-MMT and organophilic organo-MMT clay platelets. *Electrochimica Acta*, **51**, 5645–5653 (2006). DOI: [10.1016/j.electacta.2006.02.039](https://doi.org/10.1016/j.electacta.2006.02.039)
- [35] Huang K-Y., Shiu C-L., Su Y-A., Yang C-C., Yeh J-M., Wei Y., Lee K-R.: Preparation and gas transport properties of dense fluoroaniline copolymer membranes. *Journal of Membrane Science*, **339**, 171–176 (2009). DOI: [10.1016/j.memsci.2009.04.046](https://doi.org/10.1016/j.memsci.2009.04.046)
- [36] Tseng I-H., Chang J-C., Huang S-L., Tsai M-H.: Enhanced thermal conductivity and dimensional stability of flexible polyimide nanocomposite film by addition of functionalized graphene oxide. *Polymer International*, **62**, 827–835 (2013). DOI: [10.1002/pi.4375](https://doi.org/10.1002/pi.4375)
- [37] Luong N. D., Hippel U., Korhonen J. T., Soininen A. J., Ruokolainen J., Johansson L-S., Nam J. D., Sinh L. H., Seppälä J.: Enhanced mechanical and electrical properties of polyimide film by graphene sheets via *in situ* polymerization. *Polymer*, **52**, 5237–5242 (2011). DOI: [10.1016/j.polymer.2011.09.033](https://doi.org/10.1016/j.polymer.2011.09.033)
- [38] Shi H., Li Y., Guo T.: *In situ* preparation of transparent polyimide nanocomposite with a small load of graphene oxide. *Journal of Applied Polymer Science*, **128**, 3163–3169 (2013). DOI: [10.1002/app.38519](https://doi.org/10.1002/app.38519)
- [39] Tsai M-H., Tseng I-H., Liao Y-F., Chiang J-C.: Transparent polyimide nanocomposites with improved moisture barrier using graphene. *Polymer International*, **62**, 1302–1309 (2013). DOI: [10.1002/pi.4421](https://doi.org/10.1002/pi.4421)
- [40] Beving D. E., McDonnell A. M. P., Yang W. S., Yan Y. S.: One general solution formulation for aluminum alloy AA-2024-T3, AA-5052-H32, AA-6061-T4, and AA-7075-T6. *Journal of the Electrochemical Society*, **153**, B325–B329 (2006). DOI: [10.1149/1.2207845](https://doi.org/10.1149/1.2207845)
- [41] Stern M., Geary A. L.: Electrochemical polarization I. A theoretical analysis of the shape of polarization curves. *Journal of the Electrochemical Society*, **104**, 56–63 (1957). DOI: [10.1149/1.2428496](https://doi.org/10.1149/1.2428496)
- [42] Bockris J., Reddy K. N.: *Modern electrochemistry*. Plenum Press, New York (1976).
- [43] Park S-M., Yoo J-S.: Electrochemical impedance spectroscopy for better electrochemical measurements. *Analytical Chemistry*, **75**, 455A–461A (2003). DOI: [10.1021/ac0313973](https://doi.org/10.1021/ac0313973)
- [44] Amirudin A., Thierry D.: Application of electrochemical impedance spectroscopy to study the degradation of polymer-coated metals. *Progress in Organic Coatings*, **26**, 1–28 (1995). DOI: [10.1016/0300-9440\(95\)00581-1](https://doi.org/10.1016/0300-9440(95)00581-1)
- [45] Zucchi F., Grassi V., Frignani A., Monticelli C., Trabianelli G.: Electrochemical behaviour of a magnesium alloy containing rare earth elements. *Journal of Applied Electrochemistry*, **36**, 195–204 (2006). DOI: [10.1007/s10800-005-9053-3](https://doi.org/10.1007/s10800-005-9053-3)

- [46] Kannan M. B., Gomes D., Dietzel W., Abetz V.: Polyoxadiazole-based coating for corrosion protection of magnesium alloy. *Surface and Coatings Technology*, **202**, 4598–4601 (2008).
DOI: [10.1016/j.surfcoat.2008.03.027](https://doi.org/10.1016/j.surfcoat.2008.03.027)
- [47] Rammelt U., Reinhard G.: Application of electrochemical impedance spectroscopy (EIS) for characterizing the corrosion-protective performance of organic coatings on metals. *Progress in Organic Coatings*, **21**, 205–226 (1992).
DOI: [10.1016/0033-0655\(92\)87005-U](https://doi.org/10.1016/0033-0655(92)87005-U)
- [48] Wessling B.: Passivation of metals by coating with polyaniline: Corrosion potential shift and morphological changes. *Advanced Materials*, **6**, 226–228 (1994).
DOI: [10.1002/adma.19940060309](https://doi.org/10.1002/adma.19940060309)
- [49] Wessling B.: Scientific and commercial breakthrough for organic metals. *Synthetic Metals*, **85**, 1313–1318 (1991).
DOI: [10.1016/S0379-6779\(97\)80254-8](https://doi.org/10.1016/S0379-6779(97)80254-8)
- [50] Tseng I-H., Liao Y-F., Chiang J-C., Tsai M-H.: Transparent polyimide/graphene oxide nanocomposite with improved moisture barrier property. *Materials Chemistry and Physics*, **136**, 247–253 (2012).
DOI: [10.1016/j.matchemphys.2012.06.061](https://doi.org/10.1016/j.matchemphys.2012.06.061)
- [51] Wessling B.: Corrosion prevention with an organic metal (polyaniline): Surface ennobling, passivation, corrosion test results. *Materials and Corrosion*, **47**, 439–445 (1996).
DOI: [10.1002/maco.19960470804](https://doi.org/10.1002/maco.19960470804)
- [52] Lu W-K., Elsenbaumer R. L., Wessling B.: Corrosion protection of mild steel by coatings containing polyaniline. *Synthetic Metals*, **71**, 2163–2166 (1995).
DOI: [10.1016/0379-6779\(94\)03204-J](https://doi.org/10.1016/0379-6779(94)03204-J)
- [53] Fahlman M., Jasty S., Epstein A. J.: Corrosion protection of iron/steel by emeraldine base polyaniline: An X-ray photoelectron spectroscopy study. *Synthetic Metals*, **85**, 1323–1326 (1997).
DOI: [10.1016/S0379-6779\(97\)80256-1](https://doi.org/10.1016/S0379-6779(97)80256-1)
- [54] Potts J. R., Dreyer D. R., Bielawski C. W., Ruoff R. S.: Graphene-based polymer nanocomposites. *Polymer*, **52**, 5–25 (2011).
DOI: [10.1016/j.polymer.2010.11.042](https://doi.org/10.1016/j.polymer.2010.11.042)

Mapping physicochemical surface modifications of flame-treated polypropylene

S. Farris^{1*}, S. Pozzoli¹, S. La Vecchia¹, P. Biagioni², C. L. Bianchi³, L. Piergiovanni¹

¹DeFENS, Department of Food, Environmental and Nutritional Science, Packaging Division – University of Milan, Via Celoria 2, 20133 Milan, Italy

²Dipartimento di fisica and CNISM, Politecnico di Milano, Piazza L. da Vinci 32, 20133 Milano, Italy

³Department of Chemistry, University of Milan, Via Golgi 19, I, 20133 Milano, Italy

Received 14 October 2013; accepted in revised form 1 December 2013

Abstract. The aim of this work was to investigate how the surface morphology of polypropylene (PP) is influenced by the surface activation mediated by a flame obtained using a mixture of air and propane under fuel-lean (equivalence ratio $\phi = 0.98$) conditions. Morphological changes observed on flamed samples with smooth (S), medium (M), and high (H) degree of surface roughness were attributed to the combined effect of a chemical mechanism (agglomeration and ordering of partially oxidized intermediate-molecular-weight material) with a physical mechanism (flattening of the original roughness by the flame's high temperature). After two treatments, the different behavior of the samples in terms of wettability was totally reset, which made an impressive surface energy of $\sim 43 \text{ mJ}\cdot\text{m}^{-2}$ possible, which is typical of more hydrophilic polymers (e.g., polyethylene terephthalate – PET). In particular, the polar component was increased from 1.21, 0.08, and $0.32 \text{ mJ}\cdot\text{m}^{-2}$ (untreated samples) to 10.95, 11.20, and $11.17 \text{ mJ}\cdot\text{m}^{-2}$ for the flamed samples S, M, and H, respectively, an increase attributed to the insertion of polar functional groups (hydroxyl and carbonyl) on the C–C backbone, as demonstrated by the X-ray photoelectron spectroscopy results.

Keywords: coatings, flame treatment, polypropylene, surface activation, wettability

1. Introduction

Since its discovery in 1954 [1], polypropylene (PP) has become increasingly important for fabricating the materials, objects, goods, and commodities of everyday life [2]. The reason for this long-lasting growth lies mainly in the properties of PP, such as chemical resistance to most organic solvents, fatigue resistance, high clarity, very good water vapor barrier properties, compatibility with many processing techniques, low density, easy recyclability and – not least of all – moderate cost. Although PP's inability to stand thermal stresses and its poor gas barrier properties may hinder its use for certain applications, the major hurdle is probably its surface properties. Like any polyolefin, PP exhibits low surface free energy

values ($\sim 28 \text{ mJ}\cdot\text{m}^{-2}$), which are due in essence to its inherent hydrophobicity. This is reflected primarily in the high recalcitrance of polypropylene surfaces toward the deposition of substances (e.g., liquids) with a high polar component: it totally frustrates the establishment of either interatomic or intermolecular interactions at the interface [3]. This repulsion dramatically affects all technical processes where wettability and improved adhesion are required. Printability, lamination, and anti-fog properties, as well as the processability, convertibility, recyclability, and biodegradability of the final materials depend strongly on the possibility of enhancing the polypropylene substrate's surface properties. Consequently, enhancing the surface activation of poly-

*Corresponding author, e-mail: stefano.farris@unimi.it
© BME-PT

propylene (and, more generally, of polyolefins) has attracted (and still does) worldwide interest both in academia and in industrial research [4].

With reference to the source of activation (and not to the type of modification induced on the polymer surface) the main routes used to improve the surface energy of polyolefins can be grouped into chemical and physical methods [5]. Physical methods, however, are the most extensively used because they allow the provision of more precise surface modification without requiring rigorous process control, and because, involving no chemical reagents and therefore no disposal of waste liquids, they are environmentally safe and clean processes [6]. Among the wide spectrum of physical methods currently available for the surface modification of plastics (flame [7], corona discharge [8], UV [9], gamma-ray [10], electron beam [11], ion beam [12], plasma [13], and laser treatments [14]), flame treatment and corona discharge are the most widespread, especially in particular sectors such as packaging and automotive, which has primarily been ascribed to the lower cost of these methods. It has been pointed out, however, that flame treatment is probably the most suited for the surface activation of polyolefins and, within this category, polypropylene [15]. Nevertheless, the great potential involved in the flame treatment was underexploited until 1980s [16], when remarkable innovations at both the technical (e.g., the introduction of the polarized flame) and the safety level renewed interest in this method. Correspondingly, the acquisition of new powerful techniques such as optical contact angle (OCA) [17], atomic force microscopy (AFM) [18], and X-ray photoelectron spectroscopy (XPS) [19–21] prompted a fervid scientific activity, as demonstrated by the number of scientific papers in this area [16, 22–24].

At the present time, interest toward flame treatment relies mainly on the innovations expected in many areas for the next years. New developments will take place according to specific trends, among which the environmental aspect seems to be one of the main driving forces. Many companies are progressively looking for new, high-performance materials that are perceived by consumers as environmentally friendly and safe. Legislation also forces new trends [25]. Since water-based coatings are expected to play a major role in the future, the flame treatment technique may play a pivotal role in dictating the success of their deposition on PP. However, to make

the flame treatment effective towards high-recalcitrant substrates, knowing the basic principles underlying the overall process is of utmost importance [26]. This in turn will enable optimization of the main process variables to pinpoint the best operating conditions for any specific application [27]. A key factor possibly influencing the efficacy of the flame treatment is the sample's topography. There is, however, a lack of information on how surface roughness affects the activation of polypropylene substrates mediated by a flame [26].

This work was aimed at filling this gap by investigating how the substrate topography influenced the flame treatment's overall effect, by taking into account both the physical and the chemical changes that the process induced. To this end, the benefits possibly linked to changes in the surface roughness of polypropylene samples in terms of surface energy were quantitatively described. The effect of an increasing number of sequential treatments was also discussed. This was accomplished by OCA and AFM techniques, whereas XPS analysis was used to gather detailed information on the chemical changes induced by the flame.

2. Experimental section

2.1. Polymer samples

Square plaques 40 mm wide and 3 mm thick were used throughout the experiments. They were produced by injection-molding, starting from PP pellets (Moplen RP340R, Basell Polyolefins srl, Ferrara, Italy; nucleated heterophasic random copolymer, melt flow index according to ISO 1133: 25 g/10 min, density according to ISO 1183: 0.905 g/cm³, melting range = 140–163°C), fed into the heated barrel, mixed through a screw, and injected into a multiple-cavity mold (each cavity having identical geometry). The mold is then held under pressure until the material cools and hardens, after which the mold is opened and the part is removed. To produce plaques with different surface topographies, interchangeable molds with front panel of three different roughness degrees (perfect smoothness – S, medium roughness – M, and high roughness – H) were used. Unlike usual injection-molding manufacturing operations, the use of any release agent (which helps in the detachment of the object from the mold) was avoided, to prevent potential interference with the contact angle measurements. Injection-molded (OCSA spa, Creazzo, Italy) PP

(Moplen RP340R, nucleated heterophasic random copolymer, Basell Polyolefins srl, Ferrara, Italy) square plaques (40 mm wide, 3 mm thick) with different roughness degrees (perfect smoothness – S, medium roughness – M, and high roughness – H) were used in this work. The different roughness was achieved using interchangeable plates with a different surface morphology during the injection-molding process.

2.2. Surface modification apparatus and procedures

Flame treatment was performed with pilot-plant-flaming equipment built within the laboratories at the Packaging Division of DeFENS (University of Milan). An explanatory scheme is shown in Figure 1. It basically consists of a feeding system (fuel and oxidizer cylinders) connected to a fuel/oxidizer mix generator (mod. EI-080, esseCI srl, Narni, Italy); two single-flow-tube universal rotameters (ASA, Sesto S. Giovanni, Italy), one for the oxidizer (mod. 1901, flow range_{air} 85–850 L·h⁻¹, 1013 mbar, 20°C), one for the fuel (flow range_{air} 4–115 L·h⁻¹, 1013 mbar, 20°C); a pressure gauge; an in-line mixture sampling device; a 100 mm×20 mm ribbon burner with no-return flame valves (esseCI srl, Narni, Italy); and a sample holder composed by an aluminum rotating plate and a speed-regulating automatic

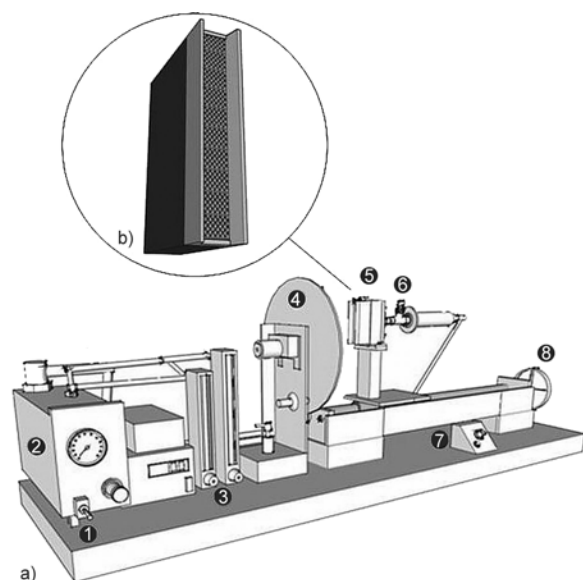


Figure 1. (a) Schematic representation of the flame treatment apparatus: 1 – manual start; 2 – gas/air mixer; 3 – gas and air flow rotameters; 4 – rotating sample holder; 5 – ribbon burner; 6 – gas/air mixture sampling valve; 7 – sample holder speed control (relay); 8 – flame-to-sample gap manual adjuster. (b) Magnification of the ribbon burner.

device. Ignition of the flame was accomplished by an electric spark.

The configuration of the flaming treatment made it possible to adjust the main process variables, such as the fuel/oxidizer ratio, the mixture flow, the flame/surface gap (i.e., the distance between the tips of the luminous flame cones and polyolefin surface), the sample's time of exposure to the flame, and the number of sequential treatments. The oxidizer used in this work was compressed air (Siad, Osio Sopra, Italy), whereas the fuel was commercial-grade liquid propane (GPL, Sarpomsrl, Trecate, Italy) with an average density of 0.5174 kg·L⁻¹ and average heat content of 93.1 kJ·L⁻¹ (2500 BTU·ft⁻³). The average volumetric composition of GPL is as follows: C3 hydrocarbons, 93.9%; C4 hydrocarbons, 5.8%; C2 hydrocarbons, 0.3%; total sulfur content, 8.0 mg·kg⁻¹; water content, 18 mg·kg⁻¹.

Flame treatments were performed by a propane/air equivalence ratio of 0.98. According to Equation (1), the equivalence ratio (φ) is defined as the actual mass gas/air ratio used during treatment divided by the stoichiometric fuel-to-oxidizer ratio [28]:

$$\varphi = \frac{\frac{m_{\text{fuel}}}{m_{\text{oxidizer}}}}{\left(\frac{m_{\text{fuel}}}{m_{\text{oxidizer}}}\right)_{\text{stoichiometric}}} \quad (1)$$

The value selected in this work ($\varphi = 0.98$) accounts for the better performance of oxidizing flames ($\varphi < 1$) compared with both stoichiometric ($\varphi = 1$) and fuel-rich ($\varphi > 1$) flames [29–31]. The equivalence ratio value was continuously monitored throughout the experiments by the sampling of a constant amount (30 μL) of the mixture, and its analysis by a gas-chromatograph coupled with a flame ionization detector (GC-FID PR 2100 Perichrom, Saulx les Chartreux, France). The C₃H₈ was separated from the other components in the mixtures by a 80/100 mesh Porapak[®] T packed column (182.88 cm length; 3.175 cm external diameter; 2.159 cm internal diameter). The column inlet was set in splitless mode at 105°C and 75 kPa. The column temperature was isothermal at 150°C, with a helium carrier flow of 38 mL·min⁻¹. The FID system (260°C, 75 kPa, 10⁻¹⁰ A/mV gain) was fuelled with pure oxygen at 420 mL·min⁻¹ and hydrogen at 30 mL·min⁻¹. Finally, an equivalence ratio of 0.98 was achieved by a flow setting of 700 and 74.5 L·h⁻¹ for compressed air and

propane, at an outlet pressure of ~5.5 and ~2.8 bar, respectively.

Additional operating conditions were: substrate-to-flame distance, 5.0 mm; flame contact time, 0.05 s. To assess the influence of the number of flame treatments, polypropylene surfaces were exposed to 1 or 2 sequential treatments; in the latter case, between two flame passes, the samples were allowed to rest for 10 s for the polymer's surface to cool down. The flame power, i.e. the product of the volume of fuel burned per unit time (80 L·h⁻¹ in our work) and the heat content of the fuel (93.1 kJ·L⁻¹) was approximately equal to 6938 kJ·h⁻¹, corresponding to ~1927 W. Since the effective burning surface (namely the sum of the area of the 129 holes of the burner grid ejecting the flame cones) amounted to 3.3 cm², the unit flame power was equal to ~584 W cm⁻², which yielded tip-luminous cones that were approximately 3 mm tall.

2.3. Physicochemical characterization

Contact angle measurements

Surface activation of polypropylene samples was firstly assessed by an optical contact angle apparatus (OCA 15 Plus – Data Physics Instruments GmbH, Filderstadt, Germany) equipped with a video measuring system with high-resolution CCD camera and a high-performance digitizing adapter. The software SCA 20 (Data Physics Instruments GmbH, Filderstadt, Germany) was used for data acquisition. For flamed samples, each contact angle measurement was performed immediately (~10 s) after the treatment. Rectangular (5 cm×2 cm) polypropylene samples (untreated and flame-treated) were fixed throughout the analysis by means of a special sample holder with parallel clamping jaws. The contact angle (θ [°]) of both water (Milli-Q water, 18.3 M Ω ·cm, liquid-vapor surface tension $\gamma_{LV} = 72.81$ mJ·m⁻²) and methylene iodide (Sigma-Aldrich, Milan, Italy; liquid-vapor surface tension $\gamma_{LV} = 50.82$ mJ·m⁻²) in air was thus measured by the sessile drop method, by gentle dropping of a 4±0.5 μ L droplet of water onto the coated surface of the plastic substrate, according to the so-called pick-up procedure (whereby the droplet hanging down the needle is laid on the coating surface by raising of the sample stage until the solid/liquid contact is reached). All droplets were released from 1 cm above the surface to minimize the inconsistency between each measurement. Each analysis was

replicated at least ten times, and the mean contact angles were then used for all subsequent calculations. The surface energy of the solid (γ_{SV}) was determined by the Owens and Wendt theory, using Equation (2) [32]:

$$(1 + \cos\theta)\gamma_{LV} = 2(\sqrt{\gamma_{LV}^d\gamma_{SV}^d} + \sqrt{\gamma_{LV}^p\gamma_{SV}^p}) \quad (2)$$

which is widely used for the surface characterization of low-surface energy polymers (e.g., polyolefins) [33]. Since the values of the polar (γ_{LV}^p) and dispersive (γ_{LV}^d) components of both water ($\gamma_{LV}^p = 51.0$ mJ·m⁻²; $\gamma_{LV}^d = 21.8$ mJ·m⁻²) and methylene iodide ($\gamma_{LV}^p = 0$ mJ·m⁻²; $\gamma_{LV}^d = 50.8$ mJ·m⁻²) are known, the dispersive and polar components of the solid's surface tension (γ_{SV}^d and γ_{SV}^p , respectively) can easily be drawn. Finally, the surface energy of the polyolefin surface is obtained according to Equation (3):

$$\gamma_{SV} = \gamma_{SV}^d + \gamma_{SV}^p \quad (3)$$

Atomic force microscopy (AFM)

AFM maps were collected in 'soft' contact mode stabilized by the standard optical-lever method with a very small force offset, using a commercial setup (AlphaSNOM, WITec GmbH, Germany). The height variation in the resulting topography maps is represented by a color scale, in which bright and dark colors denote higher and lower heights, respectively. The root mean square roughness R was evaluated for each sample as the standard deviation of the topography over the 95×95 μ m² scanning area ($M \times N$ pixels), by means of Equation (4):

$$R = \sqrt{\frac{1}{MN} \sum_{i=1}^M \sum_{j=1}^N |z(x_i, y_j) - \bar{z}|^2} \quad (4)$$

where \bar{z} is the mean value of the topography $z(x, y)$ [34]. The so-called 'ironed surface', i.e. the true exposed surface area, is also calculated for each map by means of a standard commercial software.

X-ray photoelectron spectroscopy (XPS)

XPS measurements were performed in an M-Probe instrument (Surface Science Instruments, USA) equipped with a monochromatic Al K α source (1486.6 eV) with a spot size of 200 μ m×750 μ m and a pass energy of 25 eV, providing a resolution for 0.74 eV. The energy scale was calibrated with

reference to the $4f_{7/2}$ level of a freshly evaporated gold sample, at 84.0 ± 0.1 eV, and with reference to the $2p_{3/2}$ and $3s$ levels of copper at 932.47 ± 0.1 and 122.39 ± 0.15 eV, respectively. With a monochromatic source, an electron flood gun was used to compensate for the buildup of positive charge on the insulator samples during the analyses: a value of 10 eV was selected for these samples to be measured. For all the samples, the C 1s peak level was taken as internal reference at 284.6 eV. The accuracy of the reported binding energies (BE) can be estimated to be ± 0.2 eV.

3. Results and discussion

3.1. Morphology

The effect of flame treatment on the surface roughness of polyolefins has been investigated in previous studies [35]. It slightly smoothed the surface in some cases [27], while in others it had no effect [16, 36]. The different morphology of the untreated PP plaques is confirmed by the AFM images (Figure 2) and by the indices R and I_S (Table 1). The H-type sample is clearly the roughest with $R \sim 22$ times and ~ 2 times larger than samples S and M, respectively. The same trend was observed for the I_S index, which accounts for the total amount of exposed surface.

Visual inspection of the different AFM maps reveals that the main change in the sample topography ensuing from the flame treatments lies in the appearance of new aggregates with a size in the few-micrometer range. While such aggregates are well-rendered in Figure 2b and 2c, i.e. for the treated S sample, their presence on the treated rougher samples is partially hidden in the image by the overall large height fluctuation of the sample topography. To better visualize these aggregates, we applied a line-by-line correction by subtraction of a

Table 1. Root mean squares roughness (R [μm]) and ironed surface (I_S [μm^2]) of untreated, 1-step-treated, and 2-step-treated PP plaques at different roughness

PP type	Untreated plaques		1step-treated plaques		2 step-treated plaques	
	Morphological parameter		Morphological parameter		Morphological parameter	
	R	I_S	R	I_S	R	I_S
S	0.06	9068	0.092	9075	0.098	9084
M	0.60	9286	0.570	9189	0.531	9165
H	1.34	9329	1.480	9197	1.184	9237

S – smooth; M – medium roughness; H – high roughness.

7th-order fitting curve, obtaining the maps shown in Figure 3, where the presence of the small aggregates is even more evident. According to Strobel *et al.* [37], we are inclined to believe that the original topography of the PP surfaces treated with a fuel-lean flame is altered by a new physical arrangement of PP molecular chains, specifically the agglomeration and ordering of partially oxidized intermediate-molecular-weight material formed in the treatment. Therefore, the new morphology detected on the PP plaques should be considered the result of the combined effect of temperature (flattening of the original roughness) and oxidation of the PP caused by the flame (formation of new aggregates). Conversely, the formation of low-molecular-weight oxidized material (LMWOM), typical of corona-treated PP [38], should here be excluded. This is because the presence of LMWOM has been associated with extensive chain scission primarily involving atomic oxygen. However, it has been demonstrated that, during flame treatment, the concentration of O is very low relative to the concentration of OH and the other active species, which explains the lack of LMWOM [37]. This, in turn, is the main reason why flame-treated PP is more stable than corona-treated PP as a function of storage time under ambient conditions [19, 22, 39].

3.2. Wettability

In Table 2 the values of contact angles for water ($\theta_{(w)}$) and methylene iodide ($\theta_{(d)}$) and the solid-liquid surface energy (γ_{SV}) with the disperse and polar components (γ_{SV}^d , γ_{SV}^p) are reported for untreated, 1-step-treated and 2-step-treated PP samples. Figure 4 displays instead the typical water contact angle profile for an H-type PP plaque before treatment and after one and two sequential treatments. Similar to the untreated samples, the highest surface energy was measured for the smoother type (S), which also had the highest polar component ($1.21 \text{ mJ}\cdot\text{m}^{-2}$). The lowest surface energy was instead encountered for the H-type sample, despite the higher polar component ($0.32 \text{ mJ}\cdot\text{m}^{-2}$) compared with the M sample ($0.08 \text{ mJ}\cdot\text{m}^{-2}$). This observation can be explained when we take into account the ‘roughness effect’ described by the Cassie-Baxter theory, which suggests an increase, proportional to surface roughness, in the hydrophobic attribute of inherently hydrophobic surfaces [40]. Eventually, the contribution arising from the rougher topogra-

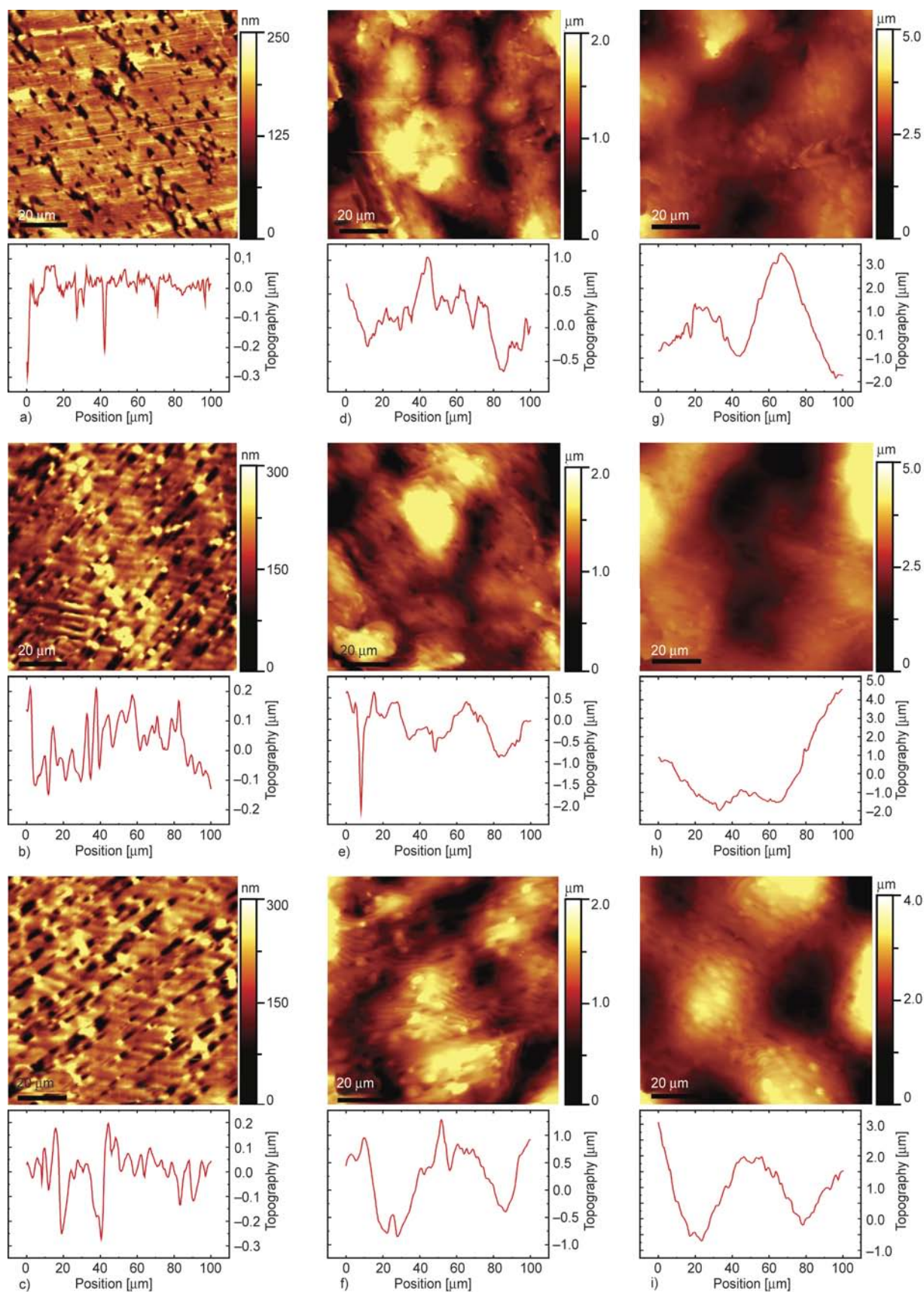


Figure 2. $95 \times 95 \mu\text{m}^2$ AFM height maps of samples S [first column, (a)–(c)], M [second column, (d)–(f)], and H [third column, (g)–(i)] before flame treatment (first row), after 1 step (second row), and after 2 steps (third row) flame treatment. A representative line profile is also reported below each map.

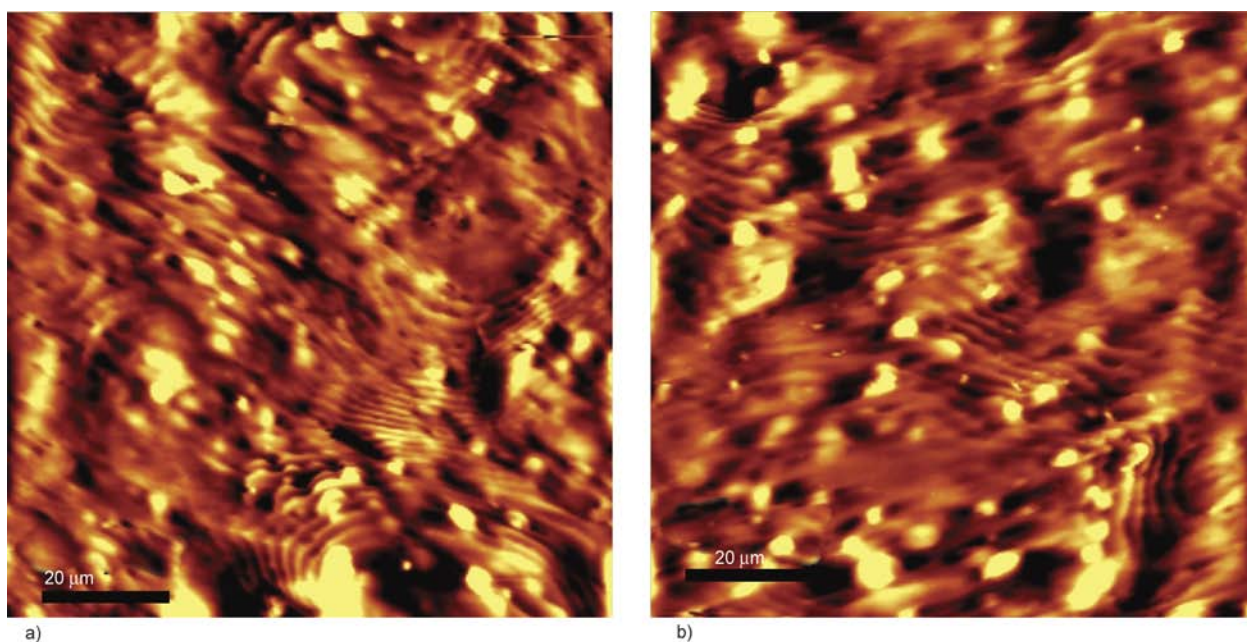


Figure 3. Corrected topography maps after 7th-order line-by-line correction of the M [panel (a)] and H [panel (b)] samples after 2 flame treatments.

Table 2. Static water (*w*) and methylene iodide (*d*) contact angles (θ [°]), solid surface energy (γ_{SV} [mJ·m⁻²]) and its components (γ_{SV}^d and γ_{SV}^p [mJ·m⁻²]) of untreated, 1-step-treated, and 2-step-treated PP plaques at different roughness

PP type	Untreated plaques					1-step-treated plaques					2-step-treated plaques				
	Thermodynamic parameter					Thermodynamic parameter					Thermodynamic parameter				
	$\theta_{(w)}$	$\theta_{(d)}$	γ_{SV}	γ_{SV}^d	γ_{SV}^p	$\theta_{(w)}$	$\theta_{(d)}$	γ_{SV}	γ_{SV}^d	γ_{SV}^p	$\theta_{(w)}$	$\theta_{(d)}$	γ_{SV}	γ_{SV}^d	γ_{SV}^p
S	95.40 ^a ±0.99	54.28 ^a ±1.53	31.89	30.68	1.21	72.38 ^a ±1.65	46.46 ^a ±1.26	40.65	31.41	9.24	68.57 ^a ±1.46	43.90 ^a ±1.30	43.16	32.21	10.95
M	104.74 ^b ±1.18	56.33 ^b ±1.14	31.07	30.99	0.08	74.63 ^b ±1.16	47.66 ^a ±1.83	39.32	31.08	8.24	68.10 ^a ±2.20	43.75 ^a ±1.04	43.41	32.21	11.20
H	103.75 ^b ±1.29	61.34 ^c ±0.99	27.91	27.59	0.32	73.32 ^a ±1.54	43.22 ^b ±0.95	40.67	32.14	8.54	68.12 ^a ±2.68	43.68 ^a ±2.07	43.42	32.25	11.17

Different letters within group (i.e., column) denote statistically significant differences between samples ($p < 0.05$).

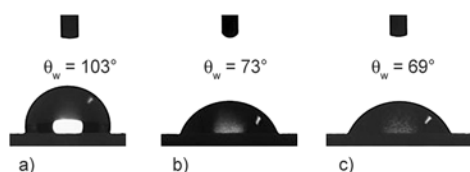


Figure 4. Typical water contact angle (θ_w) profile for an H-type PP plaque: (a) before flame treatment; (b) after one treatment; (c) after two treatments

phy of the H sample overcompensated for the effect of the higher polar component, finally yielding a higher surface energy value.

The flame’s effect on the wettability attribute of the PP plaques was decidedly marked. As reported in Table 2 (dataset in the middle), the activation of the PP surface by one treatment was achieved inso-much as the water contact angle was decreased by ~24, ~29, and ~30% for the samples S, M, and H, respectively, with corresponding surface energy values of ~40 mJ·m⁻² for all three sample types. The

relevance of this result can be better understood by the consideration that the value of ~38 mJ·m⁻² is, in most applications, the minimum surface energy value required to achieve an adequate adhesion strength between a polymeric material (e.g., plastic substrates) and the adherend (e.g., water-based adhesives, inks, paints and, more generally, coating systems).

After two treatments, the efficacy of the flame treatment in changing the PP samples’ wettability properties was increased. As reported in Table 2 (last dataset on the right), contact angle values as high as ~68° were eventually obtained, which implies surface energy values of approximately 43 mJ·m⁻². Noticeably, the latter is a typical value recorded for more hydrophilic polymers, such as polyethylene terephthalate (PET). Not less important is the increase in the polar component of the PP surfaces ensuing

from the flame treatment, which was $\sim 11 \text{ mJ}\cdot\text{m}^{-2}$ for all three types of plaques (Table 2).

3.3. Surface chemistry

Appreciation of the elemental surface composition of both untreated and flame-treated samples was gathered by XPS measurements. Untreated PP plaques exhibited a single peak related to the C 1s signal (Figure 5a). This is the non-functionalized carbon (C–C), at a binding energy (BE) of 284.7 eV

(this peak is taken as the reference peak) [41]. Neither oxygen nor nitrogen was detected (Table 3). Two-step flamed samples disclosed a different spectrum, characterized by both traces of contaminants and of the products of the flame treatment. Contaminants such as Si, F, Ca, and S arise from additives/technological aids migrated to the polymer surface. Since their contents were small and did not appreciably vary after the flame treatment, their contribution was neglected. Main peaks on the flamed sam-

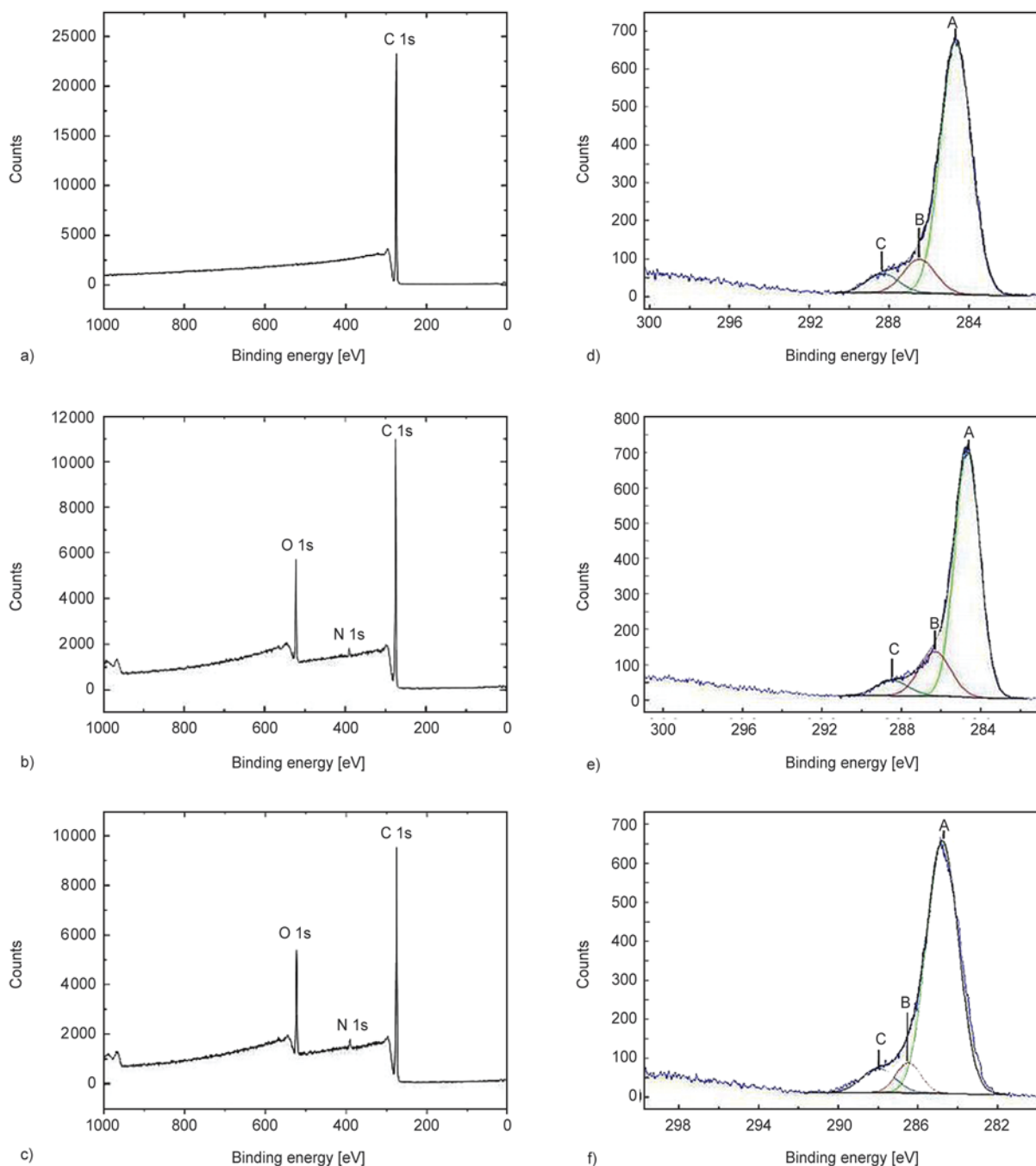


Figure 5. Left panels: raw scan spectra of untreated (a) and 2-step-treated samples S (b) and H (c); right panels: fitting of the C 1s peaks for samples S (d), M (e), and H (f)

Table 3. Elemental surface composition of polyolefin samples before and after flame treatments, determined by XPS. Note that the treated samples S, M, and H have been subjected to 2 sequential passes (interval between passes = 10 s).

Sample	C [%]	O [%]	N [%]
Untreated	100.0	–	–
S	83.7	14.1	2.2
M	83.5	14.0	2.5
H	83.3	13.8	2.9

ples were due to the functionalization of the C–C backbone by the flame’s oxidizing effect. As indicated by the new peak at ~ 532 eV in Figure 5b (sample S) and Figure 5c (sample H), all three samples (*viz.* S, M, and H morphologies) experienced a marked increase in oxygen content after the treatment ($\sim 14\%$, see Table 3). This value is in line with those reported by Papirer *et al.* [23] for 2-step-treated PP. Further information on the type of functional groups ensuing from the oxidation of the C–C backbone can be obtained by fitting of the C 1s peak using a combination of Gaussian and Lorentzian curves.

This allowed disclosing three main components: (i) nonfunctionalized carbon (C–C) at 284.6 eV; (ii) carbon carrying hydroxyl groups (C–OH) at $\sim 286.6 \pm 0.2$ eV; and (iii) carbon involved in carbonyl groups (C=O) at $\sim 289.0 \pm 0.2$ eV [42]. These three components are respectively denoted by the letters A, B, and C, in Figures 5d–5f, for samples S, M, and H. As already reported, the insertion of these new oxygen-containing functional groups onto the C–C skeleton is responsible for the increased wettability and surface energy values of flame-treated PP plaques [43]. It appears, moreover, that most of the new polar functionalities are represented by hydroxyl species (peak denoted as B in Figures 5d–5f), confirming what was reported by Sheng *et al.* [20], who estimated that ~ 20 – 30% of the oxygen added to PP by flame treatment could be in the form of hydroxyl groups. Newly formed nitrogen was also observed (peak at ~ 390 eV) on the flamed samples, with an apparent increase in N content proportional to the sample’s initial roughness. The presence of nitrogen-containing compounds on flame-treated PP is somehow controversial. For example, Pijpers and Meier [21] observed a significant amount of N at the surface of PP samples at air/ propane ratios between 26 and 18, whereas Papirer *et al.*

[23] and Briggs *et al.* [44] reported the appearance of N- derivatives only on flamed polyethylene (PE). The origin of N compounds is not yet well understood. On one hand, the formation of NO_x (among which nitrogen monoxide is the most abundant) could stem from the oxidation of molecular nitrogen (N_2) in combustion air. On the other hand, the presence of N derivatives has been ascribed to N-containing additives/stabilizers (*e.g.*, Tinuvin[®] 770) commonly used in the manufacture of polyolefins [21]. Whatever the origin of N-derivatives, from a practical point of view it would be better to keep their formation during flaming as low as possible. This is because the formation of NO_x , which is in an inverse proportion to CH_x intermediates, would impair the surface activation of the polyolefin surface [26]. Since NO_x formation is promoted by increased temperatures, residence times, and O_2 concentrations, it can easily be controlled during treatment operations by burning under lean conditions and flame-quenching with a secondary air stream. The surface chemistry analysis confirmed what we gathered from both AFM and contact angle measurements. The two-step treatment was sufficiently high to reset any morphological difference between samples, because of the high thermal input (heat) associated with the flame. This, in turn, allowed making void any influence arising from the surface roughness as observed in the pristine (*i.e.*, not treated) samples. The ultimate effect was the chemical modification of the PP surfaces, which occurred to a same extent in the three sample types, as demonstrated by the XPS results.

4. Conclusions

In this work it was demonstrated that the surface topography, which greatly affects the wettability properties of bare polypropylene samples, did not affect the surface activation of the same polymer mediated by flame treatment. After one treatment, the water contact angle was dramatically reduced for both smooth and rough surfaces, although the highest polar component was still recorded for the smooth-type surface. After two treatments, however, any initial difference between samples linked to the heterogeneous morphology was apparently reset, as demonstrated by the comparable values of both surface energy and polar components. This finding may be relevant for all those applications which envisage the use of one individual polymer (such as

PP) with different morphologies (e.g., injection-molded objects). No less important, the flame treatment's efficacy was such as to raise the final surface energy of PP surfaces to $\sim 43 \text{ mJ}\cdot\text{m}^{-2}$, a value comparable to that of inherently hydrophilic/wettable polymers. This was confirmed to be due to the functionalization of the PP backbone by polar functional groups, such as hydroxyl and carbonyl groups.

References

- [1] Hargittai I., Comotti A., Hargittai M.: Giulio Natta. *Chemical and Engineering News*, **81**, 26–28 (2003).
DOI: [10.1021/cen-v081n006.p026](https://doi.org/10.1021/cen-v081n006.p026)
- [2] Maier C., Calafut T. *Polypropylene: The definitive user's guide and databook*. William Andrews Publishing, New York (1998).
- [3] Poisson C., Hervais V., Lacrampe M. F., Krawczak P.: Optimization of PE/binder/PA extrusion blow-molded films. II. Adhesion properties improvement using binder/EVA blends. *Journal of Applied Polymer Science*, **101**, 118–127 (2006).
DOI: [10.1002/app.22407](https://doi.org/10.1002/app.22407)
- [4] Singh R. P.: Surface grafting onto polypropylene – A survey of recent developments. *Progress in Polymer Science*, **17**, 251–281 (1992).
DOI: [10.1016/0079-6700\(92\)90024-S](https://doi.org/10.1016/0079-6700(92)90024-S)
- [5] Zhang G., Liao H., Cherigui M., Davim J. P., Coddet C.: Effect of crystalline structure on the hardness and interfacial adherence of flame sprayed poly(ether–ether–ketone) coatings. *European Polymer Journal*, **43**, 1077–1082 (2007).
DOI: [10.1016/j.eurpolymj.2006.12.039](https://doi.org/10.1016/j.eurpolymj.2006.12.039)
- [6] Ozdemir M., Yurteri C. U., Sadikoglu H.: Physical polymer surface modification methods and applications in food packaging polymers. *Critical Reviews in Food Science and Nutrition*, **39**, 457–477 (1999).
DOI: [10.1080/10408699991279240](https://doi.org/10.1080/10408699991279240)
- [7] Briggs D.: Surface treatments for polyolefins. in 'Surface analysis and pretreatment of plastics and metals' (ed.: Brewis D. M.) MacMillan Publishing, New York, 199–226 (1982).
- [8] Molitor P., Barron V., Young T.: Surface treatment of titanium for adhesive bonding to polymer composites: A review. *International Journal of Adhesion and Adhesives*, **21**, 129–136 (2001).
DOI: [10.1016/S0143-7496\(00\)00044-0](https://doi.org/10.1016/S0143-7496(00)00044-0)
- [9] Lisboa P., Gilliland D., Ceccone G., Valsesia A., Rossi F.: Surface functionalisation of polypyrrole films using UV light induced radical activation. *Applied Surface Science*, **252**, 4397–4401 (2006).
DOI: [10.1016/j.apsusc.2005.07.091](https://doi.org/10.1016/j.apsusc.2005.07.091)
- [10] López D., Burillo G.: Gamma-ray irradiation of polystyrene in the presence of cross-linking agents. in 'Radiation effects on polymers' (eds.: Clough R. L., Shalaby S. W.) ACS Symposium Series, Vol. 475, 262–270 (1991).
DOI: [10.1021/bk-1991-0475.ch016](https://doi.org/10.1021/bk-1991-0475.ch016)
- [11] Murray K. A., Kennedy J. E., McEvoy B., Vrain O., Ryan D., Cowman R., Higginbotham C. L.: The influence of electron beam irradiation conducted in air on the thermal, chemical, structural and surface properties of medical grade polyurethane. *European Polymer Journal*, **49**, 1782–1795 (2013).
DOI: [10.1016/j.eurpolymj.2013.03.034](https://doi.org/10.1016/j.eurpolymj.2013.03.034)
- [12] Ensinger W., Müller H. R.: Surface modification and coating of powders by ion beam techniques. *Materials Science and Engineering: A*, **188**, 335–340 (1994).
DOI: [10.1016/0921-5093\(94\)90389-1](https://doi.org/10.1016/0921-5093(94)90389-1)
- [13] Slepíčka P., Slepíčková Kasalková N., Stránská E., Bačáková L., Švorčík V.: Surface characterization of plasma treated polymers for applications as biocompatible carriers. *Express Polymer Letters*, **7**, 535–545 (2013).
DOI: [10.3144/expresspolymlett.2013.50](https://doi.org/10.3144/expresspolymlett.2013.50)
- [14] Wingfield J. R. J.: Treatment of composite surfaces for adhesive bonding. *International Journal of Adhesion and Adhesives*, **13**, 151–156 (1993).
DOI: [10.1016/0143-7496\(93\)90036-9](https://doi.org/10.1016/0143-7496(93)90036-9)
- [15] Strobel M., Jones V., Lyons C. S., Ulsh M., Kushner M. J., Dorai R., Branch M. C.: A comparison of corona-treated and flame-treated polypropylene films. *Plasmas and Polymers*, **8**, 61–95 (2003).
DOI: [10.1023/A:1022817909276](https://doi.org/10.1023/A:1022817909276)
- [16] Strobel M., Branch M., Ulsh M., Kapaun R. S., Kirk S., Lyons C. S.: Flame surface modification of polypropylene film. *Journal of Adhesion Science and Technology*, **10**, 515–539 (1996).
DOI: [10.1163/156856196X00562](https://doi.org/10.1163/156856196X00562)
- [17] Morra M., Occhiello E., Garbassi F.: Knowledge about polymer surfaces from contact angle measurements. *Advances in Colloid and Interface Science*, **32**, 79–116 (1990).
DOI: [10.1016/0001-8686\(90\)80012-O](https://doi.org/10.1016/0001-8686(90)80012-O)
- [18] Nie H-Y., Walzak M. J., Berno B., McIntyre N. S.: Atomic force microscopy study of polypropylene surfaces treated by UV and ozone exposure: Modification of morphology and adhesion force. *Applied Surface Science*, **144–145**, 627–632 (1999).
DOI: [10.1016/S0169-4332\(98\)00879-4](https://doi.org/10.1016/S0169-4332(98)00879-4)
- [19] Briggs D., Brewis D. M., Konieczko M. B.: X-ray photoelectron spectroscopy studies of polymer surfaces. *Journal of Materials Science*, **14**, 1344–1348 (1979).
DOI: [10.1007/BF00549306](https://doi.org/10.1007/BF00549306)

- [20] Sheng E., Sutherland I., Brewis D. M., Heath R. J.: An X-ray photoelectron spectroscopy study of flame treatment of polypropylene. *Applied Surface Science*, **78**, 249–254 (1994).
DOI: [10.1016/0169-4332\(94\)90012-4](https://doi.org/10.1016/0169-4332(94)90012-4)
- [21] Pijpers A. P., Meier R. J.: Adhesion behaviour of polypropylenes after flame treatment determined by XPS (ESCA) spectral analysis. *Journal of Electron Spectroscopy and Related Phenomena*, **121**, 299–313 (2001).
DOI: [10.1016/S0368-2048\(01\)00341-3](https://doi.org/10.1016/S0368-2048(01)00341-3)
- [22] Strobel M., Walzak M. J., Hill J. M., Lin A., Karbasheski E., Lyons C. S.: A comparison of gas-phase methods of modifying polymer surfaces. *Journal of Adhesion Science and Technology*, **9**, 365–383 (1995).
DOI: [10.1163/156856195X00554](https://doi.org/10.1163/156856195X00554)
- [23] Papirer E., Wu D. Y., Schultz J.: Adhesion of flame-treated polyolefins to styrene butadiene rubber. *Journal of Adhesion Science and Technology*, **7**, 343–362 (1993).
DOI: [10.1163/156856193X00745](https://doi.org/10.1163/156856193X00745)
- [24] Garbassi F., Occhiello E., Polato F., Brown A.: Surface effect of flame treatments on polypropylene. *Journal of Materials Science*, **22**, 1450–1456 (1987).
DOI: [10.1007/BF01233147](https://doi.org/10.1007/BF01233147)
- [25] Farris S., Piergiovanni L.: Emerging coating technologies for food and beverage packaging materials. in ‘Emerging food packaging technologies: Principles and practice’ (eds.: Yam K., Lee D. S.) Woodhead, Oxford, 274–302 (2012).
- [26] Farris S., Pozzoli S., Biagioni P., Duó L., Mancinelli S., Piergiovanni L.: The fundamentals of flame treatment for the surface activation of polyolefin polymers – A review. *Polymer*, **51**, 3591–3605 (2010).
DOI: [10.1016/j.polymer.2010.05.036](https://doi.org/10.1016/j.polymer.2010.05.036)
- [27] Mazzola L., Bemporad E., Carassiti F.: Flame treatment on plastic: A new surface free energy statistical prediction model and characterization of treated surfaces. *Applied Surface Science*, **257**, 2148–2158 (2011).
DOI: [10.1016/j.apsusc.2010.09.064](https://doi.org/10.1016/j.apsusc.2010.09.064)
- [28] Pitts W. M.: The global equivalence ratio concept and the formation mechanisms of carbon monoxide in enclosure fires. *Progress in Energy and Combustion Science*, **21**, 197–237 (1995).
DOI: [10.1016/0360-1285\(95\)00004-2](https://doi.org/10.1016/0360-1285(95)00004-2)
- [29] Dillard J. G., Cromer T. F., Burtoff C. E., Cosentino A. J., Cline R. L., Maciver G. M.: Surface properties and adhesion of flame treated sheet molded composite (SMC). *The Journal of Adhesion*, **26**, 181–198 (1988).
DOI: [10.1080/00218468808071285](https://doi.org/10.1080/00218468808071285)
- [30] Sutherland I., Brewis D. M., Heath R. J., Sheng E.: Modification of polypropylene surfaces by flame treatment. *Surface and Interface Analysis*, **17**, 507–510 (1991).
DOI: [10.1002/sia.740170717](https://doi.org/10.1002/sia.740170717)
- [31] Brewis D. M.: Pretreatments of hydrocarbon and fluorocarbon polymers. *The Journal of Adhesion*, **37**, 97–107 (1992).
DOI: [10.1080/00218469208031253](https://doi.org/10.1080/00218469208031253)
- [32] Owens D. K., Wendt R. C.: Estimation of the surface free energy of polymers. *Journal of Applied Polymer Science*, **13**, 1741–1747 (1969).
DOI: [10.1002/app.1969.070130815](https://doi.org/10.1002/app.1969.070130815)
- [33] Karbowiak T., Debeaufort F., Voilley A.: Importance of surface tension characterization for food, pharmaceutical and packaging products: A review. *Critical Reviews in Food Science and Nutrition*, **46**, 391–407 (2006).
DOI: [10.1080/10408390591000884](https://doi.org/10.1080/10408390591000884)
- [34] Eaton P., West P.: *Atomic force microscopy*. Oxford University Press, Oxford (2010).
- [35] Tuominen M., Ek M., Saloranta P., Toivakka M., Kuusipalo J.: The effect of flame treatment on surface properties and heat sealability of low-density polyethylene coating. *Packaging Technology and Science*, **26**, 201–214 (2013).
DOI: [10.1002/pts.1975](https://doi.org/10.1002/pts.1975)
- [36] Song J., Gunst U., Arlinghaus H. F., Vansco G. J.: Flame treatment of low-density polyethylene: Surface chemistry across the length scales. *Applied Surface Science*, **253**, 9489–9499 (2007).
DOI: [10.1016/j.apsusc.2007.06.018](https://doi.org/10.1016/j.apsusc.2007.06.018)
- [37] Strobel M., Sullivan N., Branch M. C., Jones V., Park J., Ulsh M., Strobel J. M., Lyons C. S.: Gas-phase modeling of impinging flames used for the flame surface modification of polypropylene film. *Journal of Adhesion Science and Technology*, **15**, 1–21 (2001).
DOI: [10.1163/156856101743283](https://doi.org/10.1163/156856101743283)
- [38] Strobel M., Dunatov C., Strobel J. M., Lyons C. S., Perron S. J., Morgen M. C.: Low-molecular-weight materials on corona-treated polypropylene. *Journal of Adhesion Science and Technology*, **3**, 321–335 (1989).
DOI: [10.1163/156856189X00245](https://doi.org/10.1163/156856189X00245)
- [39] Strobel J. M., Strobel M., Lyons C. S., Dunatov C., Perron S. J.: Aging of air-corona-treated polypropylene film. *Journal of Adhesion Science and Technology*, **5**, 119–130 (1991).
DOI: [10.1163/156856191X00080](https://doi.org/10.1163/156856191X00080)
- [40] Cassie A. B. D., Baxter S.: Wettability of porous surfaces. *Transactions of the Faraday Society*, **40**, 546–551 (1944).
DOI: [10.1039/TF9444000546](https://doi.org/10.1039/TF9444000546)
- [41] Beamson G., Briggs D.: *High resolution XPS of organic polymers: The Scienta ESCA300 database*. Wiley, Hoboken (1992).
- [42] Moulder J. F., Stickle W. F., Bomben K. D.: *Handbook of X-ray photoelectron spectroscopy*. Perkin Elmer, Eden Prairie (1992).
- [43] Alexander C. S., Branch M. C., Strobel M., Ulsh M., Sullivan N., Vian T.: Application of ribbon burners to the flame treatment of polypropylene films. *Progress in Energy and Combustion Science*, **34**, 696–713 (2008).
DOI: [10.1016/j.pecs.2008.04.004](https://doi.org/10.1016/j.pecs.2008.04.004)
- [44] Briggs D., Brewis D. M., Konieczko M. B.: X-ray photoelectron spectroscopy studies of polymer surfaces. *Journal of Materials Science*, **11**, 1270–1276 (1976).
DOI: [10.1007/BF00545146](https://doi.org/10.1007/BF00545146)

Gum ghatti based novel electrically conductive biomaterials: A study of conductivity and surface morphology

K. Sharma^{1,3}, B. S. Kaith², V. Kumar³, S. Kalia^{4,5*}, V. Kumar³, S. Som³, H. C. Swart³

¹Department of Chemistry, Shoolini University of Biotechnology and Management Sciences, Solan, 173212 Himachal Pradesh, India

²Department of Chemistry, Dr. B.R. Ambedkar National Institute of Technology, Jalandhar, 144011 Punjab, India

³Department of Physics, University of the Free State, P.O. Box 339, ZA9300 Bloemfontein, South Africa

⁴Department of Civil, Chemical, Environmental and Materials Engineering, University of Bologna, Via Terracini 28, 40131 Bologna, Italy

⁵Department of Chemistry, Bahra University, Shimla Hills, 173 234 Wahnaghat, Dist. Solan (H.P.) India

Received 6 October 2013; accepted in revised form 4 December 2013

Abstract. Gum ghatti-cl-poly(acrylamide-aniline) interpenetrating network (IPN) was synthesized by a two-step aqueous polymerization method, in which aniline monomer was absorbed into the network of gum ghatti-cl-poly(acrylamide) and followed by a polymerization reaction between aniline monomers. Initially, semi-IPN based on acrylamide and gum ghatti was prepared by free-radical copolymerization in aqueous media with optimized process parameters, using *N,N'*-methylene-bis-acrylamide, as cross-linker and ammonium persulfate, as an initiator system. Optimum reaction conditions affording maximum percentage swelling were: solvent [mL] = 12, Acrylamide (AAm) [mol·L⁻¹] = 1.971, Ammonium peroxydisulfate (APS) [mol·L⁻¹] = 0.131·10⁻¹, *N,N'*-methylene-bis-acrylamide (MBA) [mol·L⁻¹] = 0.162·10⁻¹, reaction time [min] = 210, temperature [°C] = 100 and pH = 7.0. The resulting IPN was doped with different protonic acids. The effect of the doping has been investigated on the conductivity and surface morphology of the IPN hydrogel. The maximum conductivity was observed with 1.5N HClO₄ concentration. The morphological, structural and electrical properties of the candidate polymers were studied using scanning electron microscopy (SEM), Fourier transform infrared spectroscopy FTIR and two-probe method, respectively.

Keywords: polymer gels, gum ghatti, interpenetrating network, electrical properties

1. Introduction

Recently, the modifications of crosslinked hydrogels with conducting polymers (CPs) lead to the preparation of multifunctional electrical conducting materials. This offers a facile methodology to combine the superior properties of CPs with the highly crosslinked hydrogels. The resultant hydrogel exhibit quite different characteristics from the individual materials, for example, the electrical conductivity and thermal stability of the resultant hydrogels have much improved over that of bare hydrogel [1, 2].

They also showed good process ability, chemical stability towards dopants and solubility under readily accessible conditions [3]. Conducting hydrogels have been used in fuel cells, super capacitors; dye sensitized solar cells and rechargeable lithium batteries [4]. Many efforts have been made to successfully modify the crosslinked hydrogels with the different materials as polyaniline, graphite, Cu, etc. by a two-step synthesis method [5–8].

On the other hand, superabsorbent hydrogels (SAHs) are three-dimensional (3D) polymer networks that

*Corresponding author, e-mail: susheel.kalia@gmail.com

can absorb water and swell to several times their initial dry volume. The crosslinked hydrogels have outstanding properties such as, hydrophilicity, excellent swelling capacity, lack of toxicity, and biocompatibility which makes them potential candidates to use in a variety of fields [9]. They can respond to slight changes in temperature, pH and light are area of extensive research because of their responsive properties [10]. Hydrogels are particularly useful in agriculture and horticulture, sensors, biomedical and pharmaceutical applications [9, 11, 12].

Gums are important families of natural polymers derived from the seeds or tubers of plants and gum ghatti is a promising polysaccharide [13]. The polysaccharide gums have a different molecular structure and properties, but their common advantages such as renewable, biodegradable, nontoxic, biocompatibility, etc. make them useful in extensive applications as a commercial polymer in many areas [14, 15].

Among the conducting polymers (CPs), polyaniline (PANI) is a well-known versatile conducting material, which has found particular biological utility due to its easy synthesis, low cost, tunable conductivity, and environmental stability [16, 17]. The conductivity of PANI can be controlled by the protonation of the imine sites on the main polymer chain. It is well reported in literature that the electrical conductivity of PANI depends mainly on the dopant concentration, oxidant-to-monomer ratio, the rate of addition of oxidants, the nature of dopants, purity of monomer and polymerization time, etc. [18–20]. Crosslinked hydrogels based on gum ghatti were studied to determine their absorbency and biodegradability [21, 22]. Various authors synthesized electrical conducting hydrogels based on different polysaccharides and polyaniline through graft copolymerization [23–26]. The produced materials have found applications in the area of biosensors and gas sensors [3, 25]. The present work reports on the synthe-

sis of electrical conducting IPN biopolymer based on Gg-cl-poly(AAm) and PANI in hot air oven. Initially, a semi-IPN based on AAm and gum ghatti has been synthesized using free radical copolymerization with optimized process parameters (viz. concentration of monomer, solvent and crosslinker, reaction time, pH of solution, etc.). The synthesis of IPN hydrogel consisting of poly(acrylamide-aniline)-grafted gum is also reported. The effects of protonic acid dopants on the conductivity and surface morphology of the IPN hydrogel were investigated. This study has been extended to the examination of the synthesized crosslinked hydrogels for their thermal stability. The main advantage of present work is to explore the use of natural resources and increase their usefulness in broader prospective by chemical modifications.

2. Experimental section

2.1. Materials

Gum ghatti (G_g) was purchased from Sigma Aldrich. Ammonium peroxydisulfate (APS) (99.5%), *N,N'*-methylene-bis-acrylamide (MBA), aniline (99.5%) and all the protonic acids (>99% purity) were purchased from Merck India Co. Deionized water was used for all reactions.

2.2. Preparation of Gg-cl-poly(AAm)

A polymer matrix composed of Gg-cl-poly(AAm) was prepared by using MBA as crosslinker and APS as initiator in hot air oven. In a typical experiment, 0.5 g gum ghatti was dissolved in 10 mL of triple distilled water in a reaction flask. To this reaction mixture, a calculated amount of APS and MBA were added followed by the addition of AAm under continuous stirring. The reaction container was kept in a hot air oven at 60°C for a fixed time period and the resulting product was freed from homopolymer through solvent extraction using acetone. Finally, the product was dried in a hot air oven at 50°C. Var-

Table 1. Effect of different reaction parameters on Gg-cl-poly(AAm) and Gg-cl-poly(AAm-ipn-aniline)

Sample code	Optimized reaction parameters								Mean percentage swelling (M)	±SD	±SE
	Back-bone [g]	Initiator [mol/L] ·10 ⁻¹	Time [min]	Amt. of solvent [mL]	pH	Monomer [mol/L]	Cross-linker [mol/L] ·10 ⁻¹	Temperature [°C]			
Gg-cl-poly(AAm)	0.5	0.131	210	12	7	1.971	0.162	60	850.43	24.36	14.01
Gg-cl-poly(AAm-ipn-aniline)	0.5	0.131	210	12	7	2.219·10 ⁻⁴	0.162	60	686.30	12.50	7.20

Where, number of replication = 3, M – mean, ±SD – standard deviation and ±SE – standard error of mean.

ious reaction parameters such as monomer concentration, initiator concentration, cross linker concentration, polymerization time, temperature, solvent and pH of the reaction mixture were optimized to get the maximum percentage swelling (P_s) (Table 1).

2.3. Preparation of

Gg-cl-poly(AAm-ipn-aniline)

On the basis of the Gg-cl-poly(AAm) superabsorbent, a Gg-cl-poly(AAm-ipn-aniline) hydrogel was prepared according to the following procedure. For each experiment Gg-cl-poly(AAm) (0.5 g) was added to an aqueous medium with $2.129 \text{ mol}\cdot\text{L}^{-1}$ of aniline monomer. The resulting solution was kept for 16 h at room temperature, which resulted in the absorption of aniline monomer in the Gg-cl-poly(AAm) network and the formation of a swollen sample. To this mixture a preoptimized initiator ($0.131\cdot 10^{-1} \text{ mol}\cdot\text{L}^{-1}$) and crosslinker concentration ($0.162\cdot 10^{-1} \text{ mol}\cdot\text{L}^{-1}$) was added during constant stirring. When a small amount of APS solution was added slowly into the solution at the polymerization step, the slightly brown color of the reaction solution changed to slightly green. The resulting solution was kept in hot air oven at 60°C for a preoptimized time period (210 min). The resulting product was washed with 1-methyl-2-pyrrolidone (NMP) to remove the homopolymers. Finally, the product was dried in a vacuum oven at 50°C and a solid Gg-cl-poly(AAm-aniline) IPN structure was obtained. Optimization was done with respect to aniline concentration (Table 1). The synthesis of the conducting IPN was carried out in a similar fashion containing 0.5N aqueous acidic media of protonic acids such as H_2SO_4 , HCl, HClO_4 , PTS or HNO_3 in the reaction flask, respectively. The conducting IPN was also synthesized at various concentrations of HClO_4 varying from 0.5–2.5N, respectively.

2.4. Characterizations

X-ray diffraction (XRD) patterns were recorded on a Phillips X-ray diffractometer with Cu-K_α radiation (1.54 \AA) for a wide range of Bragg's angles 2θ ($10 < \theta < 60$) at the scanning rate of 1° per minute. The operating voltage and current for the X-ray gun were 40 kV and 40 mA, respectively. Fourier transformed infrared (FTIR) spectral studies of raw and cross linked samples were recorded using a Perkin Elmer FTIR spectrophotometer using KBr pellets. The analysis conditions were: wavenumber range

of $600\text{--}4000 \text{ cm}^{-1}$, 4 cm^{-1} resolution, 40 scans, and room temperature (25°C). Thermal gravimetric analysis (TGA) spectra were taken by using a Perkin Elmer Diamond instrument in air at a heating rate of $10^\circ\text{C}/\text{min}$. A Shimadzu SSX-550 Superscan scanning electron microscope (SEM) was used to capture the SEM images at different magnification. Room-temperature d.c. electrical conductivity was measured by the two-probe technique using a Keithley 2400 source meter. The electrical conductivity measurements were made on compressed circular pellets (mass $\sim 0.2 \text{ g}$, diameter = 8 mm, thickness = $1\pm 0.07 \text{ mm}$, pressure = $8 \text{ t}/\text{cm}^2$). The resistivity of the sample was calculated using the Equation (1) [26]:

$$\rho = R \frac{A}{l} \quad (1)$$

where ρ , R , A , and l are resistivity [$\Omega\cdot\text{cm}$], resistance [Ω], area of the pellet [cm^2], length of the pellet [cm], respectively.

Conductivity can be computed using the relationship, $\sigma = 1/\rho$, where σ is the conductivity, and ρ the resistivity of the sample.

2.5. Swelling behavior

The pre-weighted crosslinked hydrogel was immersed in excessive distilled water and kept undisturbed for 16 h at room temperature. The swollen hydrogel was dried with filter paper and drained for some time until no free water remained. After weighing the swollen hydrogel on an analytical balance (accuracy $\pm 0.00001 \text{ g}$), the percentage swelling (P_s) may be calculated by using the Equation (2) [27]:

$$P_s = \frac{W_s - W_d}{W_d} \cdot 100 \quad (2)$$

where W_s is the weight of swollen polymer and W_d is the weight of dry polymer.

3. Results and discussions

3.1. Mechanism of hydrogels formation

Polyacrylamide grafted gum ghatti was synthesized in a hot air oven at 60°C . APS is a thermal initiator and decomposed under heat leads to the formation of sulphate ion radicals (Figure 1). The sulphate ion radical formed from homolytic cleavage of initiator reacts with water and gives rise to hydroxyl free radical [28]. The free radicals also generated on the polar $-\text{OH}$ groups of the gum ghatti backbone. The

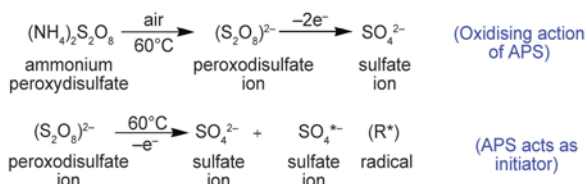


Figure 1. Generation of primary radicals under heat

monomer molecules, which are in close vicinity of the reaction sites, become acceptor of gum ghatti radicals resulting in the chain initiation and thereafter themselves become a free radical donor to neighboring molecules [29, 30]. During chain propagation crosslinker end groups may react with the polymer chain. The copolymer formed in this way

consisted of a crosslinked structure [30]. Various authors reported free radical copolymerization of vinyl monomers with carbohydrate polymers using peroxydisulfate, a chain mechanism is involved due to the formation of sulphate ion radicals, which are well known ion chain carriers for the graft copolymerization [26, 31–33].

The semi-IPN network will serve effectively as a medium for the graft copolymerization of aniline monomer in the presence of the MBA and APS as a crosslinker initiator system. At the same time peroxydisulfate stimulus the oxidative polymerization reaction of aniline via a medium of cationic radicals and form PANI and PANI radicals (Figure 2) [31,

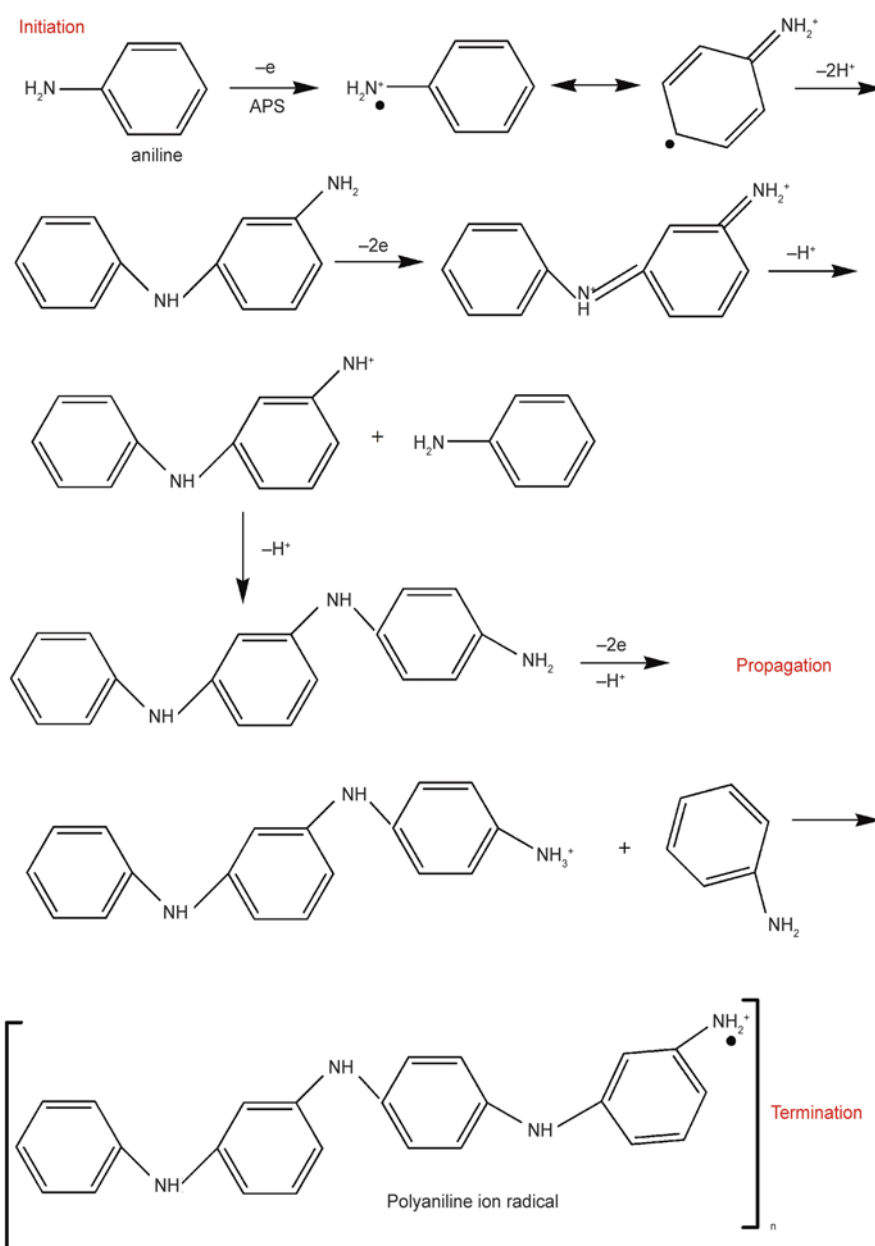


Figure 2. Formation of polyaniline ion radicals under heat

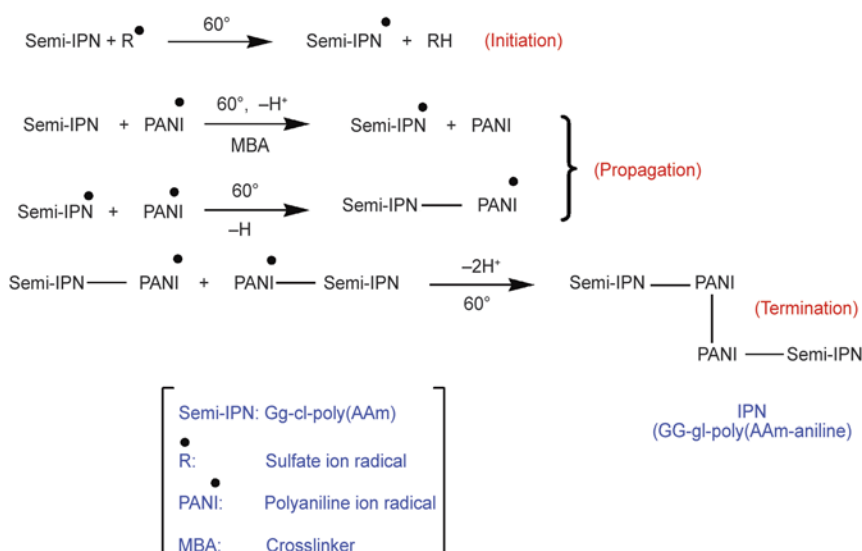


Figure 3. Formation of conducting Gg-cl-poly(AAm-ipn-aniline)

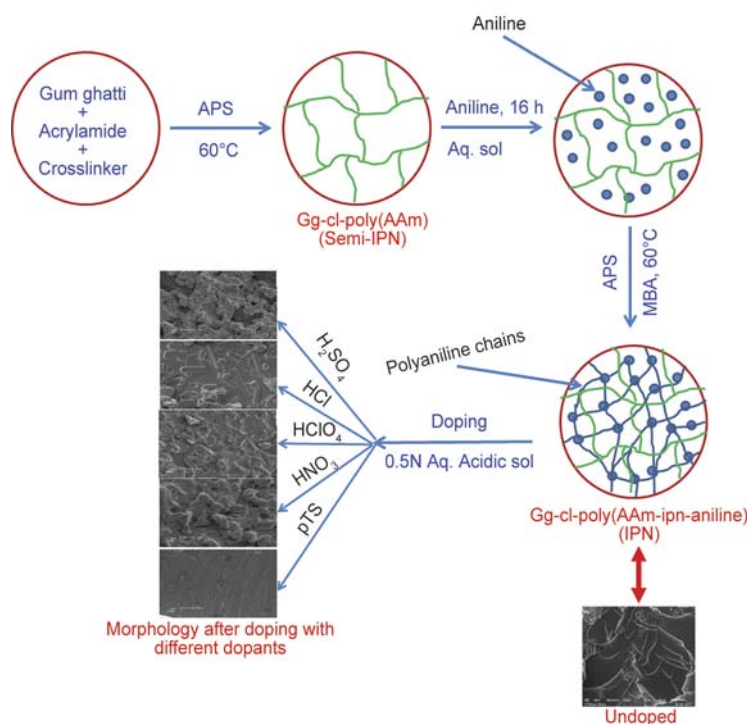


Figure 4. Schematic representation of preparation of Gg-cl-poly(AAm-ipn-aniline) hydrogels

34]. When a fully swollen semi-IPN is put in the aqueous aniline solution for 16 h, there occurs a form of loosely bound network between the semi-IPN and aniline monomer. Finally Semi-IPN radical and PANI cation radicals are combined to form Gg-cl-poly(AAm-ipn-aniline) graft copolymer. Sulfate ion is the primary radicals, generated from the APS by the reduction of one electron as shown in Figure 1. Simultaneously, APS generated sulfate ion radical by the reduction of two electrons and act

as oxidant. They initiate the oxidative polymerization of aniline. The macro radical semi-ipn* may be generated by the abstraction of H by the growing PANI ion radical in the acidic medium, which may add onto the semi-ipn macro radicals generating new radical semi-IPN* and these chains will be grow and combined with other semi-IPN* chains to give a graft copolymer (Figure 3) [26, 31]. Preparation of Gg-cl-poly(AAm-ipn-aniline) conducting hydrogel is schematically displayed in Figure 4.

3.2. Optimization of different reaction parameters for the synthesis of semi-IPN [Gg-cl-poly(AAm)]

In order to get the crosslinked hydrogel with maximum swelling capacity, the different reaction parameters such as initiator, crosslinker and monomer concentration, reaction time, amount of solvent, pH and reaction temperature were optimized (Figure 5). It was observed that the APS/MBA system could effectively be used to crosslink AAm onto Gum ghatti and maximum percentage swelling (857%) was observed with APS, AAm and MBA concentration of $0.131 \cdot 10^{-1}$, 1.971 and $0.162 \cdot 10^{-1} \text{ mol} \cdot \text{L}^{-1}$, respectively. The optimized reaction time was found to be 210 minutes.

Here it is observed that an increase in the concentration of the initiator led to a decrease in the swelling of the superabsorbent (Figure 5a). This is due to the fact that the increase in initiator concentration resulting in an increased number of free radicals led to a terminating step by initiating a bimolecular collision [35] and decreasing molecular weight of the

candidate superabsorbent [36], so both results in shortening of the polymer chains and reducing the available free volumes within the hydrogel.

Reaction time was found to possess an important role in getting the synthesized samples with higher water absorbency. However, after attaining the optimum reaction time further increment resulted in a decreased percentage swelling (Figure 5b), which again could be due to excessive crosslinking resulting in more compactness and rigidity [37].

Other optimized parameters such as reaction solvent, pH and temperature were found to be 12 mL, 7.0 and 60°C respectively (Figure 5c–5e). In the case of the reaction medium different controlling phenomenon was found to play an important role in deciding the reaction volume dependent swelling of the synthesized samples. The maximum swelling of crosslinked superabsorbent was observed with a 12 mL solvent (Figure 5c). However, further increase in the amount of solvent results in increasing concentrations of hydroxyl radicals which finally leads to the termination of the chains. Since the absorbency

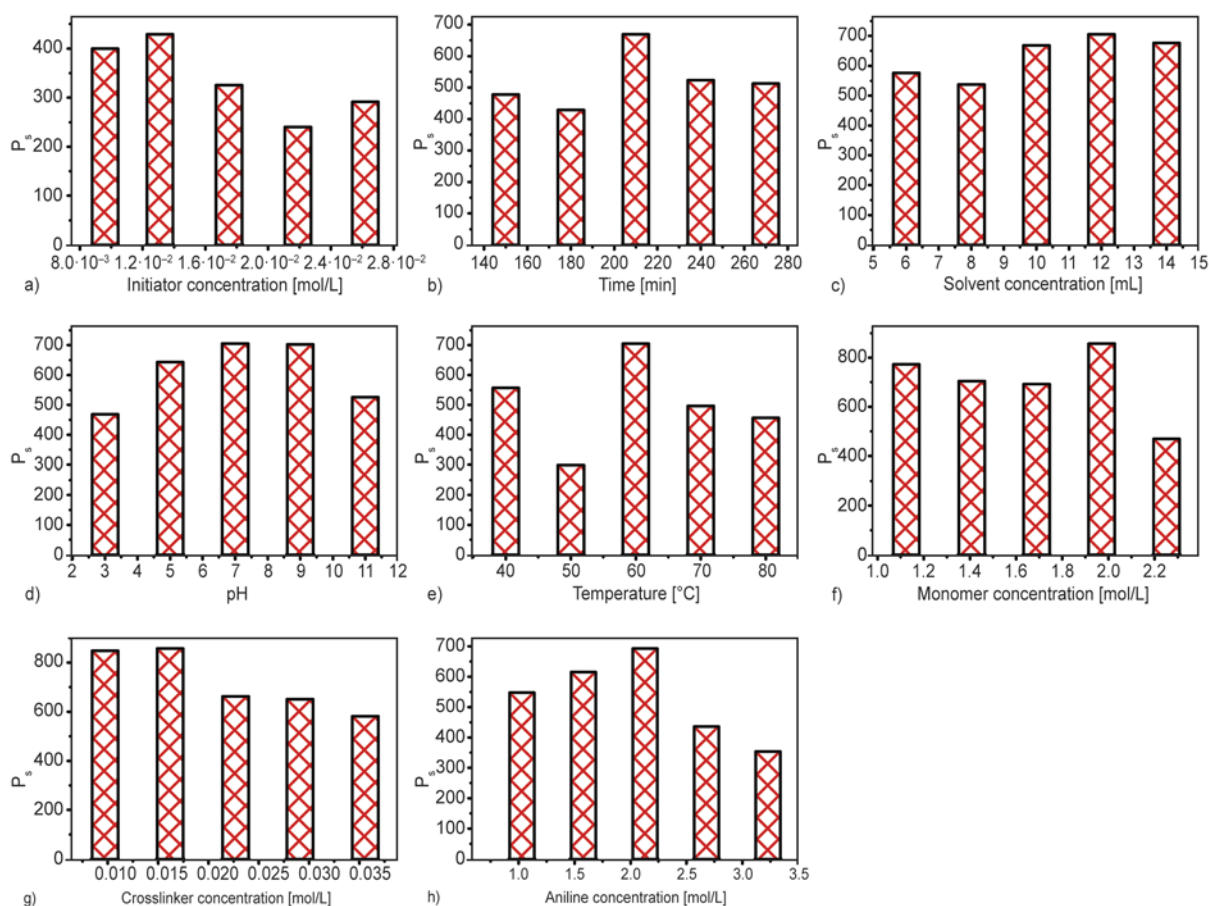


Figure 5. Variation of percentage swelling with (a) initiator concentration, (b) reaction time, (c) solvent concentration, (d) pH, (e) temperature, (f) monomer concentration, (g) amount of crosslinker, and (h) amount of aniline

of the superabsorbent is strongly influenced by the ionic strength therefore, no additional ions were added to the medium (through buffer solution) for setting the pH. The equilibrium swelling was studied for pH from 3.0 to 11.0 using NaOH stock solution (Figure 5d). Maximum P_s (857%) was observed in the neutral medium whereas, a lesser P_s was found in acidic as well as in the alkaline media. The minimum swelling occurred in the hydrogel prepared in the highly acidic medium having a pH of 3 to 5. Which might be due to the fact that the NH_2 groups of acrylamide being present along the macromolecular chains in the hydrogel remained almost unionized [38], thus resulting in almost nil osmotic swelling pressure inside the hydrogel [39]. It was observed that hydrogel prepared in neutral a medium showed maximum swelling because the degree of protonation in acrylamide increased and NH_2 ions get converted to NH_3^+ ions that resulted in a more hydrophilic polymer network and contributed to the higher water uptake [40]. When the pH was changed to basic, dissociation of $-\text{NH}_2$ group is almost complete but a very high concentration of Na^+ and OH^- ions lead to the reduction of P_s . The highest concentration of Na^+ ions acted as a screening bar hence a lesser P_s was observed [41] (Figure 5d).

It has been observed that the water absorbency of the hydrogels increased significantly with increasing the reaction temperature from 40 to 60°C (Figure 5e). Furthermore, an increase in the reaction temperature lead to degradation of the carbon chain by sulphate radicals generated due to the decomposition of APS. The decomposition of APS also gave O_2 radical scavenger which reacted with free radicals which lead to less hydrogel formation [42]. Additionally high temperature also leads to the fastest chain termination and chain transfer reactions.

Similarly with the increase in AAm concentration beyond the optimum level gave rise to favored homopolymerization over graft copolymerization and also caused the self-cross-linking phenomenon [35] and cross-linker concentration though gave rise to a medium stable product but increased crosslinking resulted in a rigid and compact structure with decreased swelling capacity [36] (Figure 5f). Cross-linker could prevent the dissolution of hydrophilic polymer chains in aqueous medium and increased the dimensional stability. Therefore, the significance of the optimization was to get the synthesized product

with maximum water absorbance capacity along with good dimensional stability.

Semi-IPN with a varying amount of crosslinker in the $0.0972 \cdot 10^{-1}$ to $0.356 \cdot 10^{-1} \text{ mol} \cdot \text{L}^{-1}$ ranges were synthesized and swelling capacity in distilled water was investigated. The results, as shown in the Figure 5g, indicate that as the concentration of crosslinker increases from $0.0972 \cdot 10^{-1}$ to $0.162 \cdot 10^{-1} \text{ mol} \cdot \text{L}^{-1}$, the swelling capacity of the resulting hydrogel increased. However, a further increase in the crosslinker concentration decreased the swelling capacity. The higher concentration of crosslinker resulted in the enhancement in degree of crosslinking which in terms decreased in flexibility of the macromolecular chains [43]. This hindered the chain relaxation process, thus causing a decrease in the swelling capacity. This behavior can also be explained in terms of the reduction in gelation time with the increase in the crosslinker concentration. At higher crosslinker concentration, the gelation time was so short that bubbles formation did not occur in the proper manner, due to an increase viscosity of the gelation medium. In this way the extent of porosity decreased in the resulting hydrogel which lead to the lowering of swelling capacity.

After the optimization of different reaction parameters for the formation of semi-IPN in the hot air oven, the replications carried-out for the reproducibility of the results were in triplicates and the statistics of the results obtained was performed using the Statistical Package for Social Science (SPSS) version 10. Statistical results of the optimum percent grafting and percent swelling are depicted in Table 1.

3.3. Optimization of aniline concentration for the synthesis of Gg-cl-poly(AAm-ipn-PANI)

The effect of the aniline concentration was studied at different concentrations keeping other influential factors constant. It has been observed that with initial increases in aniline concentration, there was an increase in percentage swelling. However, after reaching the maxima, further increase in aniline concentration resulted in decreased swelling capacity of the synthesized sample (Figure 5h). This could be due to the more compactness, decreased pore size and formation of PANI homopolymer, giving rise to decreased water absorbency [31].

3.4. FTIR spectroscopy

The crosslinking was determined on the basis of IR spectrum of gum ghatti, Gg-cl-poly(AAm) and Gg-cl-poly(AAm-aniline) (Figure 6). The gum ghatti showed broad peaks at 3434 and 1032 cm^{-1} , characteristics of the saccharide structure (due to $-\text{OH}$ stretching) [44]. The peaks at 2925 and 1622 cm^{-1} was assigned to the stretching vibration of the $-\text{CH}$ group and $-\text{C}=\text{O}$ stretching of a carbonyl group respectively [30]. Another characteristic peak of the acid group was found at 1422 cm^{-1} due to $-\text{OH}$ bending. After gum ghatti had been grafted copolymerized with acrylamide, broad peaks were observed at 1658 and 1456 cm^{-1} contributing to the $\text{C}=\text{O}$ stretching of amide I band and $-\text{NH}$ in plane bending of amide II respectively [21, 22]. Interestingly, the peaks after grafting shifted to a higher wavenumber region indicating the formation of crosslinked hydrogel. On the other hand FTIR spectrum of Gg-cl-poly(AAm-ipn-aniline) illustrated the characteristics peaks of PANI, as well as Gg-cl-poly(AAm)

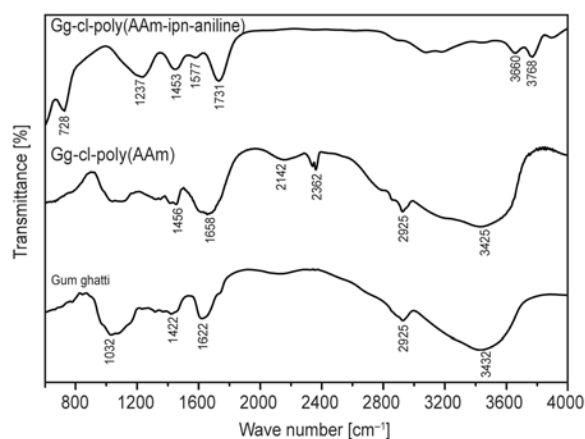


Figure 6. FTIR spectra of (a) Gum ghatti, (b) Gg-cl-poly(AAm) and (c) Gg-cl-poly(AAm-ipn-aniline)

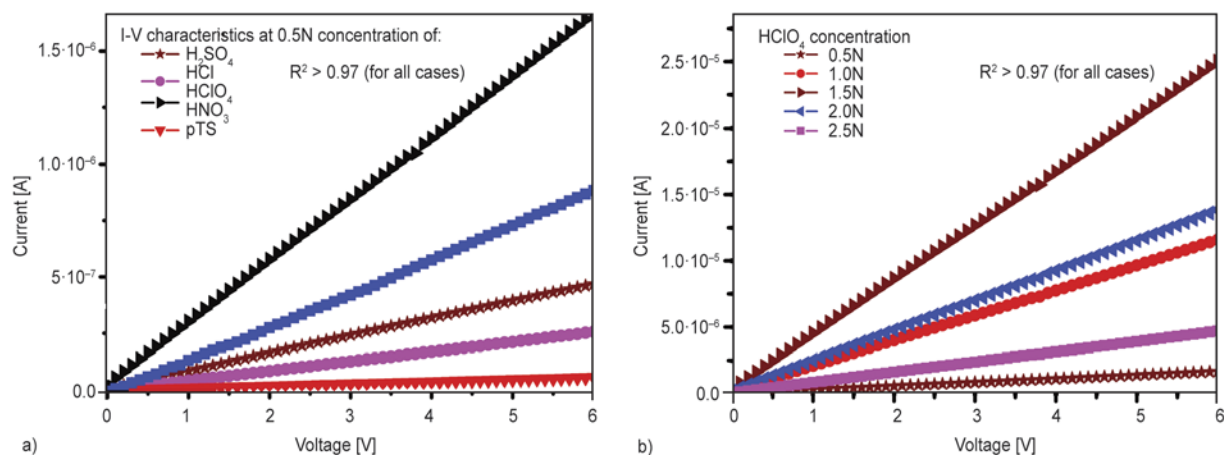


Figure 7. Current-voltage plots for IPN hydrogel with (a) different dopants and (b) as a function of perchloric acid concentration

[30, 45]. The bands at 1496 and 1574 cm^{-1} represent the benzoid and quinoid ring vibration of PANI, respectively. Conducting form of PANI is described by band at 1237 cm^{-1} [10, 46]. The bands at 796 and 1731 cm^{-1} were corresponding to an out-of-plane bending vibration of $\text{C}-\text{H}$ on para-disubstituted rings and carboxyl groups, respectively [10, 47, 48]. It has been reported that the band at 1110 cm^{-1} to be a measure of the degree of the delocalization of electrons and is also revealing of high conductivity. The shifting and formation of new bands (728, 3660 and 3768 cm^{-1}) supported the formation Gg-cl-poly(AAm-aniline) hydrogel. Thus, it is quite evident from FTIR studies that grafted chains of AAm and aniline got grafted onto gum ghatti.

3.5. Current-voltage characteristics

The current-voltage (I-V) curve of the IPN samples at room temperature was measured using a two-probe method. The I-V relationships of the IPN sample with 0.5N concentrations of each dopant are shown in Figure 7a, which shows an ohmic behavior. The nature of the dopants significantly influenced the conductivity. The differences in I-V characteristics were due to the effect of the dopant ions. It was found that HClO_4 doped IPN showed a maximum current, which pointed to the maximum conductivity (Table 2). Various authors reported the synthesis of PANI by using different dopants and its characterization [49, 50]. Kulkarni *et al.* [51] synthesized PANI by chemical polymerization using different inorganic acids, such as HCl , H_2SO_4 , HClO_4 , and HNO_3 , as protonic acid media. They have reported a maximum conductivity for HClO_4 doped PANI sample.

Table 2. Room-temperature conductivities of IPN hydrogel doped with different acids

Hydrogels	Conductivity [S/cm]
Gg-cl-poly(AAm-ipn-aniline)-H ₂ SO ₄	0.15·10 ⁻⁷
Gg-cl-poly(AAm-ipn-aniline)-HCl	0.80·10 ⁻⁷
Gg-cl-poly(AAm-ipn-aniline)-HClO ₄	0.50·10 ⁻⁶
Gg-cl-poly(AAm-ipn-aniline)-HNO ₃	0.10·10 ⁻⁸
Gg-cl-poly(AAm-ipn-aniline)-pTS	0.20·10 ⁻⁷

Taking this into account the IPN samples were further doped with different concentration of HClO₄ varying from 0.5–2.5N (Figure 7b). The improvement in the electrical conductivity with increasing HClO₄ concentration was due to increasing the degree of protonation of the imine group of PANI in the IPN. However, a decrease in electrical conductivity occurred at higher HClO₄ concentrations (2.0–2.5N). This may be probably due to the over protonation of PANI chains causing a decrease in the delocalization length of PANI and hindrance in the amount of the electrons between the valence band and the conduction band. The maximum conductivity was observed at a 1.5N HClO₄ concentration. Various authors reported the synthesis of conducting hydrogels with different materials [3, 5–7, 52].

3.6. Surface morphology

The surface morphology of the gum ghatti and its amalgamated structures are shown in (Figure 8) in three states the native, cross linked and layered/hybrid with polyaniline (undoped). The pure gum ghatti showed a smooth surface as shown in Figure 8a–8b. The film is also covered with white spots uniformly distributed over the whole surface [29, 30]. After the cross linking of gum ghatti with poly(AAm), the structural morphology gets changed and resembles an whisker like morphology with a rough agglomerated surface (Figure 8c–8d). These figures display the favorable cross linking network between gum ghatti and poly(AAm). Gg-cl-poly(AAm-ipn-aniline) hydrogel form a heterogeneous network type structure, as shown in Figure 8e–8f. The three micrographs and their magnified images clearly show the variation in chemical structures and change in surface morphology in the cross linked networks. Figure 9 shows SEM micrographs of Gg-cl-poly(AAm-ipn-aniline) doped with H₂SO₄, HCl, HClO₄, HNO₃ and pTS. The morphology of the IPN samples was changed based on the type of acid used to dope. As shown in the SEM images of Figure 9,

IPN samples with varying dopants exhibit varying microstructures. It was observed that the type of dopants has considerable influence on the properties-in particular, electrical and morphological features of the resulting IPN hydrogel. Each acid produced characteristic morphology. It is well documented that the incorporation of dopant ions modifies the polymer lattice, which leads to the ionization of sites in the chains which in terms creates defects in the chain [53]. The formation of defects due to the dopant ions provide the mobility of the charge carriers on which conduction depends. Moreover, the conductivity is also dependent on the number of charge carriers. The morphological studies reveal some interesting features as a function of protonic acid used during synthesis.

Figure 9a–9b shows the H₂SO₄ doped IPN showing agglomerated particles type morphology with different shapes and noticeable pores which can be useful for chemical sensing applications. The HCl-doped sample has flat-faced particles of varied shapes and sizes (Figure 9c–9d); the HClO₄ doped sample (Figure 9e–9f) has a rough surface with noticeable pores. Figure 9g–9h shows the loose flaky structures of the HNO₃-doped IPN hydrogel. Lastly, Figure 9i–9j shows the rough surface of the pTS doped sample. The low conductivity of the HNO₃-doped sample may be due to these loose flaky structures and presence of air space. Thus, SEM analysis reveals the variation in the surface morphologies of the undoped and doped IPN hydrogel. Finally, it can be concluded that the surface morphology and the conductivity of the resulting IPN hydrogel can be tuned by varying the types of dopant.

3.7. X-ray diffraction studies

XRD patterns of the samples are characterized by halos extending in the 2θ range 10–60°. XRD pattern of gum ghatti showed that the gum ghatti is partly crystalline with a dominant amorphous phase while on poly(AAm) grafting, the graft copolymer acquires more amorphous area (Figure 10). Change in the XRD pattern confirms the grafting. In the graft copolymer the decrease in the diffraction intensity and an increase in the broadness was due to the presence of poly(AAm) grafts at gum ghatti, which was also confirmed by changes in the surface morphology as seen from SEM micrographs (Figure 8a–8f). Gum ghatti showed peaks at 19.740 and 360 with relative intensities of 462 and 257, respectively.

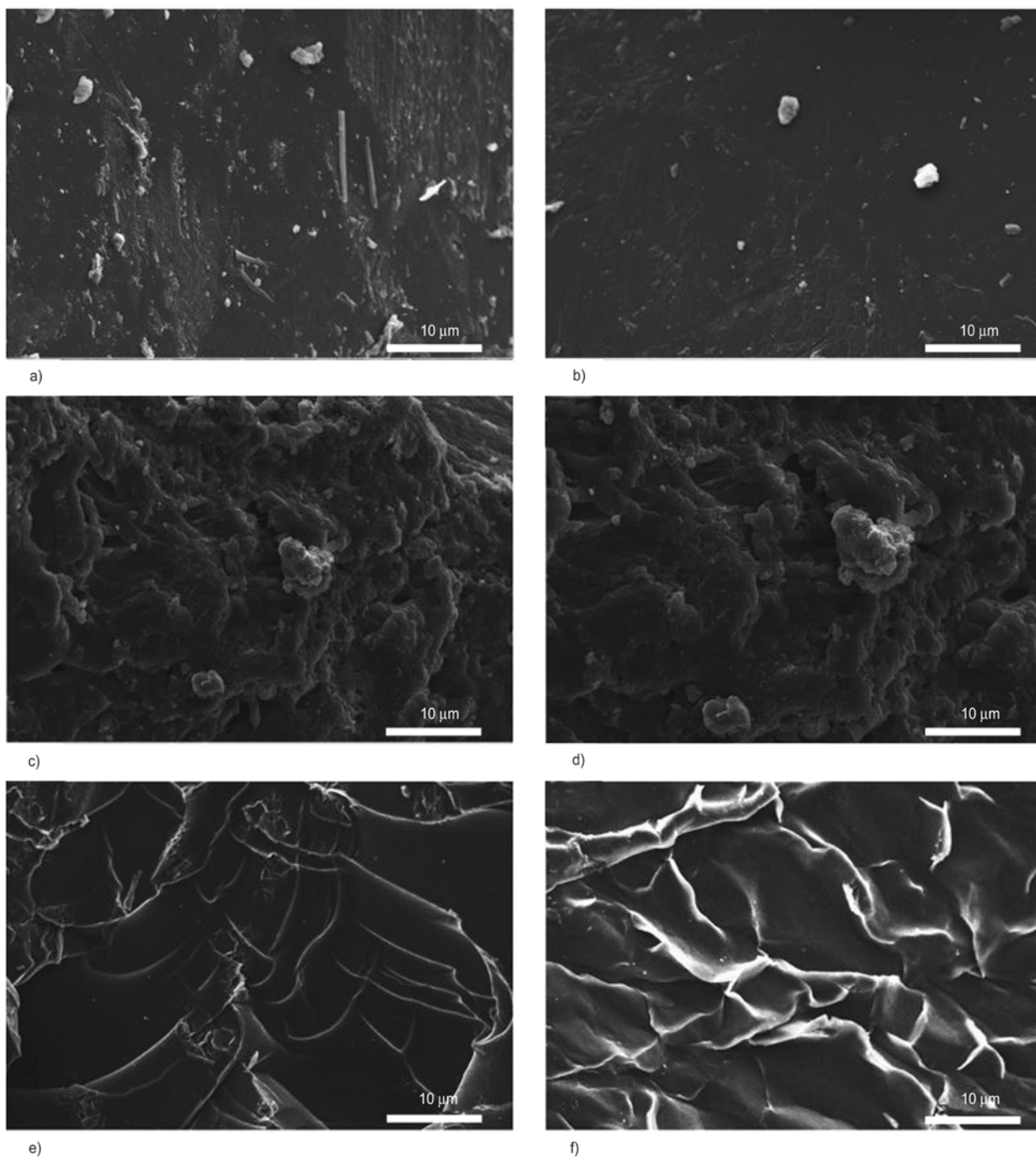


Figure 8. Scanning electron micrographs of (a–b) Gum ghatti, (c–d) Gg-cl-poly(AAm), and (e–f) undoped Gg-cl-poly(AAm-ipn-aniline)

However, Gg-cl-poly(AAm) showed peaks at 22 and 35.4° with relative intensities of 289 and 150, respectively. It is interesting to note that the intensity of the diffraction peaks increased with a cross linked network on moving from Gg-cl-poly (AAm) to Gg-cl-poly (AAm-ipn-aniline), which indicated the enhancement in crystallinity [30, 44]. This enhancement in crystallinity could be attributed to the interaction of PANI chains in the crosslinked

network of Gg-cl-poly(AAm) [54]. The PANI chains crosslinked with each other during the polymerization process to form a network structure [30]. This phenomenon relates the changes in the surface morphology revealed by SEM images. Thus, the XRD patterns of the crosslinked hydrogels provide an additional evidence of AAm and PANI crosslinking onto gum ghatti.

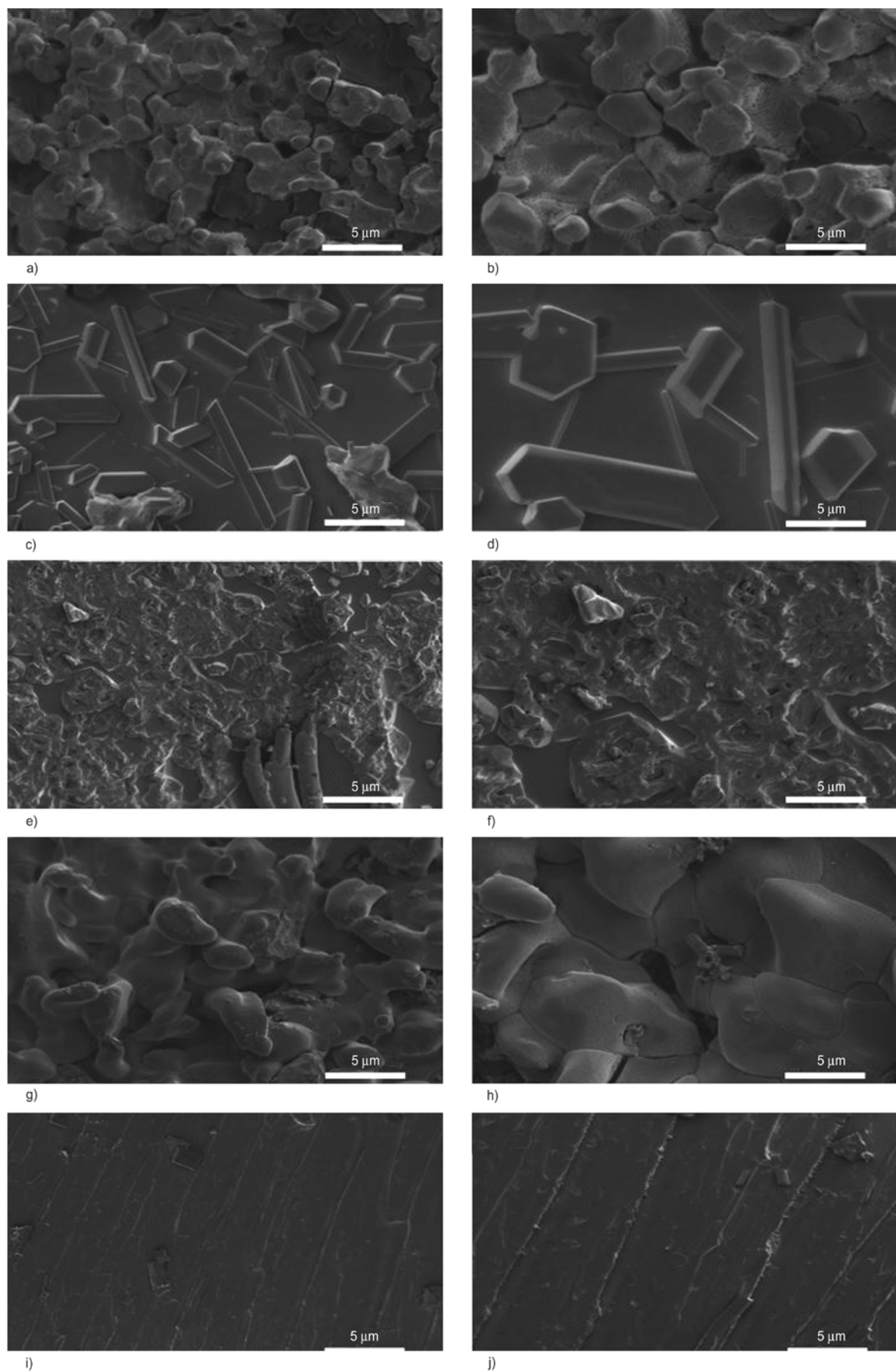


Figure 9. Scanning electron micrographs of IPN samples doped with (a–b) H_2SO_4 , (c–d) HCl , (e–f) HClO_4 , (g–h) HNO_3 and (i–j) pTS

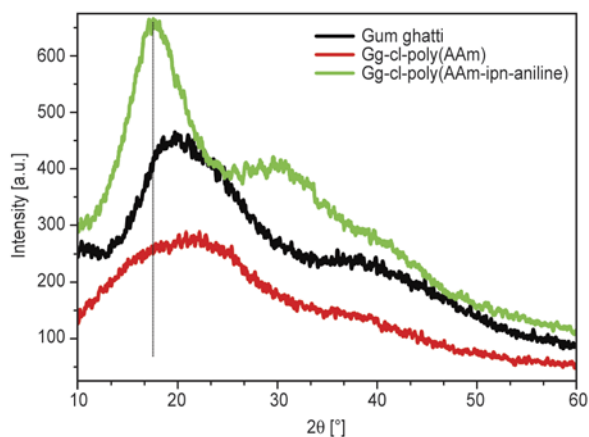


Figure 10. XRD patterns of the Gum ghatti, Gg-cl-poly(AAm) and Gg-cl-poly(AAm-ipn-aniline)

3.8. Thermal analysis

The effect of crosslinking of poly(AAm) and poly(AAm-aniline) on the thermal stability of *gum ghatti* was studied with the help of the thermogravimetric technique (Figure 11). Grafting is clear from the TGA that the Gg-cl-poly(AAm-ipn-aniline) has more thermal stability than the gum ghatti and Gg-cl-poly(AAm) both [26]. The percent of weight losses at the selected temperatures are listed in Table 3. TGA of G_g showed two-stage decomposition. G_g exhibited initial decomposition temperature (IDT) at 207°C and final decomposition temperature (FDT) at 534°C [44]. Whereas, Gg-cl-poly(AAm) showed

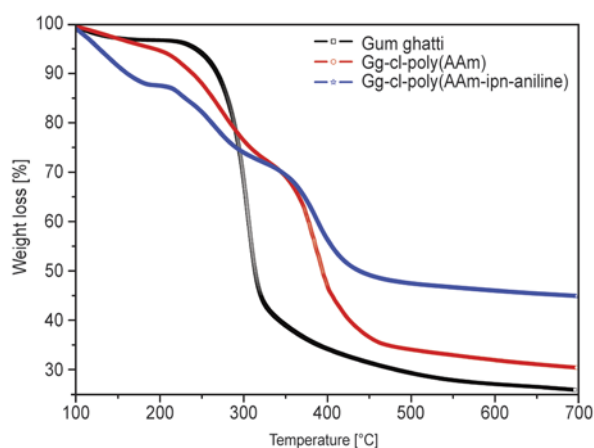


Figure 11. TGA spectra of Gum ghatti, Gg-cl-poly(AAm) and Gg-cl-poly(AAm-ipn-aniline)

Table 3. Details of % weight loss at different temperatures

Sample name	IDT [°C]	FDT [°C]	Weight loss [%] at different temperature						
			250°C	300°C	350°C	400°C	450°C	500°C	600°C
G_g	207	534	5.8	32.3	61.2	65.8	69.7	70.7	73
Gg-cl-poly(AAm)	190	578	12.0	23.7	30.7	53.3	63.2	66.0	68
Gg-cl-poly(AAm-ipn-aniline)	100	600	18.0	26.0	30.7	43.7	51.0	52.7	54

IDT at 190°C and FDT was at 578°C. It was found that the IDT of G_g was higher whereas, the FDT was lower than that of Gg-cl-poly(AAm). The TGA spectrum of IPN shows three-step degradation. The first step degradation was due to the loss of moisture or water content, which ends at 180°C [55]. The second weight (28%) loss at temperature between 211 and 320°C is believed to be due to the elimination of some low molecules or due to dopant evolution. The third stage decomposition started at about 340°C is assigned to the breakdown of the IPN structure. Thus, it is clear from the thermo gravimetric analysis studies that the synthesized IPN was found to possess higher thermal stability with higher decomposition temperature in comparison to gum ghatti and semi-IPN Gg-cl-poly(AAm). Thus, good thermal stability coupled with high electrical conductivity is the most significant advantage of dopants for the synthesis of conducting IPN hydrogels. This enhanced thermal stability of the grafted hydrogel networks might be due to the formation of crosslinks between different polymeric chains through covalent bonding.

4. Conclusions

In summary we have investigated the effects of dopants on the surface morphologies and electrical conductivity of the IPN hydrogels. It was found that the surface morphology and electrical conductivity strongly depended on the type of dopants. These results indicate that the present work may open a new way to synthesize IPN structures with different surface morphologies and conductivities. Further, thermogravimetric analysis showed good thermal stability for the IPN hydrogel. The hydrogels based on biodegradable natural gum ghatti significantly improved the swelling capacity, which can be used as promising water holding materials for agricultural and biomedical applications. Further studies in the direction of controlled drug delivery of cross-linked hydrogels are under progress in order to extend the application of these hydrogels in biomedical applications.

Acknowledgements

The research is supported by the South African Research Chairs Initiative of the Department of Science and Technology and National Research Foundation of South Africa. The University of the Free State Cluster program for financial support. Authors are also thankful to department of Chemistry, University of the Free State for providing TGA spectra.

References

- [1] Fan S., Tang Q., Wu J., Hu D., Lin J.: Two-step synthesis of polyacrylamide/poly(vinyl alcohol)/polyacrylamide/graphite interpenetrating network hydrogel and its swelling, conducting and mechanical properties. *Journal of Materials Science*, **43**, 5898–5904 (2008). DOI: [10.1007/s10853-008-2855-z](https://doi.org/10.1007/s10853-008-2855-z)
- [2] Pissis P., Kyritsis A.: Electrical conductivity studies in hydrogels. *Solid State Ionics*, **97**, 105–113 (1997). DOI: [10.1016/S0167-2738\(97\)00074-X](https://doi.org/10.1016/S0167-2738(97)00074-X)
- [3] Tiwari A.: Synthesis and characterization of pH switching electrical conducting biopolymer hybrids for sensor applications. *Journal of Polymer Research*, **15**, 337–342 (2008). DOI: [10.1007/s10965-008-9176-4](https://doi.org/10.1007/s10965-008-9176-4)
- [4] Sun X-G., Liu G., Xie J., Han Y., Kerr J. B.: New gel polyelectrolytes for rechargeable lithium batteries. *Solid State Ionics*, **175**, 713–716 (2004). DOI: [10.1016/j.ssi.2003.11.043](https://doi.org/10.1016/j.ssi.2003.11.043)
- [5] Lin J., Tang Q., Wu J.: The synthesis and electrical conductivity of a polyacrylamide/Cu conducting hydrogel. *Reactive and Functional Polymers*, **67**, 489–494 (2007). DOI: [10.1016/j.reactfunctpolym.2007.02.002](https://doi.org/10.1016/j.reactfunctpolym.2007.02.002)
- [6] Lin J., Tang Q., Wu J., Hao S.: The synthesis and electrical conductivity of a polyacrylate/graphite hydrogel. *Reactive and Functional Polymers*, **67**, 275–281 (2007). DOI: [10.1016/j.reactfunctpolym.2007.01.011](https://doi.org/10.1016/j.reactfunctpolym.2007.01.011)
- [7] Tang Q., Wu J., Lin J.: A multifunctional hydrogel with high conductivity, pH-responsive, thermo-responsive and release properties from polyacrylate/polyaniline hybrid. *Carbohydrate Polymers*, **73**, 315–321 (2008). DOI: [10.1016/j.carbpol.2007.11.036](https://doi.org/10.1016/j.carbpol.2007.11.036)
- [8] Tang Q., Wu J., Sun H., Fan S., Hu D., Lin J.: Superabsorbent conducting hydrogel from poly(acrylamide-aniline) with thermo-sensitivity and release properties. *Carbohydrate Polymers*, **73**, 473–481 (2008). DOI: [10.1016/j.carbpol.2007.12.030](https://doi.org/10.1016/j.carbpol.2007.12.030)
- [9] Peppas N. A., Bures P., Leobandung W., Ichikawa H.: Hydrogels in pharmaceutical formulations. *European Journal of Pharmaceutics and Biopharmaceutics*, **50**, 27–46 (2000). DOI: [10.1016/S0939-6411\(00\)00090-4](https://doi.org/10.1016/S0939-6411(00)00090-4)
- [10] Sharma Y., Tiwari A., Hattori S., Terada D., Sharma A. K., Ramalingam M., Kobayashi H.: Fabrication of conducting electrospun nanofibers scaffold for three-dimensional cells culture. *International Journal of Biological Macromolecules*, **51**, 627–631 (2012). DOI: [10.1016/j.ijbiomac.2012.06.014](https://doi.org/10.1016/j.ijbiomac.2012.06.014)
- [11] Buenger D., Topuz F., Groll J.: Hydrogels in sensing applications. *Progress in Polymer Science*, **37**, 1678–1719 (2012). DOI: [10.1016/j.progpolymsci.2012.09.001](https://doi.org/10.1016/j.progpolymsci.2012.09.001)
- [12] Kaith B. S., Saruchi, Jindal R., Bhatti M. S.: Screening and RSM optimization for synthesis of a *Gum tragacanth*-acrylic acid based device for *in situ* controlled cetirizine dihydrochloride release. *Soft Matter*, **8**, 2286–2293 (2012). DOI: [10.1039/C2SM07033B](https://doi.org/10.1039/C2SM07033B)
- [13] Deshmukh A. S., Setty C. M., Badiger A. M., Muralikrishna K. S.: Gum ghatti: A promising polysaccharide for pharmaceutical applications. *Carbohydrate Polymers*, **87**, 980–986 (2012). DOI: [10.1016/j.carbpol.2011.08.099](https://doi.org/10.1016/j.carbpol.2011.08.099)
- [14] Rana V., Rai P., Tiwari A. K., Singh R. S., Kennedy J. F., Knill C. J.: Modified gums: Approaches and applications in drug delivery. *Carbohydrate Polymers*, **83**, 1031–1047 (2011). DOI: [10.1016/j.carbpol.2010.09.010](https://doi.org/10.1016/j.carbpol.2010.09.010)
- [15] Ghosh S., Sen G., Jha U., Pal S.: Novel biodegradable polymeric flocculant based on polyacrylamide-grafted tamarind kernel polysaccharide. *Bioresource Technology*, **101**, 9638–9644 (2010). DOI: [10.1016/j.biortech.2010.07.058](https://doi.org/10.1016/j.biortech.2010.07.058)
- [16] Malhotra B. D., Ghosh S., Chandra R.: Polyaniline/polymeric acid composite, a novel conducting rubber. *Journal of Applied Polymer Science*, **40**, 1049–1052 (1990). DOI: [10.1002/app.1990.070400536](https://doi.org/10.1002/app.1990.070400536)
- [17] Tiwari A., Sharma Y., Hattori S., Terada D., Sharma A. K., Turner A. P. F., Kobayashi H.: Influence of poly(*n*-isopropylacrylamide)-CNT-polyaniline three-dimensional electrospun microfabric scaffolds on cell growth and viability. *Biopolymers*, **99**, 334–341 (2013). DOI: [10.1002/bip.22170](https://doi.org/10.1002/bip.22170)
- [18] Pron A., Genoud F., Menardo C., Nechtschein M.: The effect of the oxidation conditions on the chemical polymerization of polyaniline. *Synthetic Metals*, **24**, 193–201 (1988). DOI: [10.1016/0379-6779\(88\)90257-3](https://doi.org/10.1016/0379-6779(88)90257-3)
- [19] Syed A. A., Dinesan M. K.: Review: Polyaniline – A novel polymeric material. *Talanta*, **38**, 815–837 (1991). DOI: [10.1016/0039-9140\(91\)80261-W](https://doi.org/10.1016/0039-9140(91)80261-W)
- [20] Cortés M. T., Sierra E. V.: Effect of synthesis parameters in polyaniline: Influence on yield and thermal behavior. *Polymer Bulletin*, **56**, 37–45 (2006). DOI: [10.1007/s00289-005-0467-1](https://doi.org/10.1007/s00289-005-0467-1)

- [21] Mittal H., Mishra S. B., Mishra A. K., Kaith B. S., Jindal R.: Flocculation characteristics and biodegradation studies of *Gum ghatti* based hydrogels. *International Journal of Biological Macromolecules*, **58**, 37–46 (2013). DOI: [10.1016/j.ijbiomac.2013.03.045](https://doi.org/10.1016/j.ijbiomac.2013.03.045)
- [22] Rani P., Sen G., Mishra S., Jha U.: Microwave assisted synthesis of polyacrylamide grafted gum ghatti and its application as flocculant. *Carbohydrate Polymers*, **89**, 275–281 (2012). DOI: [10.1016/j.carbpol.2012.03.009](https://doi.org/10.1016/j.carbpol.2012.03.009)
- [23] Tiwari A., Singh V.: Synthesis and characterization of electrical conducting chitosan-graft-polyaniline. *Express Polymer Letters*, **1**, 308–317 (2007). DOI: [10.3144/expresspolymlett.2007.44](https://doi.org/10.3144/expresspolymlett.2007.44)
- [24] Shukla S. K., Tiwari A.: Synthesis of chemical responsive chitosan-grafted-polyaniline bio-composite. *Advanced Materials Research*, **306–307**, 82–86 (2011). DOI: [10.4028/www.scientific.net/AMR.306-307.82](https://doi.org/10.4028/www.scientific.net/AMR.306-307.82)
- [25] Tiwari A.: Gum arabic-graft-polyaniline: An electrically active redox biomaterial for sensor applications. *Journal of Macromolecular Science Part A: Pure and Applied Chemistry*, **44**, 735–745 (2007). DOI: [10.1080/10601320701353116](https://doi.org/10.1080/10601320701353116)
- [26] Tiwari A., Singh S. P.: Synthesis and characterization of biopolymer-based electrical conducting graft copolymers. *Journal of Applied Polymer Science*, **108**, 1169–1177 (2008). DOI: [10.1002/app.27789](https://doi.org/10.1002/app.27789)
- [27] Singh V., Tiwari A., Pandey S., Singh S. K.: Peroxydisulfate initiated synthesis of potato starch-graft-poly(acrylonitrile) under microwave irradiation. *Express Polymer Letters*, **1**, 51–58 (2007). DOI: [10.3144/expresspolymlett.2007.10](https://doi.org/10.3144/expresspolymlett.2007.10)
- [28] Kaith B. S., Kumar K.: In air synthesis of poly-cl-poly(AAm) network and its application in water-absorption from oil-water emulsions. *Express Polymer Letters*, **1**, 474–480 (2007). DOI: [10.3144/expresspolymlett.2007.66](https://doi.org/10.3144/expresspolymlett.2007.66)
- [29] Kaith B. S., Sharma K., Kumar V., Kumar V., Swart H. C., Kalia S.: Effects of swift heavy ion beam irradiation on the structural and morphological properties of poly(methacrylic acid) cross-linked gum ghatti films. *Vacuum*, **101**, 166–170 (2014). DOI: [10.1016/j.vacuum.2013.08.020](https://doi.org/10.1016/j.vacuum.2013.08.020)
- [30] Sharma K., Kaith B. S., Kumar V., Kumar V., Som S., Kalia S., Swart H. C.: Synthesis and properties of poly(acrylamide-aniline)-grafted gum ghatti based nanospikes. *RSC Advances*, **3**, 25830–25839 (2013). DOI: [10.1039/c3ra44809f](https://doi.org/10.1039/c3ra44809f)
- [31] Tiwari A., Singh V.: Microwave-induced synthesis of electrical conducting gum acacia-graft-polyaniline. *Carbohydrate Polymers*, **74**, 427–434 (2008). DOI: [10.1016/j.carbpol.2008.03.015](https://doi.org/10.1016/j.carbpol.2008.03.015)
- [32] Singh V., Tiwari A., Sanghi R.: Studies on $K_2S_2O_8$ /ascorbic acid initiated synthesis of *Ipomoea dasysperma* seed gum-g-poly(acrylonitrile): A potential industrial gum. *Journal of Applied Polymer Science*, **98**, 1652–1662 (2005). DOI: [10.1002/app.22333](https://doi.org/10.1002/app.22333)
- [33] Singh V., Tiwari A., Shukla P., Singh S. P., Sanghi R.: Grafting of methylmethacrylate on to the plant seed galactomannans using potassium persulphate/ascorbic acid redox pair. *Reactive and Functional Polymers*, **66**, 1306–1318 (2006). DOI: [10.1016/j.reactfunctpolym.2006.03.013](https://doi.org/10.1016/j.reactfunctpolym.2006.03.013)
- [34] Ding Y., Padias A. B., Hall H. K. Jr.: Chemical trapping experiments support a cation-radical mechanism for the oxidative polymerization of aniline. *Journal of Polymer Science Part A: Polymer Chemistry*, **37**, 2569–2579 (1999). DOI: [10.1002/\(SICI\)1099-0518\(19990715\)37:14<2569::AID-POLA30>3.0.CO;2-N](https://doi.org/10.1002/(SICI)1099-0518(19990715)37:14<2569::AID-POLA30>3.0.CO;2-N)
- [35] Chen J., Zhao Y.: Relationship between water absorbency and reaction conditions in aqueous solution polymerization of polyacrylate superabsorbents. *Journal of Applied Polymer Science*, **75**, 808–814 (2000). DOI: [10.1002/\(SICI\)1097-4628\(20000207\)75:6<808::AID-APP10>3.0.CO;2-3](https://doi.org/10.1002/(SICI)1097-4628(20000207)75:6<808::AID-APP10>3.0.CO;2-3)
- [36] Pourjavadi A., Harzandi A. M., Hosseinzadeh H.: Modified carrageenan 3. Synthesis of a novel polysaccharide-based superabsorbent hydrogel via graft copolymerization of acrylic acid onto kappa-carrageenan in air. *European Polymer Journal*, **40**, 1363–1370 (2004). DOI: [10.1016/j.eurpolymj.2004.02.016](https://doi.org/10.1016/j.eurpolymj.2004.02.016)
- [37] Athawale V. D., Rathi S. C.: Graft polymerization: Starch as a model substrate. *Journal of Macromolecular Science Part C: Polymer Reviews*, **39**, 445–480 (1999). DOI: [10.1081/MC-100101424](https://doi.org/10.1081/MC-100101424)
- [38] Motonaga T., Shibayama M.: Studies on pH and temperature dependence of the dynamics and heterogeneities in poly(N-isopropylacrylamide-co-sodium acrylate) gels. *Polymer*, **42**, 8925–8934 (2001). DOI: [10.1016/S0032-3861\(01\)00380-9](https://doi.org/10.1016/S0032-3861(01)00380-9)
- [39] Saraydin D., Karadag B., Çetinkaya S., Güven O.: Preparation of acrylamide/maleic acid hydrogels and their biocompatibility with some biochemical parameters of human serum. *Radiation Physics and Chemistry*, **46**, 1049–1052 (1995). DOI: [10.1016/0969-806X\(95\)00318-R](https://doi.org/10.1016/0969-806X(95)00318-R)
- [40] Singhal R., Gupta I.: A study on the effect of butyl methacrylate content on swelling and controlled-release behavior of poly (acrylamide-co-butyl-methacrylate-co-acrylic acid) environment-responsive hydrogels. *International Journal of Polymeric Materials*, **59**, 757–776 (2010). DOI: [10.1080/00914037.2010.483216](https://doi.org/10.1080/00914037.2010.483216)

- [41] Li Q., Ma Z., Yue Q., Gao B., Li W., Xu X.: Synthesis, characterization and swelling behavior of superabsorbent wheat straw graft copolymers. *Bioresource Technology*, **118**, 204–209 (2012).
DOI: [10.1016/j.biortech.2012.03.028](https://doi.org/10.1016/j.biortech.2012.03.028)
- [42] Pourjavadi A., Mahdavinia G. R., Zohuriaan-Mehr M. J.: Modified chitosan. II. H-chitoPAN, a novel pH-responsive superabsorbent hydrogel. *Journal of Applied Polymer Science*, **90**, 3115–3121 (2003).
DOI: [10.1002/app.13054](https://doi.org/10.1002/app.13054)
- [43] Mahdavinia G. R., Mousavi S. B., Karimi F., Marandi G. B., Garabaghi H., Shahabvand S.: Synthesis of porous poly(acrylamide) hydrogels using calcium carbonate and its application for slow release of potassium nitrat. *Express Polymer Letters*, **3**, 279–285 (2009).
DOI: [10.3144/expresspolymlett.2009.35](https://doi.org/10.3144/expresspolymlett.2009.35)
- [44] Kaith B. S., Sharma K., Kumar V., Kalia S., Swart H. C.: Fabrication and characterization of gum ghatti-polymethacrylic acid based electrically conductive hydrogels. *Synthetic Metals*, **187**, 61–67 (2014).
DOI: [10.1016/j.synthmet.2013.10.021](https://doi.org/10.1016/j.synthmet.2013.10.021)
- [45] Tiwari A., Gong S.: Electrochemical detection of a breast cancer susceptible gene using cDNA immobilized chitosan-co-polyaniline electrode. *Talanta*, **77**, 1217–1222 (2009).
DOI: [10.1016/j.talanta.2008.08.029](https://doi.org/10.1016/j.talanta.2008.08.029)
- [46] Tiwari A., Kumar R., Prabakaran M., Pandey R. R., Kumari P., Chaturvedi A., Mishra A. K.: Nanofibrous polyaniline thin film prepared by plasma-induced polymerization technique for detection of NO₂ gas. *Polymers for Advanced Technologies*, **21**, 615–620 (2010).
DOI: [10.1002/pat.1470](https://doi.org/10.1002/pat.1470)
- [47] Tiwari A., Shukla S. K.: Chitosan-g-polyaniline: A creatine amidinohydrolase immobilization matrix for creatine biosensor. *Express Polymer Letters*, **3**, 553–559 (2009).
DOI: [10.3144/expresspolymlett.2009.69](https://doi.org/10.3144/expresspolymlett.2009.69)
- [48] Shumaila, Alam M., Siddiqui A. M., Husain M.: Synthesis, characterization and properties of Se nanowires intercalated polyaniline/Se nanocomposites. *Express Polymer Letters*, **7**, 723–732 (2013).
DOI: [10.3144/expresspolymlett.2013.70](https://doi.org/10.3144/expresspolymlett.2013.70)
- [49] Patil R. C., Patil S. F., Mulla I. S., Vijayamohan K.: Effect of protonation media on chemically and electrochemically synthesized polyaniline. *Polymer International*, **49**, 189–196 (2000).
DOI: [10.1002/\(SICI\)1097-0126\(200002\)49:2<189::AID-PI325>3.0.CO;2-9](https://doi.org/10.1002/(SICI)1097-0126(200002)49:2<189::AID-PI325>3.0.CO;2-9)
- [50] Jósefowicz M. E., Epstein A. J., Tang X.: Protonic acid doping of two classes of the emeraldine form of polyaniline. *Synthetic Metals*, **46**, 337–340 (1992).
DOI: [10.1016/0379-6779\(92\)90359-Q](https://doi.org/10.1016/0379-6779(92)90359-Q)
- [51] Kulkarni M. V., Viswanath A. K., Marimuthu R., Seth T.: Spectroscopic, transport, and morphological studies of polyaniline doped with inorganic acids. *Polymer Engineering and Science*, **44**, 1676–1681 (2004).
DOI: [10.1002/pen.20167](https://doi.org/10.1002/pen.20167)
- [52] Tiwari A., Sen V., Dhakate S. R., Mishra A. P., Singh V.: Synthesis, characterization, and hoping transport properties of HCl doped conducting biopolymer-co-polyaniline zwitterion hybrids. *Polymers for Advanced Technologies*, **19**, 909–914 (2008).
DOI: [10.1002/pat.1058](https://doi.org/10.1002/pat.1058)
- [53] Kroschwitz J. I.: *Electrical and electronic properties of polymers: A state-of-the-art compendium*. Wiley, New York (1988).
- [54] Malik H., Gupta N., Sarkar A.: Anisotropic electrical conduction in gum Arabica – A biopolymer. *Materials Science and Engineering: C*, **20**, 215–218 (2002).
DOI: [10.1016/S0928-4931\(02\)00036-X](https://doi.org/10.1016/S0928-4931(02)00036-X)
- [55] Li Q., Cruz L., Phillips P.: Granular-rod model for electronic conduction in polyaniline. *Physical Review B*, **47**, 1840–1845 (1993).
DOI: [10.1103/PhysRevB.47.1840](https://doi.org/10.1103/PhysRevB.47.1840)

Polypropylene/ethylene-propylene rubber (PP/EPR) blends for the automotive industry: Basic correlations between EPR-design and shrinkage

G. Grestenberger^{*}, G. D. Potter, C. Grein⁺

Borealis Polyolefine GmbH PO R&, St.-Peter-Strasse 25, A-4021 Linz, Austria

⁺Present address: SABIC Europe, P.O. Box 5151, 6130 PD Sittard, The Netherlands

Received 22 July 2013; accepted in revised form 14 December 2013

Abstract. The influence of the phase morphology on the shrinkage of injection molded plates from reactor based PP/EPR blends was investigated using a model series. The morphology of the dispersed phase – in terms of size and shape of the rubber particles as determined from scanning electron microscopy (SEM) – was found to correlate fairly well with the shrinkage determined in the flow and transverse direction of injection molded plates. In this respect it turned out to be elementary to consider the anisotropy of the particles rather than their average size alone. Additionally, the effect of the EPR design on the coefficient of linear thermal expansion (CLTE) was evaluated and brought into a relationship with the blend morphology.

Keywords: polymer blends, polypropylene, morphology, injection molding

1. Introduction

Automotive parts like bumpers, body panels, dashboards and door claddings are nowadays made out of advanced polypropylene (PP) materials. Most of the time, heterophasic blends – where PP is the continuous phase and an ethylene-propylene copolymer (EPR) the dispersed one – are used. The polypropylene matrix delivers the stiffness of the material whereas the rubbery inclusions act as impact modifiers providing a grade with balanced stiffness-impact behavior. Besides this basic requirement, getting a low shrinkage (i.e. a very limited difference between mold and part geometry) and a low thermal expansion is also more and more targeted. The latter is especially relevant when polymer parts are combined with metal parts which will normally have a significantly lower thermal expansion in the application temperature range.

Shrinkage is not an intrinsic material property, but rather a result of the thermal and mechanical conditions a material experiences during processing. The main factors that influence the shrinkage of the final part are the polymer itself, the processing parameters, the mold design and the geometry of the molded part.

Most studies concerning post-molding shrinkage of polypropylene (PP) parts focus on the influence of molding parameters (temperature and speed), geometry and mold design [1–5], very often using only one defined polymer for performing the study. One of the earliest extensive studies regarding molecular structure and polymer composition effects on the shrinkage of PP was done by Fujiyama and Kimura [6], in which both the general reduction of shrinkage with increasing melt flow rate (MFR) and the additional shrinkage-reducing effect of elastomer

^{*}Corresponding author, e-mail: georg.grestenberger@borealisgroup.com

particles and filler became apparent already. For PP homopolymers, these studies were later expanded to variations of molecular weight distribution (MWD) and isotacticity [7] to show a massive effect of MWD polydispersity on morphology (skin layer formation) and shrinkage.

When more complex compositions involving elastomer and filler components have to be considered, the contributions of the various components to shrinkage were analyzed (e.g. Pantani and Titomanlio [8]), finding reasonable agreements for a volume-based addition approach in model experiments. While platy mineral particles like talc have been found to have a stabilizing effect, reducing the shrinkage in a rather isotropic manner [9], fibrillar or acicular particles like glass fibers or multi-walled carbon nanotubes (MWNT) will certainly increase shrinkage anisotropy due to their high degree or orientation in flow direction during mold filling [10]. In addition to the composition, the testing time for shrinkage also needs to be considered, as different polymer compositions and/or processing parameter sets will generate different time dependences of shrinkage [3, 11].

The number of studies dealing with the thermal expansion of PP parts which is frequently expressed as the coefficient of linear thermal expansion (CLTE) is significantly lower than for shrinkage. The morphology plays a decisive role, even more than for the case of shrinkage, on top of the component contributions as demonstrated in the work of Ono and coworkers [12, 13]. The development of highly oriented elastomer arrays or networks through the selection of a suitable viscosity ratio can quite obviously reduce expansion significantly. Especially in combination with a modification by solid micro- or nanoparticles [14], the interactions can become very complex as these particles will in turn modify the phase morphology.

Hence, the present study aims to evaluate the influence of the phase morphology on the shrinkage and CLTE (coefficient of linear thermal expansion) of PP/EPR blends. For this purpose, in-reactor made heterophasic copolymers have been investigated and key morphology drivers were varied systematically based on earlier experience in polymer development.

2. Experimental

2.1. Materials

A set of eight in-reactor made heterophasic copolymers with a systematic variation in molecular weight of the rubber portion at comparable EPR compositions were polymerized in lab scale (Table 1 and Table 2). To evaluate the effect of matrix crystallinity, both a series with and without in-reactor nucleation were prepared.

These materials were polymerized in a multi-stage process using a 4th generation Ziegler-Natta catalyst supported on MgCl₂ in combination with a silane donor and triethyl-aluminum as an activator/scavenger. For the in-reactor nucleated versions, the catalyst system further contained isotactic poly(vinyl cyclohexane) (PVCH) as a polymeric nucleating agent. PVCH is effective at already very low loadings (<100 ppm) and, compared to other external nucleating agents, shows clear advantages in terms of mechanical and optical properties [15, 16].

In particular, the investigated heterophasic copolymers consist of an isotactic PP homopolymer matrix with a Melt Flow Rate (MFR) of ~40 g/10 min (ISO 1133, 230°C/2.16 kg) and about 29 wt% of an ethylene-propylene copolymer (EPR). Apart from the molecular weight of the EPR phase, all other polymer parameters were kept rather constant throughout the series. Since the investigated materials have been produced in a two stage polymerization process, the EPR phase is not accessible independently. Therefore, the xylene cold soluble (XCS) fraction (determined acc. ISO 6427-1992) was assumed to represent the EPR phase. The average molecular weight of the rubber (EPR) fraction was

Table 1. Material composition parameters of non-nucleated samples

	IV 1.5	IV 1.9	IV 2.2	IV 2.5
XCS-content [wt%]	29.2	31.2	31.5	31.7
C ₂ -content of XCS [wt%]	34.4	34.6	34.3	33.4
IV of XCS [dL/g]	1.5	1.9	2.2	2.5
MFR [g/10 min]	27.2	19.4	16.3	14.4

Table 2. Material composition parameters of in-reactor nucleated samples

	IV 1.5N	IV 1.9N	IV 2.2N	IV 2.5N
XCS-content [wt%]	27.9	29.0	29.4	27.6
C ₂ -content of XCS [wt%]	36.2	36.3	36.5	34.2
IV of XCS [dL/g]	1.5	1.9	2.2	2.5
MFR [g/10 min]	27.1	20.6	17.1	14.7

assessed by intrinsic viscosity (IV) measurements of the XCS fraction (ISO 1628-1, decaline at 135°C) and varied between 1.5 and 2.5 dL/g.

The comonomer (ethylene) content was determined by quantitative Fourier transform infrared spectroscopy (FTIR) after basic assignment calibrated via quantitative ¹³C nuclear magnetic resonance (NMR) spectrometry in a manner well known in the art. Thin films were pressed from the XCS fraction to a thickness of ~300 μm and spectra recorded in transmission mode. Specifically, the ethylene content of the EPR was determined using the baseline corrected peak area of the quantitative bands found at 720–722 and 730–30 733 cm⁻¹. Quantitative results were obtained based upon reference to the film thickness, and the ethylene content of the XCS fraction was 35±1.5 wt% for all materials.

2.2. Dimensional stability

2.2.1. Shrinkage

Shrinkage was determined on injection molded quadratic plaques of 60×60×2 mm³. The film gated specimens were produced on an Engel V60 injection molding machine. The following process parameters were applied: 200°C melt temperature, 100 mm/s flow front velocity (inside the mold), 10 seconds holding pressure time and 10 bars hydraulic holding pressure level. The dimensions (length and width) of the plaques were determined with a digital measuring slide and compared to the dimensions of the cavity at room temperature about (but not less than) 96 h after de-molding.

2.2.2. Coefficient of linear thermal expansion (CLTE)

CLTE measurements were done at Johannes Kepler University Linz (Institute of Polymer Science) in accordance with DIN 53752 on 10×10×4 mm³ specimen prepared from injection molded test bars (80×10×4 mm³). These test bars are normally used for assessment of Charpy impact strength according to ISO 179 and the central portion of the bars is cut and polished for the CLTE measurements. The thermal expansion in flow direction was monitored in a temperature range from -30°C to +80°C. The average CLTE on a given temperature range (α_{T_1/T_2}) is defined by Equation (1):

$$\alpha_{T_1/T_2} = \frac{1}{L} \frac{L_2 - L_1}{T_2 - T_1} \quad (1)$$

where L , L_1 and L_2 are resp. the reference length determined at 23°C, the length measured at temperature T_1 and the length at temperature T_2 .

2.3. Scanning electron microscopy (SEM)

For morphology investigations the shrinkage specimens as defined above were cut perpendicular to the flow direction. The surface of the specimens was prepared with an ultra-cryo-microtome (PMC PC-PT). To increase the contrast between matrix and rubber phase the samples were etched in n-heptane at room temperature over night (~14 hours). n-heptane dissolves the amorphous EPR-inclusions but hardly affects the semi-crystalline PP matrix. Holes are created in the samples surface due to the removal of the EPR particles. These holes appear as dark regions in the SEM image allowing an evaluation of the dispersed phase morphology. Following this procedure SEM micrographs were taken from the skin to the core of the specimen in order to assess and quantify the changes in particle size and shape over the thickness. The SEM investigations were done with a FEI Quanta 200 FEG microscope at an acceleration voltage of 5.0 kV and various magnifications (1,000–30,000×).

3. Results and discussion

3.1. Morphology

From the overview of SEM images in Figure 1, it is obvious that the particle size of the dispersed EPR phase is affected significantly by the molecular weight of the EPR phase. As both matrix viscosity and the composition of the EPR is similar for all samples the phase viscosity ratio between matrix and rubber can be assumed to be the driving force for this development [17–22].

For heterophasic polymer systems like the investigated ethylene-propylene copolymers (also termed rTPOs for ‘reactor thermoplastic polyolefins’) the viscosity ratio λ between dispersed phase and matrix phase is known to control the final morphology. The ratio in dynamic viscosity between rubber and matrix at a defined shear rate is considered for the calculation of λ (e.g. compare [17] and [18]), as shown by Equation (2):

$$\lambda = \frac{\eta_d^*}{\eta_m^*} \quad (2)$$

For a first approximation and in lack of viscosity data from dynamic measurements, λ can also be

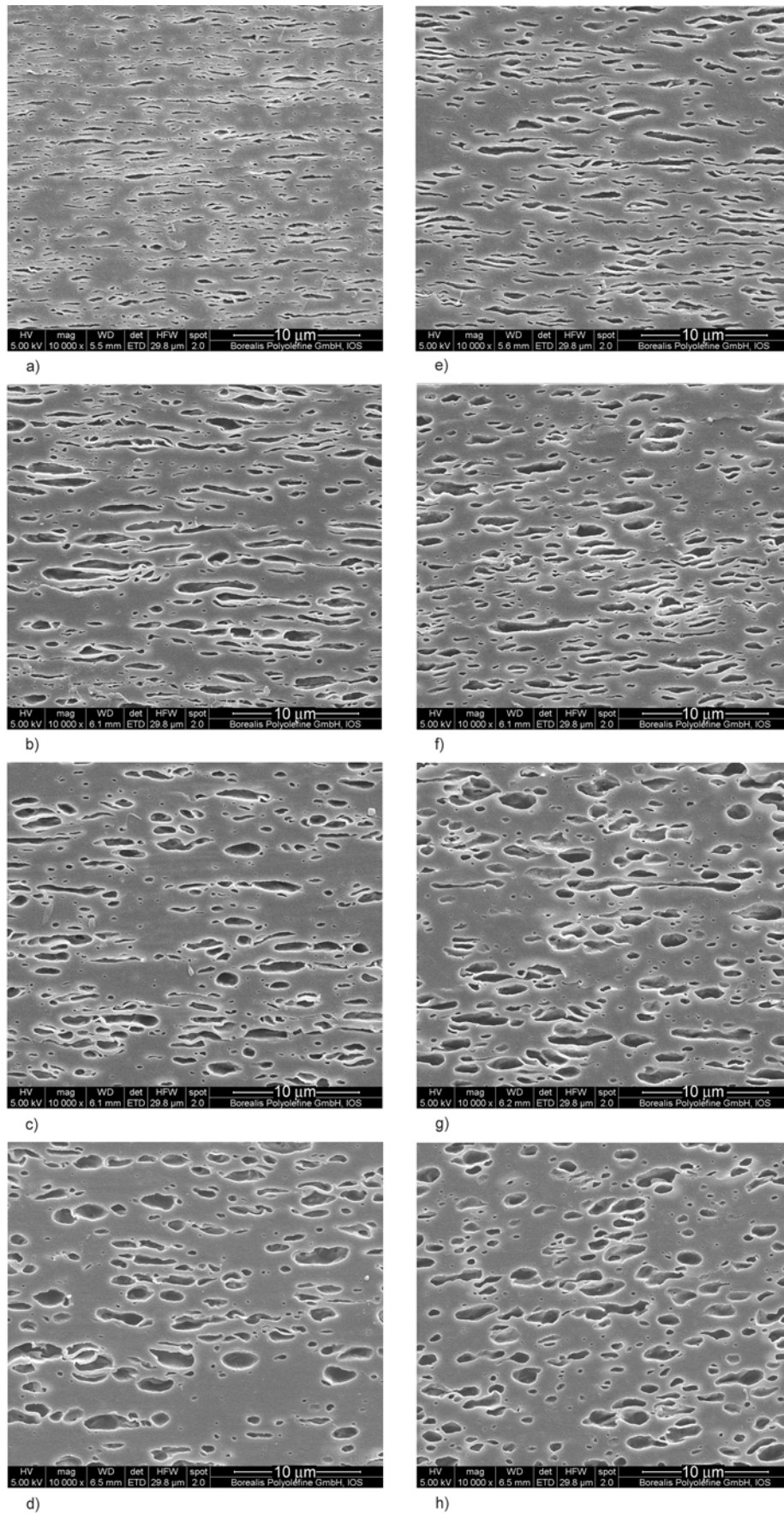


Figure 1. SEM-images of the investigated plates taken at different distances from the surface of the samples: IV(XCS) 1.5–1.9–2.2–2.5 from top to bottom, skin layer at 100 μm below surface left column a–d, core layer at 1000 μm below surface right column e–h; MD perpendicular to image plane, TD horizontal, ND vertical).

determined by the ratio in intrinsic viscosity between dispersed phase IV_d and matrix phase IV_m (e.g. compare [18] and [19], see Equation (3)), provided that relative rather than absolute values are targeted:

$$\lambda = \frac{IV_d}{IV_m} \quad (3)$$

While the final phase morphology may be affected by the processing step, the particle size distribution (PSD) is mostly defined by particle break-up and aggregation during the melt mixing (compounding or pelletization) step [21]. In this respect, the initial particle size expressed by the radius R , the interfacial tension α between the phases and the actual shear rate γ^* control the dispersion process in this melt mixing step. Particle deformation and break up only occurs if the according Equation (4) calculated Weber number is larger than a critical value [18].

$$We = \frac{\gamma^* \eta_m \cdot R}{\alpha} \quad (4)$$

This effect has not being considered quantitatively in the current investigation due to a lack of experimental data for radius R and interfacial tension α .

In earlier studies, the various averages of the same PSD have been related to the melt viscosity ratio and/or the compatibility between the phases, often expressed by the interfacial tension α . Wu [23] as well as Serpe *et al.* [24] have investigated blend combinations with high chemical diversity and consequently high interfacial tensions e.g. nylon and polyester as the matrix and EPR as the dispersed phase. More relevant for the present study, in which matrix and disperse phase are very similar, are papers like the ones by Mighri *et al.* [25] and Kock *et al.*

[26]. None of these studies investigated reactor-based heterophasic systems like the ones in this study. Common to all these works is the fact that for reliable results relaxed specimens are necessary to determine equilibrium PSDs with spherical EPR particles.

From the SEM images the size distribution (PSD) of the dispersed EPR particles was determined by means of Image J (V1.43), a public domain Java image processing and analysis software [27]. Since the morphology of the dispersed phase is believed to be only marginally affected by an additional alpha nucleation, SEM images were taken from the nucleated materials only. The validity of this assumption was proven by comparing the morphologies of samples IV2.2 and IV2.2N (Figure 2). It can consequently be assumed that nucleation will affect shrinkage and CLTE largely independent of the phase morphology.

The morphology images were reworked manually before analyzing the size and shape of the EPR particles. This was inevitable since the contrast between the dark areas (holes where the EPR was extracted) and the matrix phase was too low to allow an automated detection of the phase boundaries via Image J. In a subsequent step, the manually contrasted images were converted into binary images (i.e. converted into black and white images). All particles at the edges of the image where excluded from the analysis to avoid misinterpretation of the data. Furthermore, a minimum particle size of $0.05 \mu\text{m}^2$ was defined in order to remove speckles and noise in the pictures.

Assuming spherical particles for the sake of PSD, the average particle diameters in number D_n , in weight

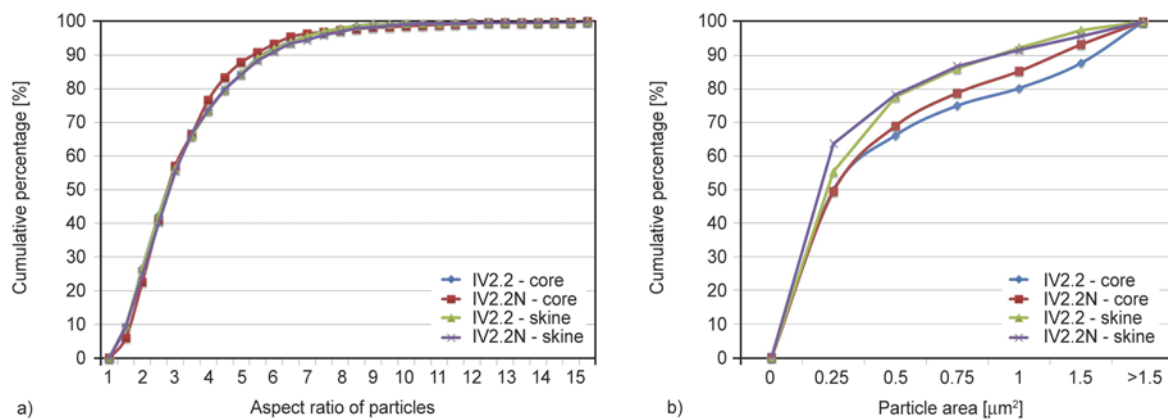


Figure 2. Distribution of particle aspect ratio (a) and particle size (b) for the nucleated and non-nucleated version of sample IV2.2

D_w and in volume D_v were evaluated according to [19] and [20] as Equation (5):

Average particle diameters in number D_n

$$D_n = \frac{\sum_{i=1}^N n_i D_i}{\sum_{i=1}^N n_i} \quad (5)$$

Average particle diameters in weight D_w (Equation (6)):

$$D_w = \frac{\sum_{i=1}^N n_i D_i^2}{\sum_{i=1}^N n_i D_i} \quad (6)$$

Average particle diameters in volume D_v (Equation (7)):

$$D_v = \frac{\sum_{i=1}^N n_i D_i^4}{\sum_{i=1}^N n_i D_i^3} \quad (7)$$

Applying Equations (5)–(7) to the particle sizes in the core as well as near the surface of the specimen allowed for the determination of D_n , D_w and D_v from the SEM-images. It can be clearly observed from Figure 3 and Table 3 that the average particle size of the dispersed phase increases with the intrinsic viscosity of the EPR phase, i.e. with increasing melt viscosity ratio between the phases. This is

completely in line with previous experience [19, 20]. Furthermore, the particles are smaller in the high shear skin region than in the core of the specimens. Although this is in line with literature (compare [17–22] and [25–28]), the determined diameters are not reflecting the actual shape of EPR the particles.

The particles are oriented and elongated during the filling of the mold. The assumption of spherical particles is an inaccurate approximation of the actual particles shape. Therefore, the average particle diameter and IV of the XCS show a low correlation coefficient. For a better correlation between polymer design parameters and morphology, the aspect ratio in combination with the particle area was considered further on.

Image J automatically fits an ellipse of the same area to each particle and records its shape and aspect ratio. The ellipse’s area A and aspect ratio AR are determined by Equations (8) and (9):

$$A = \pi \cdot \frac{a}{2} \cdot \frac{b}{2} \quad (8)$$

$$AR = \frac{a}{b} \quad (9)$$

In these equations, a is the major axis and b the minor axis of the fitted ellipse. The number average particle height and width were determined by applying this simple calculation. With this approach, a nicely fitting logarithmic correlation between IV of

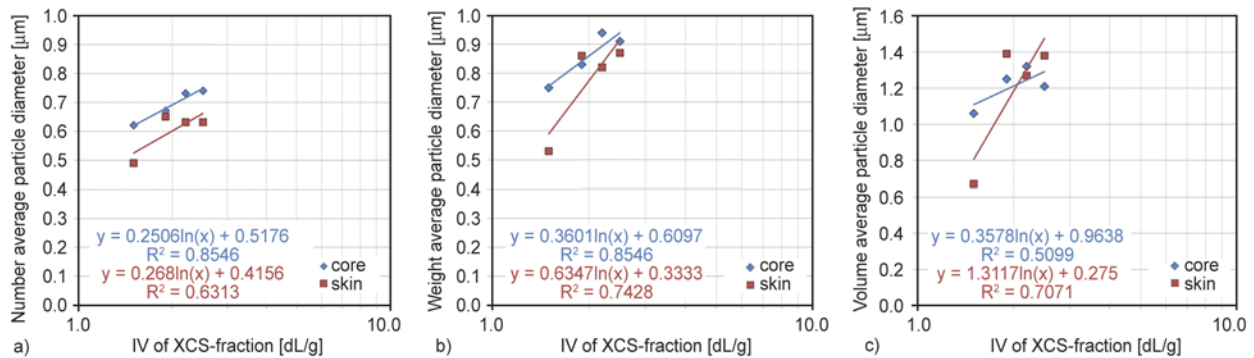


Figure 3. Average particle diameters by number (a), weight (b) and volume (c) as function of the intrinsic viscosity of the dispersed EPR phase (XCS fraction) determined for nucleated samples

Table 3. Average particle diameters of in-reactor nucleated materials (spherical particles assumed)

Region	Parameter	Unit	IV1.5N	IV1.9N	IV2.2N	IV2.5N
Core	Number average particle diameter, D_n	μm	0.62	0.67	0.73	0.74
	Weight average particle diameter, D_w	μm	0.75	0.83	0.94	0.91
	Volume average particle diameter, D_v	μm	1.06	1.25	1.32	1.21
Skin	Number average particle diameter, D_n	μm	0.49	0.65	0.63	0.63
	Weight average particle diameter, D_w	μm	0.53	0.86	0.82	0.87
	Volume average particle diameter, D_v	μm	0.67	1.39	1.27	1.38

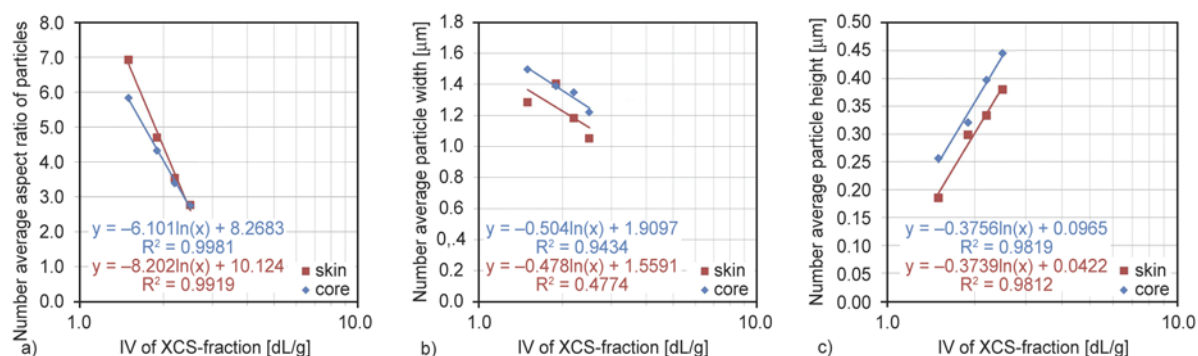


Figure 4. Average particle aspect ratio by number (a), particle height (b) and particle width (c) as function of the intrinsic viscosity of the dispersed EPR phase (XCS fraction) determined for nucleated samples

XCS and particle dimensions could be found (Figure 4). Only the particle width in the skin region of sample IV1.9N was not fitting into this correlation. A possible explanation for this outlier could be a more pronounced agglomeration of particles (compare Figure 1). However, a more in-depth analysis of the samples morphology in flow direction would be required to prove this assumption.

Plotting the number average aspect ratio versus the IV of the EPR phase (i.e. XCS) shows that the deformation of particles in processing is most pronounced for the sample IV1.5N and steadily decreases with increasing molecular weight of the rubber. On the other hand the area of particles is lowest for IV1.5N and almost linearly increases with the intrinsic viscosity (compare Figure 5). Furthermore, some significant changes in morphology along the specimen thickness were found. As expected, particles in the skin region showed a clearly higher orientation than in the core. This phenomenon was most pronounced for samples IV1.5N and IV1.9N. Only minor differences in particle deformation along the lateral direction were found in the case of IV 2.2N and IV 2.5N (compare Figure 5).

3.2. Shrinkage

Injection molded parts of crystalline polymers are known to exhibit a skin-core structure rather independent of the type of polymer. For impact modified PP, this effect was described by e.g. Karger-Kocsis and Csikai [17]. Taking into account this skin-core structure, Fujiyama and Kimura [6] claim that the shrinkage in flow direction is increasing with the crystalline skin layer thickness of injection molded plaques which in turn is influenced by flowability, molar mass distribution etc. Corresponding light

microscopy investigations of samples IV1.5N to IV2.5N did not show any change in skin layer thickness.

It is difficult to link the shrinkage data to the particle size of the rubbery phase due to the differences in orientation of particles and the skin core structure of the samples. Just the morphology in the core was subsequently considered in order to simplify the analysis. Applying this simplification, an increase in shrinkage with increasing IV of XCS and particle size was found. This shows that shrinkage is linked to the molecular weight of the dispersed phase and viscosity ratio between rubber and matrix respectively. However, the almost identical average particle area of sample IV2.2N and IV2.5N but significantly different shrinkage results (Figure 6) indicate that not only the size but also the shape of particles has a decisive influence on the shrinkage of heterophasic systems. Therefore, the actual particle dimensions were linked to shrinkage instead of the particle area. As already mentioned above, the particle area and particle aspect ratio were used to calculate the number average height and width of the dispersed phase. Comparing this data to the shrinkage of the samples resulted in a very nice fit of data (Figure 7).

The nucleation effect was only evident for the shrinkage perpendicular to the flow direction. Generally, the shrinkage of the non-nucleated samples was approximately 0.1% lower than for the nucleated materials. The shrinkage in flow direction displayed no significant difference between non-nucleated and nucleated compositions. As the nucleation only marginally affects the morphology of the dispersed phase, this can be assumed to reflect the influence of the matrix crystallinity on shrinkage.

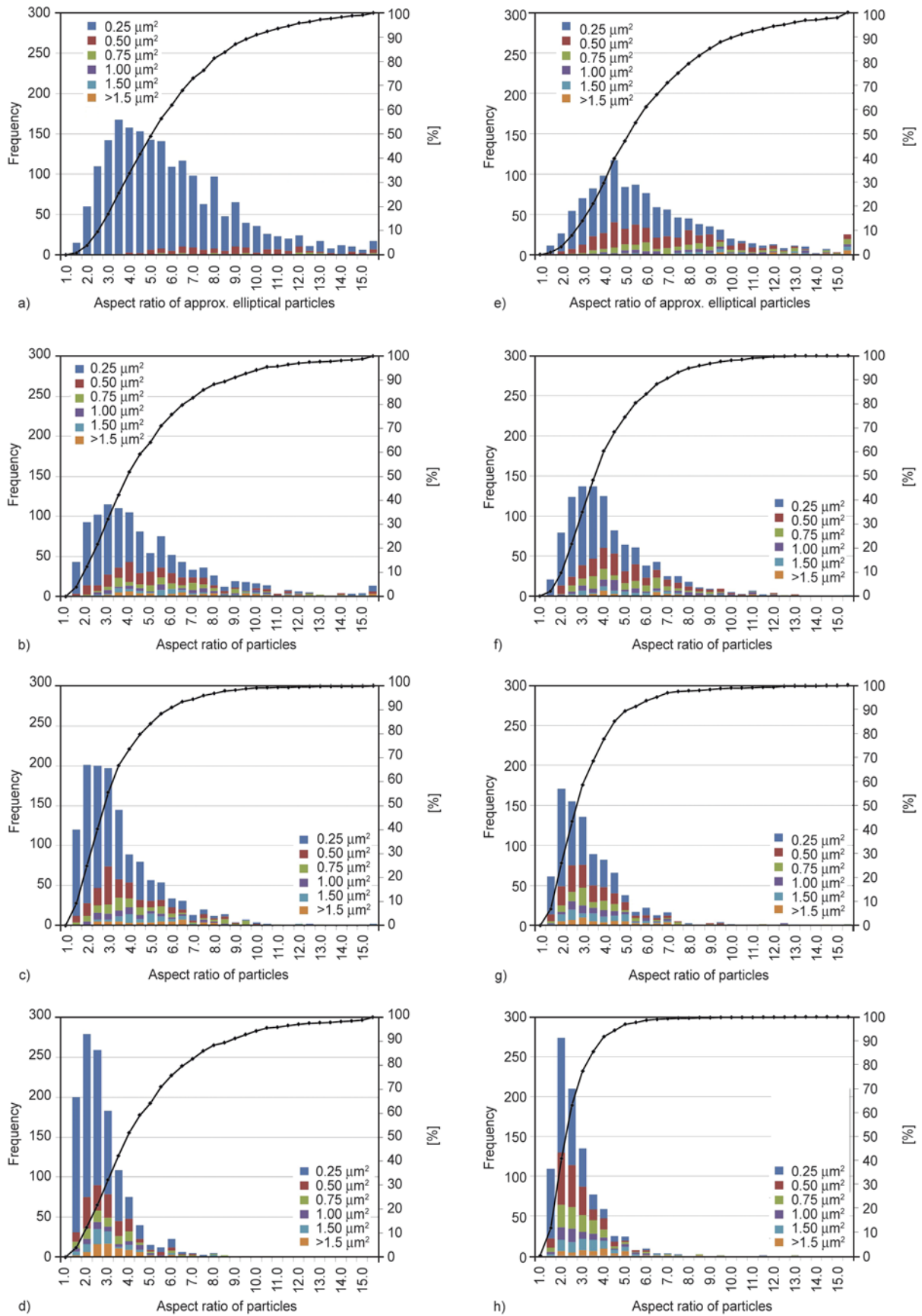


Figure 5. Particle size distribution in the skin layer (a–d) and core region (e–h); IV(XCS) 1.5–1.9–2.2–2.5 from top to bottom

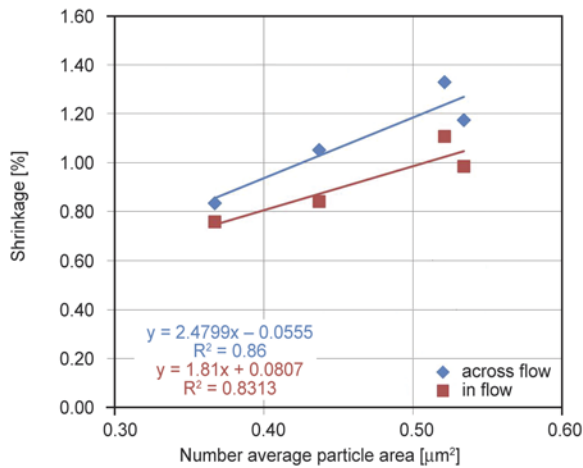


Figure 6. Correlation between shrinkage and number average particle area

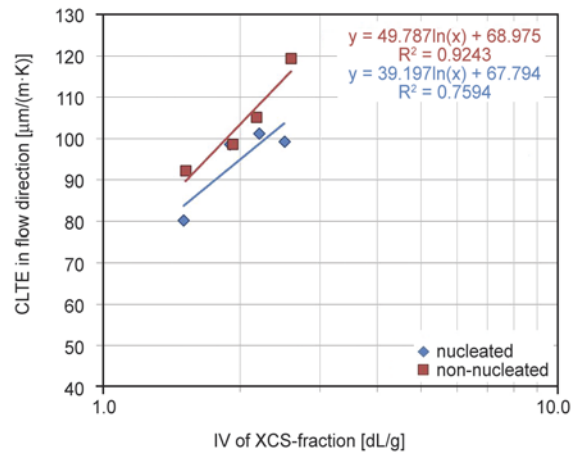


Figure 8. CLTE of the nucleated and non-nucleated materials in relation to the IV of the XCS-fraction (related to melt viscosity of the EPR phase)

3.3. Coefficient of linear thermal expansion (CLTE)

The CLTE was determined on specimens cut from injection molded test bars (in flow direction). These bars have a different geometry and are molded under different conditions than the shrinkage plates. The morphology determined from the latter can therefore only give a rough indication on the influence of dispersed phase morphology on CLTE. SEM investigations of the CLTE specimen would be required to get a more precise correlation. In lack of morphology data for these specimens CLTE was linked to the intrinsic viscosity of the EPR phase resp. XCS only. Similarly to the shrinkage cases, an increase in dimensional change with increasing IV of XCS was observed (Figure 8).

Due to their higher crystallinity, nucleated materials showed an approximately 15 μm·(m⁻¹·K⁻¹) lower CLTE than the corresponding non-nucleated samples. The mobility of polymer chains in a crystal lattice is much more constrained than in amorphous regions. Hence, the volume increase upon heating

and thermal expansion respectively is less for crystalline regions than for amorphous (at least for temperatures above the glass transition and below the melting of the crystals).

4. Conclusions

In the current investigation, the shrinkage of injection molded plates from reactor based PP/EPR blends with a high EPR-content of about 30 wt% and identical EPR composition were evaluated. Scanning Electron Microscopy (SEM) investigations of the polymers showed that the melt viscosity of the dispersed EPR phase, represented by the intrinsic viscosity of XCS fraction, significantly affects the size and distribution of EPR particles. This is in line with theory and was reported by a number of research groups (compare [17–22] and [25– 28]). Unlike in previous studies, the particles' cross sections were not considered to be circular but taken to be elliptically shaped as a result of the orientation in the processing step. Therefore, the average particle diameter was not used in the evaluation of the morphol-

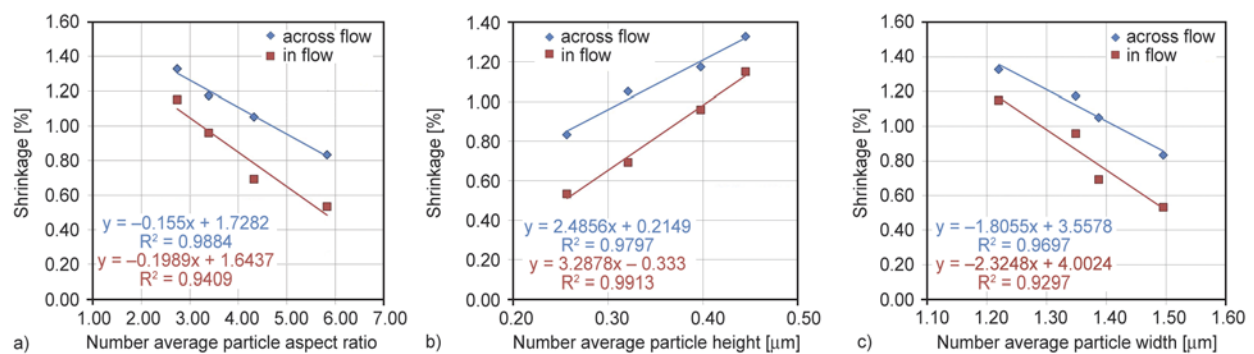


Figure 7. Shrinkage as a function of the number average particle aspect ratio (a), particle height (b) and particle width (c)

ogy of the materials. Instead, the width and height, the aspect ratios as well as the areas of the particles were considered. It was shown that an increase in molecular weight of the EPR is accompanied by an increase in particle size and a decrease in the particles aspect ratio, i.e. a reduced deformation of the particles in the molding step. This coarsening of the phase morphology resulted in an increase in shrinkage and CLTE with the molecular weight of the EPR phase.

From the comparison of nucleated and non-nucleated materials it was found that alpha-nucleation increases the shrinkage across flow direction by about 0.1% while it hardly influences the shrinkage in the flow direction. This increase in shrinkage is a consequence of the higher crystallinity of the nucleated sample. At similar processing conditions, nucleation of PP leads to an increase in the molding shrinkage. The opposite is true for the CLTE.

Acknowledgements

The authors want to thank Renate Eckmayr and Gottfried Kandioller of Borealis Polyolefine GmbH in Linz, Austria for polymerising the materials of this study and preparing the excellent SEM images, respectively. Furthermore, we want to thank Markus Gahleitner, Senior Group Expert PP at Borealis, for his support and expertise in the interpretation and evaluation of collected data. Finally, a special thanks to the staff of the analytical and physical laboratory at Borealis in Linz for fractionating and characterizing the model materials.

References

- [1] Fischer J. M.: Handbook of molded part shrinkage and warpage. William Andrew, New York (2003).
- [2] Zoller P.: The pressure–volume–temperature properties of three well-characterized low-density polyethylenes. *Journal of Applied Polymer Science*, **23**, 1057–1061 (1979).
DOI: [10.1002/app.1979.070230410](https://doi.org/10.1002/app.1979.070230410)
- [3] Jansen K. M. B.: Measurement and prediction of anisotropy in injection moulded PP products. *International Polymer Processing*, **13**, 309–317 (1998).
DOI: [10.3139/217.980309](https://doi.org/10.3139/217.980309)
- [4] Kwon K., Isayev A. I., Kim K. H., van Sweden C.: Theoretical and experimental studies of anisotropic shrinkage in injection moldings of semicrystalline polymers. *Polymer Engineering and Science*, **46** 712–728 (2006).
DOI: [10.1002/pen.20546](https://doi.org/10.1002/pen.20546)
- [5] Pomerleau J., Sanschagrin B.: Injection molding shrinkage of PP: Experimental progress. *Polymer Engineering and Science*, **46**, 1275–1283 (2006).
DOI: [10.1002/pen.20595](https://doi.org/10.1002/pen.20595)
- [6] Fujiyama M., Kimura S.: Effect of molecular parameters on the shrinkage of injection-molded polypropylene. *Journal of Applied Polymer Science*, **22**, 1225–1241 (1978).
DOI: [10.1002/app.1978.070220506](https://doi.org/10.1002/app.1978.070220506)
- [7] Fujiyama M., Kitajima Y., Inata H.: Structure and properties of injection-molded polypropylenes with different molecular weight distribution and tacticity characteristics. *Journal of Applied Polymer Science*, **84**, 2142–2156 (2002).
DOI: [10.1002/app.10372](https://doi.org/10.1002/app.10372)
- [8] Pantani R., Titomanlio G.: Description of PVT behavior of an industrial polypropylene–EPR copolymer in process conditions. *Journal of Applied Polymer Science*, **81**, 267–278 (2001).
DOI: [10.1002/app.1438](https://doi.org/10.1002/app.1438)
- [9] Shelesh-Nezhad K., Taghizadeh A.: Shrinkage behavior and mechanical performances of injection molded polypropylene/talc composites. *Polymer Engineering and Science*, **47**, 2124–2128 (2007).
DOI: [10.1002/pen.20940](https://doi.org/10.1002/pen.20940)
- [10] Prashantha K., Soulestin J., Lacrampe M. F., Lafranche E., Krawczak P., Dupin G., Claes M.: Taguchi analysis of shrinkage and warpage of injection-moulded polypropylene/multiwall carbon nanotubes nanocomposites. *Express Polymer Letters*, **3**, 630–638 (2009).
DOI: [10.3144/expresspolymlett.2009.79](https://doi.org/10.3144/expresspolymlett.2009.79)
- [11] Qi G-Q., Xu Y-J., Yang W., Xie B-H., Yang M-B.: Injection molding shrinkage and mechanical properties of polypropylene blends. *Journal of Macromolecular Science Part B: Physics*, **50**, 1747–1760 (2011).
DOI: [10.1080/00222348.2011.583798](https://doi.org/10.1080/00222348.2011.583798)
- [12] Ono M., Washiyama J., Nakajima K., Nishi T.: Anisotropic thermal expansion in polypropylene/poly(ethylene-co-octene) binary blends: Influence of arrays of elastomer domains. *Polymer*, **46**, 4899–4908 (2005).
DOI: [10.1016/j.polymer.2005.03.098](https://doi.org/10.1016/j.polymer.2005.03.098)
- [13] Ono M., Nakajima K., Nishi T.: Study on thermal expansion in injection-molded isotactic polypropylene and thermoplastic elastomer blends. *Journal of Applied Polymer Science*, **107**, 2930–2943 (2008).
DOI: [10.1002/app.27192](https://doi.org/10.1002/app.27192)
- [14] Spencer M. W., Paul D. R.: Modeling the mechanical and thermal expansion behavior of TPO-based nanocomposites. *Polymer*, **52**, 4910–4919 (2011).
DOI: [10.1016/j.polymer.2011.08.042](https://doi.org/10.1016/j.polymer.2011.08.042)
- [15] Menyhárd A., Gahleitner M., Varga J., Bernreitner K., Jääskeläinen P., Øysæd H., Pukánszky B.: The influence of nucleus density on optical properties in nucleated isotactic polypropylene. *European Polymer Journal*, **45**, 3138–3148 (2009).
DOI: [10.1016/j.eurpolymj.2009.08.006](https://doi.org/10.1016/j.eurpolymj.2009.08.006)

- [16] Gahleitner M., Grein C., Kheirandish S., Wolfschwenger J.: Nucleation of polypropylene homo- and copolymers. *International Polymer Processing*, **26**, 2–20 (2011).
- [17] Karger-Kocsis J., Csikai I.: Skin-core morphology and failure of injection-molded specimens of impact-modified polypropylene blends. *Polymer Engineering and Science*, **27**, 241–253 (1987).
- [18] Paulik C. E., Neißl W.: Phase structure and morphology: Designing a new class of heterophasic PP copolymers. *Technical Papers of the Annual Technical Conference- Society Of Plastics Engineers Incorporated*, **2**, 2565–2570 (1998).
- [19] Grein C., Bernreitner K., Hauer A., Gahleitner M., Neißl W.: Impact modified isotactic polypropylene with controlled rubber intrinsic viscosities: Some new aspects about morphology and fracture. *Journal of Applied Polymer Science*, **87**, 1702–1712 (2003).
DOI: [10.1002/app.11696](https://doi.org/10.1002/app.11696)
- [20] Premphet K., Paecharoenchai W.: Quantitative characterization of dispersed particle size, size distribution, and matrix ligament thickness in polypropylene blended with metallocene ethylene–octene copolymers. *Journal of Applied Polymer Science*, **82**, 2140–2149 (2001).
DOI: [10.1002/app.2060](https://doi.org/10.1002/app.2060)
- [21] Doshev P., Lach R., Lohse G., Heuvelsland A., Grellmann W., Radusch H-J.: Fracture characteristics and deformation behavior of heterophasic ethylene–propylene copolymers as a function of the dispersed phase composition. *Polymer*, **46**, 9411–9422 (2005).
DOI: [10.1016/j.polymer.2005.07.029](https://doi.org/10.1016/j.polymer.2005.07.029)
- [22] Doshev P., Lohse G., Henning S., Krumova M., Heuvelsland A., Micheler G., Radusch H-J.: Phase interactions and structure evolution of heterophasic ethylene–propylene copolymers as a function of system composition. *Journal of Applied Polymer Science*, **101**, 2825–2837 (2006).
DOI: [10.1002/app.22921](https://doi.org/10.1002/app.22921)
- [23] Wu S.: Formation of dispersed phase in incompatible polymer blends: Interfacial and rheological effects. *Polymer Engineering and Science*, **27**, 335–343 (1987).
DOI: [10.1002/pen.760270506](https://doi.org/10.1002/pen.760270506)
- [24] Serpe G., Jarrin J., Dawans F.: Morphology-processing relationships in polyethylene-polyamide blends. *Polymer Engineering and Science*, **30**, 553–565 (1990).
DOI: [10.1002/pen.760300908](https://doi.org/10.1002/pen.760300908)
- [25] Mighri F., Huneault M. A., Ajjji A., Ko G. H., Watanabe F.: Rheology of EPR/PP blends. *Journal of Applied Polymer Science*, **82**, 2113–2127 (2001).
DOI: [10.1002/app.2057](https://doi.org/10.1002/app.2057)
- [26] Kock C., Gahleitner M., Schausberger A., Ingolic E.: Polypropylene/polyethylene blends as models for high-impact propylene–ethylene copolymers, Part 1: Interaction between rheology and morphology. *Journal of Applied Polymer Science*, **128**, 1484–1496 (2013).
DOI: [10.1002/app.38289](https://doi.org/10.1002/app.38289)
- [27] Abramhoff M. D., Magalhães P. J., Ram S. J.: Image processing with ImageJ. *Biophotonics International*, **11**, 36–42 (2004).
- [28] Grein C., Gahleitner M., Knogler B., Nestelberger S.: Melt viscosity effects in ethylene–propylene copolymers. *Rheologica Acta*, **46**, 1083–1089 (2007).
DOI: [10.1007/s00397-007-0200-0](https://doi.org/10.1007/s00397-007-0200-0)

Superior thermal conductivity of transparent polymer nanocomposites with a crystallized alumina membrane

Md. Poostforush, H. Azizi*

Plastics Dept., Processing Faculty, Iran Polymer and Petrochemical Institute, P.O.Box.14965/115, Tehran, Iran

Received 12 October 2013; accepted in revised form 14 December 2013

Abstract. The properties of novel thermoconductive and optically transparent nanocomposites have been reported. The composites were prepared by the impregnation of thermoset resin into crystallized anodic aluminum oxide (AAO). Crystallized AAO synthesized by annealing amorphous AAO membrane at 1200°C. Although through-plane thermal conductivity of nanocomposites improved up to $1.13 \text{ W}\cdot\text{m}^{-1}\cdot\text{K}^{-1}$ (39 vol% alumina) but their transparency was preserved ($T_{\lambda 550 \text{ nm}} \sim 72\%$). Integrated annealed alumina phase, low refractive index mismatch between resin and alumina and formation of nano-optical fibers through the membrane resulted in such marvel combination. This report shows a great potential of these types of nanocomposites in ‘heat management’ of lightening devices.

Keywords: nanocomposites, thermal conductivity, transparent, anodized alumina

1. Introduction

Heat management is a critical issue during the service life of electronic devices. Many applications would benefit from the use of polymers with high thermal conductivity. To have efficient devices, the heat released from itself must be managed to reduce afterwards operating temperature. However, the use of polymeric composite heat sinks is one of the conventional methods to manage the heat in electronic devices. Overheating of LED lightening instruments can decrease their shelf life, quality and amount of light [1]. Heat dissipation through transparent optical parts in electronic devices can suggest new approaches in heat management filed. Incorporation of thermally-conductive micro size ceramics such as silicon carbide, Aluminum Nitride, Boron nitride (BN) and Al_2O_3 to polymeric matrix can enhance thermal conductivity [2–10]. Incorporation of high filler contents of these micro type fillers to get moderate heat dissipation is usual. Addition of limited amount of fillers to transparent polymers will dam-

age their optical transmittance. However in some special applications the transparency is also an important factor for polymer composites. Addition of nano fillers to transparent polymeric matrix can balance both transparency and thermal properties. Based on our knowledge there are few publications on using transparent polymeric composites for heat management applications. Transparent boron nitride nanotubes (BNNT)/ polyvinyl formal composites fabricated by Terao *et al.* [11]. Thermal conductivity of PVF composites contain 1 wt% of filler raised by rate of 156% and reached to $0.26 \text{ W}\cdot\text{m}^{-1}\cdot\text{K}^{-1}$. In another report [12] these authors aligned BNNT in PVA by electrospinning method. Thermal conductivity of transparent composites reached to $0.54 \text{ W}\cdot\text{m}^{-1}\cdot\text{K}^{-1}$ along the BNNT orientation (10 wt%). Greatest through-plane thermal conductivity was claimed in that investigation related to randomly dispersed BNNT composites in PVA ($0.28 \text{ W}\cdot\text{m}^{-1}\cdot\text{K}^{-1}$). It should be noted that in none of above reports, authors did not disclose the optical

*Corresponding author, e-mail: h.azizi@ippi.ac.ir
© BME-PT

transmittance. Shimazaki *et al.* [13] fabricated transparent ($T_{\lambda 550 \text{ nm}}: 72.6\%$) Epoxy/Cellulose nanofibers (CNFs) with high in-plane thermal conductivity ($1 \text{ W}\cdot\text{m}^{-1}\cdot\text{K}^{-1}$ and Through-plane: $0.23 \text{ W}\cdot\text{m}^{-1}\cdot\text{K}^{-1}$). Excellent thermal conductivity of CNFs, small diameter of fibrils ($<50 \text{ nm}$) and low refractive index mismatch between the components can offer such unique combination.

In this letter, transparent nanocomposites were prepared by impregnation of thermoset resin into an annealed AAO membrane. In addition, morphological structure, thermal conductivity and transmittance of nanocomposites were evaluated.

2. Experimental

2.1. Materials

Commercially available AAO membrane (pore size: 20 nm, Anodisc 47, Whatman, International Ltd, Maidstone, UK) selected as a filler. A mixture of Bisphenol A type epoxy (50 wt%, KFR-120, Kukdo Chemical Co. Ltd, Seoul, South Korea) and hardener (50 wt%, KFH-9590H, Kukdo Chemical Co. Ltd, Seoul, South Korea) used as a resin. All of the chemicals were used as received. Refractive index of ingredients listed in Table 1.

Table 1. Refractive index (*R.I.*) of raw materials

Materials	R.I.	Ref
Amorphous alumina	1.60–1.67	Whatman [14]
AAO membrane	1.63	[15]
Epoxy	1.50–1.57	[13, 16]

2.2. Sample preparation

In order to crystallize AAO membrane, we sandwiched them between two alumina plates and located in a furnace (EW-33855-30, Cole-Parmer, Illinois, USA). The temperature was increase at a rate of $3^\circ\text{C}\cdot\text{min}^{-1}$ to a target temperature (1200°C , AAO-1200, ramping: $3^\circ\text{C}\cdot\text{min}^{-1}$) for four hours and then cooled down to room temperature.

Nanocomposites were fabricated by immersion of AAO or AAO-1200 in resin. The impregnated membrane tightly sandwiched by two glass slides and fixed by parallel metal clips and cured at 85°C for three hours to get the nanocomposites. Figure 1 shows a graphical scheme of preparation of these nanocomposites. In order to prepare free-standing films, silicon base release agent (FREKOTE 700-

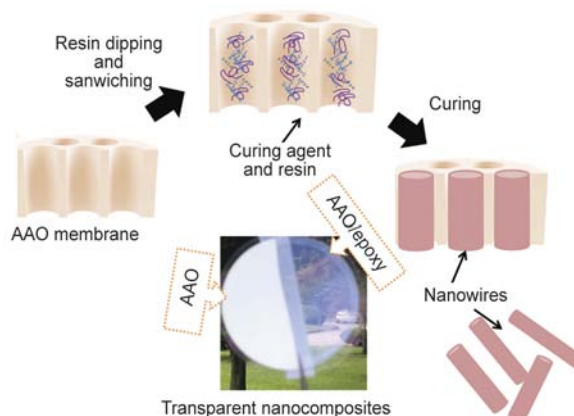


Figure 1. Nanocomposites preparation scheme and related photograph of AAO/epoxy nanocomposites (Glass slides should be added)

NC, Henkel, Hong Kong, China) was applied on the surface of glass before starting the procedure. After curing step, we simply discharged the composites.

2.3. Characterization and measurements

2.3.1. X-ray diffraction

Powder X-ray diffraction (XRD, D/MAX-2500H, Rigaku, Tokyo, Japan) analysis with $\text{Cu K}\alpha_1 = 1.54056 \text{ \AA}$ radiation was used to show the crystallinity enhancement of annealed AAO compare to non-treated AAO membrane. The detector moved step by step ($\Delta 2\theta = 0.05^\circ$) between 10 to 90° .

2.3.2. Field emission scanning electron microscopy (FE-SEM)

A field emission scanning electron microscope (S-4500, JEOL, Tokyo, Japan) at an acceleration voltage of 10 kV used to observe morphological features of unannealed, annealed AAO membrane and prepared composites. Samples were Pt coated, using a sputter coater (108Auto, Cressington Scientific, Watford, UK) for 2 min before imaging, to avoid charging during observation.

2.3.3. Light transmittance

Light transmittance percentage of composites was measured using UV-Vis spectrophotometer (HP-8453, Hewlett Packard, Germany). Two slide glasses were considered as blank for transmittance measurement of all composites which were laminated between two glasses. Laminating between two glasses can limit surface disorders and improve the transmittance of composites.

2.3.4. Thermal conductivity

Through-plane thermal conductivity of nanocomposites can be calculated from thermal diffusivity by using Equation (1):

$$K = \alpha \cdot \rho \cdot C_p \quad (1)$$

Thermal diffusivity (α [mm²/s]) was measured using laser flash method in Microflash instrument (LFA-457, NETZSCH, Selb, Germany). Laser flash technique introduced in 1961 by Parker *et al.* [17]. Laser heat pulses irradiated on the front side of square shape sample; the heat transmitted through the sample thickness direction and measured by an infrared camera. The time to reach the half of the maximum temperature ($t_{1/2}$) at the back side of the sample was chosen to calculate the heat diffusivity according to the Equation (2):

$$\alpha = \frac{1.38L^2}{\pi^2 t_{1/2}} \quad (2)$$

Density (ρ [g/cm³]) gained by electronic densitometer (MD-300S, Alfa Mirage, Tokyo, Japan) and differential scanning calorimeter (N-650, Scinco, Seoul, Korea) used in order to measure the specific heat (C_p [J/(g·K)]). 10–15 mg sample was loaded in the Al pan and the experiments were conducted under nitrogen atmosphere. Optical tightness of transparent free standing films provided by gold sputtering (200 sec) and carbon coating on both sides of samples (1×1 mm). The specific heats of nanocomposite estimated from those of polymer and AAO in terms of mixing rule: Composites = ω_{polymer} Polymer + ω_{AAO} AAO, where ω denotes weight fractions.

3. Results and discussion

3.1. Membrane crystallinity

XRD graphs of annealed (AAO-1200) and unannealed AAO membrane are shown in Figure 2. As it is clear, unannealed membrane just shows a flat curve (without any characteristic peaks) compared to AAO-1200. Flat appearance of unannealed XRD chart can come from amorphous structure and extremely low intensity of fully amorphous structure sample. On the other hand, AAO-1200 chart shows sharp peaks which can relate to θ -alumina [3]. Annealing of amorphous AAO led to crystallinity enhancement of AAO which later can improve the thermal conductivity of membrane.

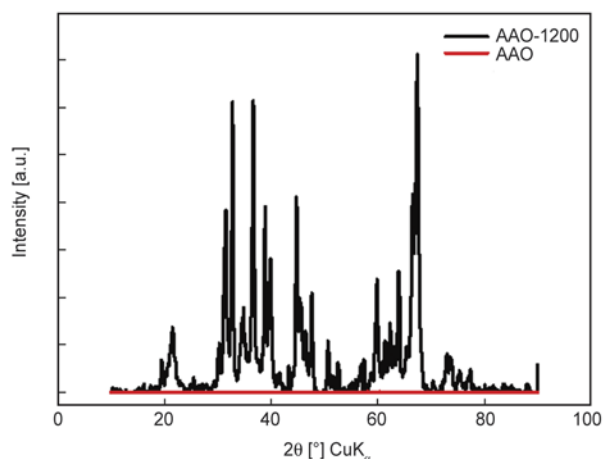


Figure 2. XRD charts of AAO and annealed AAO at 1200°C (AAO-1200)

3.2. Morphological characteristics

Morphology of annealed and unannealed membranes investigated and the micrographs are shown in Figure 3. Unannealed membrane image (Figure 3a) is same as typical surface of AAO sheets that contains high pore density and narrow pore size distribution (~25 nm). Annealing of membrane led to phase transition of amorphous alumina and partially sintering of walls which subsequently reduced the final pores size (~15 nm) of membrane. The insets show opposite side of membranes before and after annealing. Similar evidences found in opposite side, but it was not significant. In addition, morphological changes in cross section, studied after fracturing the membranes as shown in Figure 3c–3d. Figure 3c illustrates non interconnected channels of the membrane which extended in parallel fashion through the thickness. As it can be seen, annealing of membrane made disorders on the cylindrical shape walls (Figure 3d). It is worth nothing to say that, there is a great chance for resin to penetrate to this structure and form polymeric nanowires.

The morphological surface of nanocomposites was also investigated and the images illustrated in Figure 4. For both un-annealed (Figure 4a) and annealed (Figure 4b) composites, surface roughness decreased well in comparison with virgin AAO membrane. Figure 4c–4d shows cross-section of unannealed and annealed composites, respectively. As it is clear, nanowires formed in both types through the sample thickness.

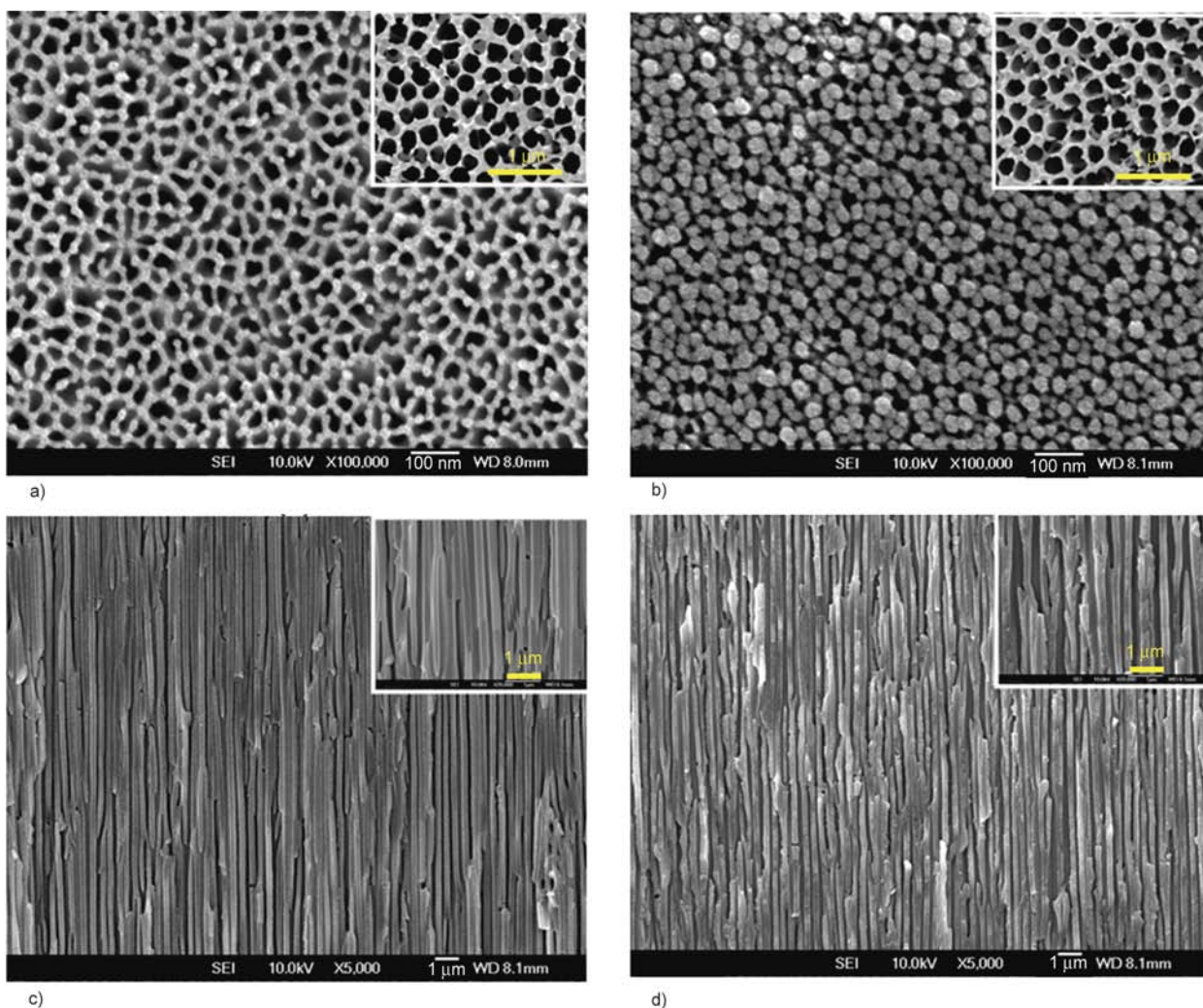


Figure 3. Surface images of (a) unannealed AA sheet, (b) annealed AAO at 1200 °C and cross sectional images of (c) unannealed AA sheet, (d) annealed AAO at 1200°C

3.3. Light transmittance of nanocomposites

Light transmittance measured using UV-Visible spectrophotometer and the results are demonstrated in Figure 5. Lack of optical transmission in AAO membrane is due to surface light scattering and limitations for light diffusion through the thickness (60 μm) of membrane. In transparent organic-inorganic composites, filler size, composite surface roughness and refractive index (RI) difference [18] between inorganic phase and matrix might be responsible for their transparency. The light transmission percentages of annealed and unannealed composites are demonstrated in Figure 5a. Transparency ($T_{\lambda 550 \text{ nm}}$ [%]) of unannealed Anodisc is about 0.04% while for unannealed AAO/epoxy nanocomposites the transparency reached up to 87.90%. As it is clear from Figure 5b, letters behind the free standing AAO-1200/epoxy in the background (nodisc 25) can be seen completely, confirming that the nano-

composites are transparent. Filling pores by transparent resin, which has low refractive index mismatch with membrane, can result in transparent films. As a result of capillary forces [19], precursor successfully penetrated (Figure 3) into the pores and solidified after polymerization. Impregnated thermoset formed nanowires in channels after cross-linking. Nanowires can discharge by dissolving alumina template in nanocomposite at 6 M NaOH. They (Figure 5c) can act as polymeric optical fibers which helped the light to diffuse through the thickness. In addition, it is worth nothing that, prepared composites have high transparency near IR spectral region. Annealing of AAO membrane led to decrement of nanocomposite transparency (AAO-1200, $T_{\lambda 550 \text{ nm}}$: 72.6%) compared to AAO/epoxy. As it was mentioned, the sintering of the membrane [3] would happen due to phase transition of amorphous alumina. Introducing of these types of disorders (Fig-

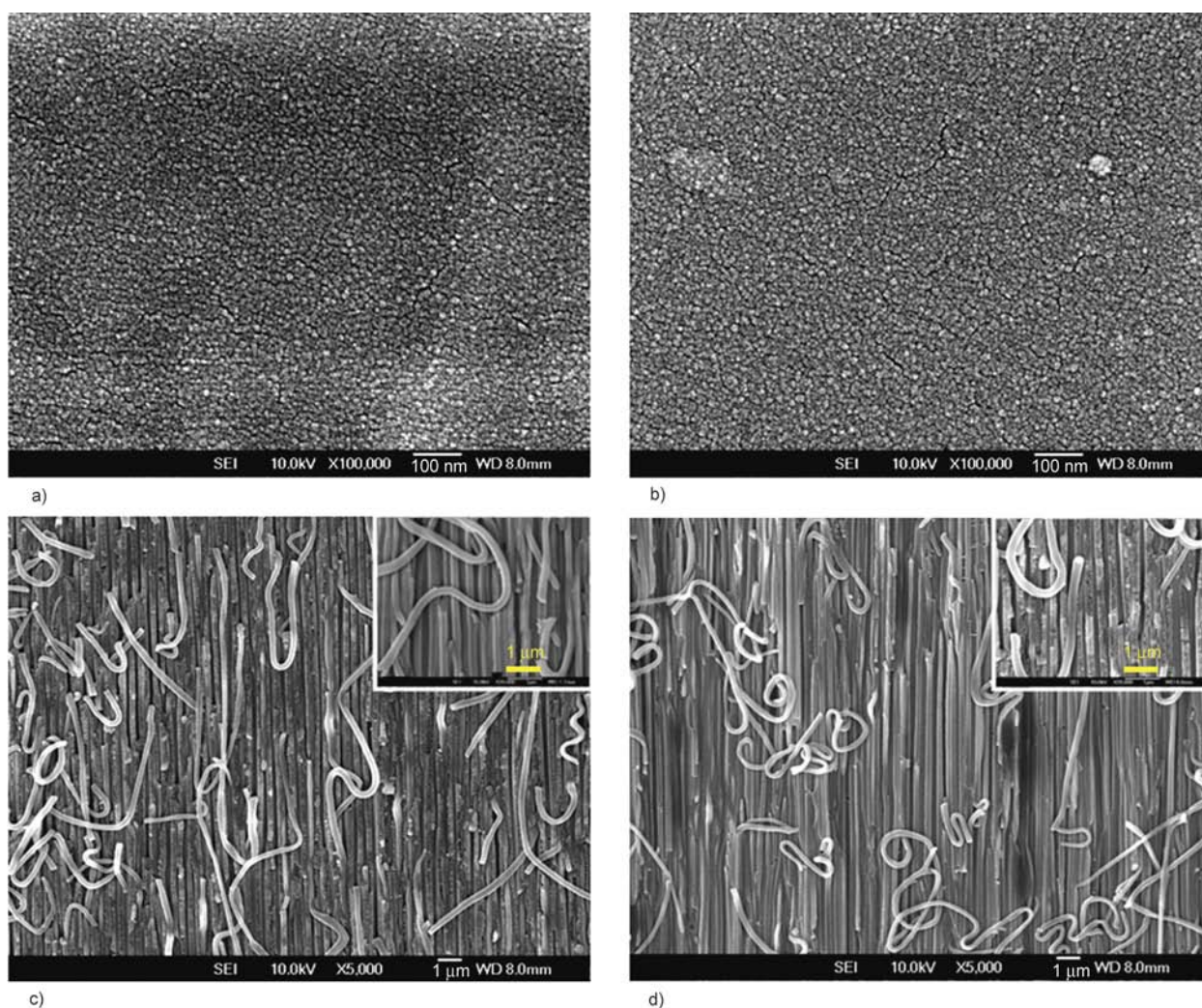


Figure 4. Surface images of nanocomposites with (a) an unannealed AAO/epoxy, (b) AAO-1200/epoxy and cross sectional images of (c) an unannealed AAO/epoxy and (d) AAO-1200/epoxy samples

ure 2b and Figure 2d) can decline pore size and subsequently decrease the transparency of AAO-1200/epoxy nanocomposites. In addition, prepared AAO-1000/epoxy nanocomposites shows similar optical results as we found in the case of AAO-1200/epoxy nanocomposites.

3.4. Thermal conductivity of nanocomposites

High through-plane thermal conductivity of transparent nanocomposites is one of the interesting areas in optical electronics. The highest improvement in through plane thermal conductivity of transparent polymer composites is 53.33% (0.18 to $0.23 \text{ W}\cdot\text{m}^{-1}\cdot\text{K}^{-1}$) which reported by Shimazaki *et al.* [13] for cellulose nano-fiber based nanocomposites. Thermal conductivity of unannealed AAO/epoxy composites attained to $0.25 \text{ W}\cdot\text{m}^{-1}\cdot\text{K}^{-1}$. Higher thermal conductivity of AAO compared to epoxy ($0.15 \text{ W}\cdot\text{m}^{-1}\cdot\text{K}^{-1}$) can suggest this improve-

ment. Thermal conductivity of annealed-AAO/epoxy nanocomposites, calculated and the results reported in Table 2. The thickness and volume contents of filler in nanocomposites mentioned too. As it was expected [3] incorporation of annealed AAO membranes can enhance the total thermal conductivity of composites. Thermal conductivity of epoxy/AAO-1200 samples enhanced up to $1.13 \text{ W}\cdot\text{m}^{-1}\cdot\text{K}^{-1}$. Based on our knowledge this is the highest through-plane thermal conductivity of transparent polymer

Table 2. Thermal conductivity (TC), filler contents and thickness of epoxy nanocomposites

Sample	Filler content [vol%]	Thickness [μm]	TC [$\text{W}\cdot\text{m}^{-1}\cdot\text{K}^{-1}$]
Epoxy	–	80	0.15
AAO membrane	–	60	1.3 [20]
Epoxy/AAO	33	73	0.25
Epoxy/AAO-1000	38	76	1.06
Epoxy/AAO-1200	39	72	1.13

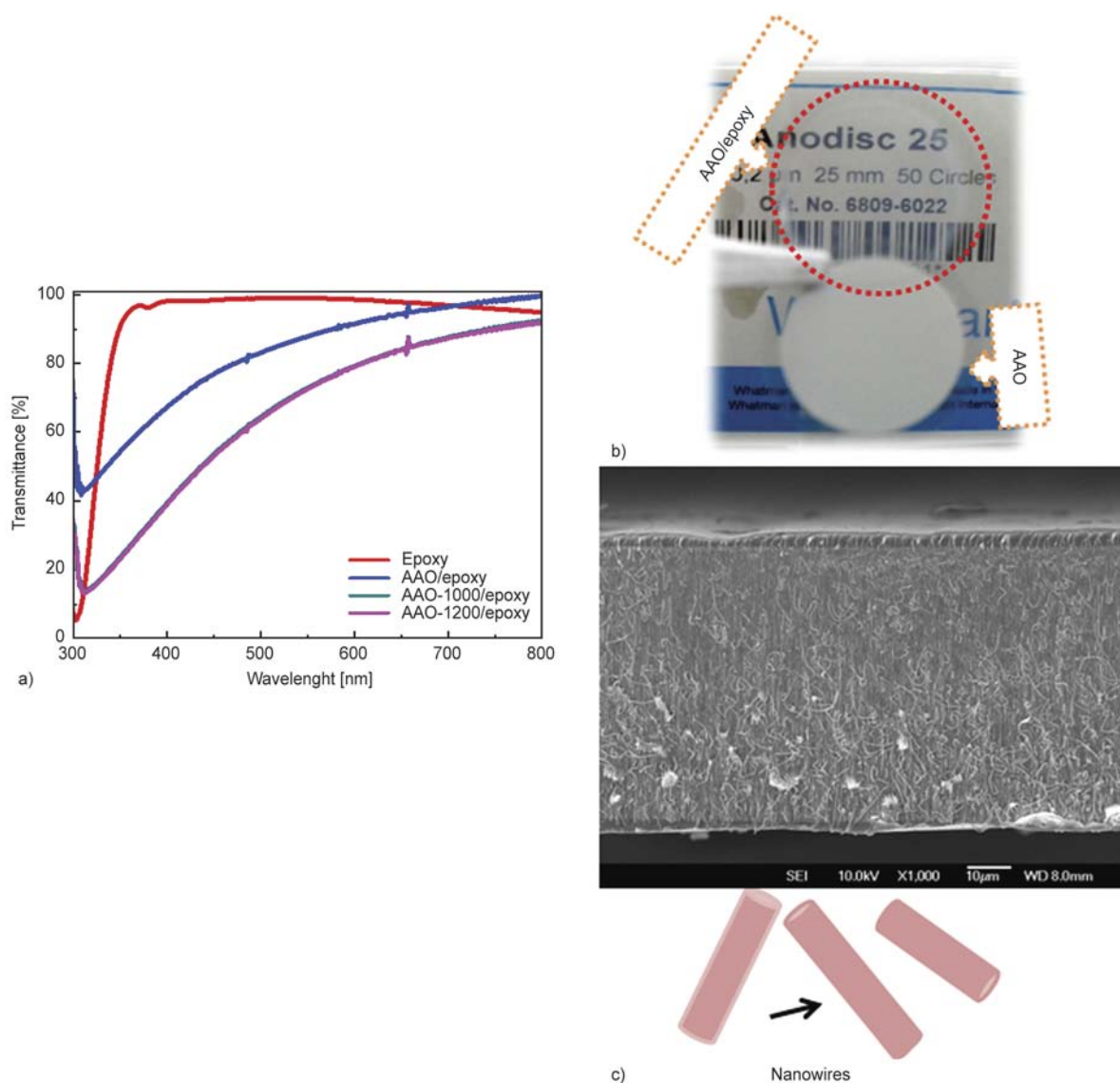


Figure 5. (a) Transmission spectra of annealed and unannealed AAO membrane and their nanocomposites, (b) a photograph of AAO membrane and AAO/epoxy composites (c) FE-SEM image of epoxy nanowires through the AAO thickness of AAO/epoxy nanocomposites

nanocomposites which has been reported till now. Thermal conductivity of composites enhanced more than 7 times while transmittance percentage ($T_{\lambda 550 \text{ nm}}$ [%]) is about 70%. It should be considered that, to get more accurate thermal conductivity results, thickness of samples should be close to thickness of AAO membrane (60 μm).

4. Conclusions

In summary, we successfully prepared thermally conductive and transparent nanocomposites by a simple impregnation based method. Crystalline structure of annealed AAO membrane characterized by XRD. FE-SEM was selected to study the morphological changes as a result of annealing. Filling the parallel pores of membrane with resin of similar

refractive index and formation of polymeric nanowires through the sample thickness resulted in transparent nanocomposites. Through-plane thermal conductivity of composites enhanced as high as $1.13 \text{ W}\cdot\text{m}^{-1}\cdot\text{K}^{-1}$ as a result of devitrification of the amorphous alumina membrane after annealing at 1200°C . These types of nanocomposites can open new heat management approaches in small electronic devices, high power LED lightening devices and so on.

Acknowledgements

We would like to acknowledge department of polymer engineering of 'Korea National University of Transportation' for providing some facilities for us.

References

- [1] Cao D., Jensen S. D.: Led light source. U.S. Patent 13665689, USA (2013).
- [2] Shimazaki Y., Hojo F., Takezawa Y.: Preparation and characterization of thermoconductive polymer nanocomposite with branched alumina nanofiber. *Applied Physics Letters*, **92**, 133309/1–133309/4 (2008). DOI: [10.1063/1.2907315](https://doi.org/10.1063/1.2907315)
- [3] Shimazaki Y., Hojo F., Takezawa Y.: Highly thermoconductive polymer nanocomposite with a nanoporous α -alumina sheet. *ACS Applied Materials and Interfaces*, **1**, 225–227 (2008). DOI: [10.1021/am800055s](https://doi.org/10.1021/am800055s)
- [4] Zhou W.: Thermal and dielectric properties of the AlN particles reinforced linear low-density polyethylene composites. *Thermochimica Acta*, **512**, 183–188 (2011). DOI: [10.1016/j.tca.2010.10.003](https://doi.org/10.1016/j.tca.2010.10.003)
- [5] Hong J-P., Yoon S-W., Hwang T., Oh J., Hong S., Lee Y., Nam J.: High thermal conductivity epoxy composites with bimodal distribution of aluminum nitride and boron nitride fillers. *Thermochimica Acta*, **537**, 70–75 (2012). DOI: [10.1016/j.tca.2012.03.002](https://doi.org/10.1016/j.tca.2012.03.002)
- [6] Song W-L., Wang P., Cao L., Anderson A., Meziani M., Farr A., Sun Y-P.: Polymer/boron nitride nanocomposite materials for superior thermal transport performance. *Angewandte Chemie International Edition*, **51**, 6498–6501 (2012). DOI: [10.1002/anie.201201689](https://doi.org/10.1002/anie.201201689)
- [7] Yu J., Huang X., Wu C., Wu X., Wang G., Jiang P.: Interfacial modification of boron nitride nanoplatelets for epoxy composites with improved thermal properties. *Polymer*, **53**, 471–480 (2012). DOI: [10.1016/j.polymer.2011.12.040](https://doi.org/10.1016/j.polymer.2011.12.040)
- [8] Yu J., Huang X., Wang L., Peng P., Wu C., Wu X., Jiang P.: Preparation of hyperbranched aromatic polyamide grafted nanoparticles for thermal properties reinforcement of epoxy composites. *Polymer Chemistry*, **2**, 1380–1388 (2011). DOI: [10.1039/C1PY00096a](https://doi.org/10.1039/C1PY00096a)
- [9] Yu J., Duan J., Peng W. Y., Wang L. C., Peng P., Jiang P. K.: Influence of nano-AlN particles on thermal conductivity, thermal stability and cure behavior of cycloaliphatic epoxy/trimethacrylate system. *Express Polymer Letters*, **5**, 132–141 (2011). DOI: [10.3144/expresspolymlett.2011.14](https://doi.org/10.3144/expresspolymlett.2011.14)
- [10] Qian R., Yu J., Xie L., Li Y., Jiang P.: Efficient thermal properties enhancement to hyperbranched aromatic polyamide grafted aluminum nitride in epoxy composites. *Polymers for Advanced Technologies*, **24**, 348–356 (2013). DOI: [10.1002/pat.3090](https://doi.org/10.1002/pat.3090)
- [11] Terao T., Bando Y., Mitome M., Zhi C., Tang C., Goldberg D.: Thermal conductivity improvement of polymer films by catechin-modified boron nitride nanotubes. *The Journal of Physical Chemistry C*, **113**, 13605–13609 (2009). DOI: [10.1021/jp903159s](https://doi.org/10.1021/jp903159s)
- [12] Terao T., Zhi C., Bando Y., Mitome M., Tang C., Goldberg D.: Alignment of boron nitride nanotubes in polymeric composite films for thermal conductivity improvement. *The Journal of Physical Chemistry C*, **114**, 4340–4344 (2010). DOI: [10.1021/jp911431f](https://doi.org/10.1021/jp911431f)
- [13] Shimazaki Y., Miyazaki Y., Takezawa Y., Nogi M., Abe K., Ifuku S., Yano H.: Excellent thermal conductivity of transparent cellulose nanofiber/epoxy resin nanocomposites. *Biomacromolecules*, **8**, 2976–2978 (2007). DOI: [10.1021/bm7004998](https://doi.org/10.1021/bm7004998)
- [14] Groner M. D., Fabreguette H. F., Elam J. W., George S. M.: Low-temperature Al₂O₃ atomic layer deposition. *Chemistry of Materials*, **16**, 639–645 (2004). DOI: [10.1021/cm0304546](https://doi.org/10.1021/cm0304546)
- [15] Liu Y., Wang H. H., Indacochea J. E., Wang M. L.: A colorimetric sensor based on anodized aluminum oxide (AAO) substrate for the detection of nitroaromatics. *Sensors and Actuators B: Chemical*, **160**, 1149–1158 (2011). DOI: [10.1016/j.snb.2011.09.040](https://doi.org/10.1016/j.snb.2011.09.040)
- [16] Tao P., Li Y., Rungta A., Viswanath A., Gao J., Benicewicz B. C., Siegel R. W., Schadler L. S.: TiO₂ nanocomposites with high refractive index and transparency. *Journal of Materials Chemistry*, **21**, 18623–18629 (2011). DOI: [10.1039/C1JM13093E](https://doi.org/10.1039/C1JM13093E)
- [17] Parker W., Jenkins R., Butler C., Abbott G.: Flash method of determining thermal diffusivity, heat capacity, and thermal conductivity. *Journal of Applied Physics*, **32**, 1679–1684 (1961). DOI: [10.1063/1.1728417](https://doi.org/10.1063/1.1728417)
- [18] Lü C., Yang B.: High refractive index organic–inorganic nanocomposites: Design, synthesis and application. *Journal of Materials Chemistry*, **19**, 2884–2901 (2009). DOI: [10.1039/B816254A](https://doi.org/10.1039/B816254A)
- [19] Cheng D. F., Yagihashi M., Hozumi A.: Lamination of alumina membranes to polymer surfaces: Thick, hard, transparent, crack-free alumina films on polymers with excellent adhesion. *ACS Applied Materials and Interfaces*, **3**, 2224–2227 (2011). DOI: [10.1021/am200662d](https://doi.org/10.1021/am200662d)
- [20] Zhou M., Lin T., Huang F., Zhong Y., Wang Z., Tang Y., Bi H., Wan D., Lin J.: Highly conductive porous graphene/ceramic composites for heat transfer and thermal energy storage. *Advanced Functional Materials*, **23**, 2263–2269 (2013). DOI: [10.1002/adfm.201202638](https://doi.org/10.1002/adfm.201202638)